Summer 2014

High fidelity simulations of electrokinetic phenomena in microfluidic devices

Qian Li
Purdue University

Graduate School ETD Form 9
(Revised 01/14)

PURDUE UNIVERSITY
GRADUATE SCHOOL
Thesis/Dissertation Acceptance

This is to certify that the thesis/dissertation prepared

By Li, Qian

Entitled
HIGH FIDELITY SIMULATIONS OF ELECTROKINETIC PHENOMENA IN MICROFLUIDIC DEVICES

For the degree of Doctor of Philosophy

Is approved by the final examining committee:

STEVEN H. FRANKEL

JUN CHEN

STEVEN T. WERELEY

TOM I. SHIH

To the best of my knowledge and as understood by the student in the *Thesis/Dissertation Agreement. Publication Delay, and Certification/Disclaimer (Graduate School Form 32)*, this thesis/dissertation adheres to the provisions of Purdue University's "Policy on Integrity in Research" and the use of copyrighted material.

STEVEN H. FRANKEL

Approved by Major Professor(s): _____

Approved by: GANESH SUBBARAYAN 09/18/2014

Head of the Department Graduate Program Date

HIGH FIDELITY SIMULATIONS OF ELECTROKINETIC PHENOMENA IN MICROFLUIDIC DEVICES

A Dissertation

Submitted to the Faculty

of

Purdue University

by

Qian Li

In Partial Fulfillment of the

Requirements for the Degree

of

Doctor of Philosophy

December 2014

Purdue University

West Lafayette, Indiana

ACKNOWLEDGMENTS

I would like to sincerely and gratefully thank my advisor Prof. Steven H. Frankel for his continuous support during my PhD. His motivating ideas, encouraging advice and guidance helped me explore new research areas and make progress in the research. I also would like to express my gratitude to Prof. Moran Bercovici at Technion, Israel Institute of Technology for his invaluable comments and advice on my study of electrokinetic instability and isotachophoresis. His guidance and knowledge were very effective and greatly helped me overcome my theoretical struggles. Many thanks to Prof. Tom Shih, Prof. Steven Wereley, Prof. Jun Chen for agreeing to serve on my advisory committee and providing their valuable comments and guidelines.

I am very thankful to Dr. Kameswararao Anupindi and Dr. Yann Delorme for the tremendous help and beneficial suggestions they gave for my academic and research studies. Their extensive knowledge in CFD, insightful discussions, and encouragement made it possible for me to develop the codes for simulating electrokinetic phenonema. I learned so much from these two excellent CFD researchers and I cannot thank them enough!

I want to appreciate my friends Zhe Luo, Zhuohua Shen, Weichen Lai, Yan Xue, Ruihong Zhang, Yi Kong and many more. They made my research and personal life at Purdue a colorful and memorable one. Special thanks to my closest friends Yu Liu and Juan Han for their continuous encouragement and inspiring conversations that helped me survive from the stressful days of doubt and uncertainty.

Last but not least, I would like to deeply thank my parents Pingyuan Li and Songping Hu. Without their love, support, encouragement, criticism, and patience at every step of the way, there is no chance for me to finish my PhD. I can never thank them enough. I love them, always!

TABLE OF CONTENTS

Page

LIST OF TABLES

LIST OF FIGURES

Figure Page

Figure Page

ABSTRACT

Li, Qian Ph.D., Purdue University, December 2014. High Fidelity Simulations of Electrokinetic Phenomena in Microfluidic Devices. Major Professor: Steven H. Frankel.

Electroosmotic flow with electrokinetic effects is the primary method of fluid handling in micro-total analysis systems. Under external applied electric fields, electrokinetic micro-devices allow for innovative functionality in a wide range of microfluidic applications including sample injection, separation, rapid micromixing, and miniaturized chemical and biochemical analysis and detection. This dissertation focuses on simulations of two electrokinetic phenomena, isotachophoresis (ITP) and electrokinetic instability (EKI). A set of coupled governing equations including the incompressible Naiver-Stokes equations, Nernst-Planck transport equations and a charge conservation equation are solved in the simulation. A multiblock in-house solver based on high-order finite difference schemes is developed to solve the system of equations and thus to numerically capture essential physics of ITP and EKI in microfluidic devices. Validation of the solver is provided for one-dimensional ITP problems in which sharp gradients present in species concentration and electric fields. It is demonstrated that the current solver can offer an accurate non-oscillatory solution with reduced numerical diffusion compared to several existing numerical schemes on a given uniform grid. Two-dimensional ITP and EKI problems are then simulated to acquire a good understanding of the basic mechanism and behavior of the two electrokinetic phenomena under certain conditions. Finally, a series of three-dimensional simulations are carried out to predict EKI phenomena in a realistic cross-shaped microchannel. It is shown that the current solver has the capability to capture the threshold value of applied electric field for the onset of instabilities and it offers a better prediction

for the critical features of EKI phenomena in the considered cross-shaped microchannel compared to the numerical and experimental results presented in the literature. Moreover, in the general parametric study the present solver also explores several useful guidelines showing the effect of different parameters, including the electric field strength, the conductivity ratio, the channel depth as well as the electric field ratio on EKI in a cross-shaped microchannel.

1. INTRODUCTION

1.1 Motivation

Electrokinetic flows with conductivity gradients or ion density gradients occur in a wide range of microfluidic applications [1], [2]. As a result, many integrated electrokinetic micro-devices have been developed as a key component for micro-total-analysis systems over the past two decades. The so-called micro-total-analysis systems (μTAS) refer to those microfluidic systems that integrate multiple laboratory processes and functions on a single platform. Compared to their macro-scale counterparts, such systems offer many advantages including a more rapid analysis, a significant improvement in performance, and a reduction in reagent consumption and the amount of chemical waste [3]. When electrokinetic devices are used in these μTAS, electric fields are typically employed to fulfill novel functionalities, for example, to enable rapid and miniaturized chemical and biochemical analysis and detection [4]. However, due to electro-osmotic flow mismatch and electrokinetic instability, complex flow phenomena may occur and it challenges our fundamental understanding and prediction capability for electrokinetic flows [5]. Thus, relevant knowledge is desired so as to achieve robust control of the electrokinetic phenomena induced in the electrokinetic microfluidic devices.

The main motivation for the current work is connected with two electrokinetic problems, isotachophoresis (ITP) and electrokinetic instability (EKI). Both of these two problems are challenging while can be widely used in various fields including genetics, pharmacology, chemistry and biochemistry [6]. For example, as an electrophoresis technique which allows for simultaneous separation and focusing of chemical and biological species, ITP poses difficult design and simulation challenges especially when high electric fields and ion density gradients are involved in electrophore-

sis processes. In EKI, despite that the cells observed in the electroconvective motion may look similar to Rayleigh-Benard convection cells, the EKI phenomena are much more complicated from both the physical and the mathematical points of view. The present research focuses on simulating the two important and challenging electrokinetic phenomena in microfluidic devices as described above. As a strong research tool like experiments, computational fluid dynamics (CFD) simulations can provide valuable details and insights of the electrokinetic phenomena. For instance, in ITP computer simulations give a way to reveal fundamental processes ruling the dynamics of electrokinetic separation and preconcentration methods. For EKI, the knowledge acquired from the numerical study can not only provide useful guidelines for design improvement for electrokinetic micro-devices, but it may also offer a more efficient way to implement rapid micromixing for low Reynolds number flows.

1.2 Background

The increasing demands for novel and effective mixing technologies as well as the smooth execution of complex chemical reactions in process industry, pharmacy, chemical analysis and biochemistry have generated extensive research interest. As a result, a considerable variety of micro-reaction technologies and microfluidic systems have been developed during the past twenty years. Nowadays, besides stand-alone micro-devices the microfluidic systems known as lab-on-a-chip (LOC) or μTAS are more and more widely used in practice to offer the promise of integrating multiple laboratory processes onto one single chip, and thereby increasing throughput and decreasing assay cost [7]. μTAS devices are generally designed to carry out the functions such as sample introduction, injection, mixing, reaction, dispensing, separation and detection through a series of micrometer-scale channels [8].

Since the characteristic length scales of such systems are in the micrometer range, the properties of flows in μTAS are different from macro-scale flows and they are dominantly controlled by viscous forces rather than inertia [9]. The reduced dimensions

of μTAS can lead to a large surface-to-volume ratio, which increases heat and mass transfer efficiencies, for example, the small dimensions allow rapid diffusive mixing to occur in as little as 100 μs [10]. In addition, due to this large surface-to-volume ratio property, many interesting interfacial phenomena that are usually neglected in macro-scale fluid mechanics, namely wetting properties, surface tension, capillary effects, electrokinetic effects, etc. could be considered as driving forces [5]. In the above mentioned effects, employing electric fields and taking advantage of electrokinetic phenomena to manipulate fluids in microchannels has been demonstrated as one of the most promising approaches [11]. Compared to the traditional micro-devices like syringe pumps that use mechanical forces to drive fluids, electrokinetic devices require no external mechanical moving parts and they have the advantages of a simpler microchannel design, a more straightforward fabrication process, and a rudimentary voltage control scheme [12].

In the following two subsections, a brief overview of the two electrokinetic problems in microfluidic devices that would be studied in the present work are provided respectively, including the relevant major concepts, the applications, and a review of previous studies. Electrokinetic instability (EKI) is introduced first, and then it is followed by an introduction to the electrophoretic preconcentration and separation technique, isotachophoresis (ITP).

1.2.1 Electrokinetic Instability (EKI)

In the applications of electrokinetic micro-devices, one important regime is on-chip biochemical assays with high conductivity gradients. Conductivity gradients are prevalent in on-chip electrokinetic processes including multi-dimensional assays [13], systems with poorly specified sample chemistry, and pre-concentration methods such as isoelectric focusing [14] and field amplified sample stacking [15]. Electrokinetics (EK) is a branch of electrohydrodynamics (EHD) that describes the interaction of ion transport, fluid motion and electric fields and it is distinguished from EHD by the

relevance of interface charge at solid-liquid interfaces [16]. Microfluidic flows (typically with Reynolds numbers of order unity or smaller) are characterized by low velocities (typically in order of $10^{-3}m/s$) and extremely small characteristic lengths (typically between $1\mu m$ and $100\mu m$) resulting in laminar flows that are strongly damped by viscous forces and are very stable for most flow conditions. However, under certain conditions, owing to electrokinetic instabilities heterogeneous ionic conductivity fields in the presence of applied electric fields can make the flows become unstable and lead to propagation of the instability through the flows by maintaining those conditions.

Electrokinetic instability (EKI) is a microscale instability arising from the coupling of the electric field, ion-electromigration as well as fluid motion. The reason why the terminology "electrokinetic instability" is chosen is because it is relevant to electrokinetic microfluidic systems and more importantly the convective nature of such instability is somehow determined by electro-osmotic flow. Since the first reported observation of EKI in an electrokinetic microsystem by Oddy et al. in 2001 [17], EK techniques received renewed interests. Extensive research in the development of more accurate models for predicting threshold conditions for instability onset as well as other flow features like coherent wave structures and mixing rate were conducted. In 2002, by using experimental research tool Chen and Santiago [18] explored that conductivity gradient and high electric field strength play a very important role in inducing the instability. After that, more systematic experimental investigations on EKI were performed in greater details by various groups. The research covered different aspects of EKI including electroosmotic convection [19, 20], time-periodic forcing [12, 21], multiple-species [22], chaotic dynamics [23, 24], and various design problems for micromixing applications [25–28]. Among these experimental studies, the work done by Posner and Santiago [20] is of especial importance as this research completed an extensive parametric study for convective instability in cross-shaped microchannels. It investigated the stability of a layer of high-conductivity solution sandwiched between two low-conductivity streams in which the applied field was or-

thogonal to the conductivity gradient. This work provided a detailed parametric database for the design of EK applications with a generic and general configuration.

Besides experimental manners, researchers also took advantage of numerical simulations as a strong research tool to obtain insights of the EKI mechanism and behavior. In 2004 Lin et al. [29] related the instability physics with earlier works on EHD instability and developed a set of governing equations based on a modified Ohmic model to study EKI with a symmetric binary electrolyte. Along with experimental data, 2D and 3D numerical simulations were presented for the temporal disturbances that form at the interface of two liquid streams in a long, rectangular cross-section straight channel using second-order numerical schemes. In the study, it was found that compared with the 2D linear analysis, the 3D analysis provided much closer agreement with experimentally measured values. In 2005, by adopting the reduced form of the equations provided by Lin et al., Storey [30] implemented 2D and 3D simulations for EHD flows driven by conductivity gradients in a rectangular straight microchannel and studied the effects of different assumptions in boundary conditions on nonlinear behavior of EKI using direct numerical simulation. In addition, Storey pointed out that if the channel is deep such that instability can occur even in the depth direction, then the depth-averaged equations are no longer applicable and 3D numerical simulation is the only viable option for flow modeling. In 2006, Kang et al. [31] performed a numerical analysis for a two-dimensional unsteady DC electroosmotic flow using a second-order finite volume method and examined the initial and later stages of growth of the convective instability in T-shaped microchannels. In 2009, Luo [32] performed a series of numerical and experimental investigations in the use of EKI effects to achieve species mixing within a cross-shaped microchip, the same flow geometry as presented in [20]. In the numerical study, only 2D simulations were conducted by employing the backward-Euler time-stepping method and second-order central difference scheme. More recent research about EKI is focusing on chaotic dynamics of electrokinetic flows. In 2013, Druzgalski et al. [33] used direct numerical simulations of the coupled Poisson-Nernst-Planck and Navier-Stokes

equations to study transport processes associated with electro-hydrodynamic chaos in electrokinetic systems containing an ion-selective surface. In 2013, Demekhin et al. [34] adopted a finite-difference method with second-order accuracy for the spatial discretization and a semi-implicit $3\frac{1}{3}$-step Runge-Kutta scheme for the integration in time to numerically study EKI and an unusual transition to chaotic motion near a charge-selective surface. The numerical investigation gave a qualitative agreement of the experimental and the theoretical values of the threshold of instability.

1.2.2 Isotachophoresis (ITP)

Isotachophoresis (ITP) is an electrophoretic preconcentration and separation technique that utilizes a heterogeneous buffer system of disparate electrophoretic mobilities [35]. Due to the features of simultaneous separation and focusing of a wide range of chemical and biological species, ITP is useful in numerous applications such as drug discovery, toxin detection, pharmacology, genetics and food analysis [36, 37]. In ITP it typically requires two zones containing different electrolytes: a trailing electrolyte (TE) with low ionic mobility and a leading electrolyte (LE) with high ionic mobility. The sample analytes of interest should have intermediate mobilities. Under the action of an electric field, the sample ions separate simultaneously and redistribute themselves in segregated zones in order of decreasing mobility starting from TE to LE along the channel. At steady state, these focused sample zones migrate at an identical speed as that of the leading zone, thus it is termed "iso(same)-tacho(speed)-phoresis(transport)" which is derived from the ancient Greek [38].

Due to the inherent preconcentration effect of ITP, sharp concentration boundaries can be formed between adjacent sample zones. With the increase of the applied electric field the interfaces of sample zones become even sharper as the width of the interface is inversely proportional to the applied electric field [39]. As a result, ITP can be difficult to simulate because of the mathematical stiffness that accompanies steep concentration gradients, i.e. significant spurious oscillations may occur when

simulating ITP under high electric fields. In order to accurately resolve the sharp interfaces, numerous numerical schemes were proposed over the past 20 years including simulation software packages such as the 1D solver GENTRANS [40–42], SIMUL [43], SPRESSO [44] as well as commercially available multidimensional software such as CFD-ACE+ (ESI, Huntsville, AL, USA) [45] and COMSOL Multiphysics (COMSOL, Inc., Burlington, MA, USA) [46]. Roughly speaking, most of the solvers were developed to simulate 1D ITP in simple, linear channels and the numerical schemes basically fall into two categories: non-dissipative schemes and dissipative schemes. In general, most existing non-dissipative schemes adopt a second-order central discretization on a uniform grid [47–51]. To reduce numerical oscillations, such schemes require a large number of grid points. For example, at realistic electric fields and channel lengths it may need $O(10^3) - O(10^4)$ uniform grid points which results in very long computation cost even on modern computers [49, 50]. In order to improve the performance of non-dissipative schemes, Bercovici et al. proposed a non-dissipative sixth-order compact scheme with an adaptive grid algorithm [44, 52]. This solver named SPRESSO is an open-source simulation tool for 1D electrophoresis available at [53]. The advantage of the SPRESSO solver over the previous non-dissipative schemes is not only due to its high order accuracy but also from the high resolution. In addition, with an adaptive grid mechanism SPRESSO allows grid points to accumulate in relatively small regions that include high concentration gradients and thus this solver can give accurate solutions to ITP simulations while using much less computational resources.

In contrast to non-dissipative schemes, dissipative schemes can offer faster and non-oscillatory solutions to ITP simulations under high electric fields. However, this is at the cost of physical accuracy as dissipative schemes would introduce numerical dissipation so as to stabilize the solutions. Based on the second-order centered spatial discretization, Ermakov et al. introduced artificial dispersion to the scheme to achieve higher resolution and thus obtained smooth solutions up to a low current density of $100A/m^2$ (one order of magnitude lower than current densities used in the labora-

tory) [54]. Martens et al. implemented first-order upwind discretization and other higher order dissipative scheme such as third-order QUICK (Quadratic Upstream Interpolation for Convective Kinematics) scheme [55]. It was found that the first-order upwind scheme allowed non-oscillatory solutions at current densities of order $1000 A/m^2$ but resulted in overly diffused concentration interfaces, i.e. wider interfaces than analytical solution. The third-order QUICK scheme was specifically useful for the decrease of such numerical diffusion. Hence, it was pointed out by [55] that higher-order algorithms generally offer better results than lower-order algorithms when looking at the zone boundary thickness which is critical in ITP simulations. Sounart and Baygents proposed a second-order FTC (flux-corrected transport) method to offer limited numerical dissipation in the scheme and thus made the interface widths much closer to the expected values compared with the first-order upwind scheme [56]. Similarly, Yu et al. used a second-order CESE (the spacetime conservation element and solution element) method to reduce the numerical dissipation and thereby improved the accuracy at interfaces compared with upwind schemes [57]. There were few numerical studies on two-dimensional ITP and to our knowledge none on three-dimensional ITP problems even in recent years. Shim et al. applied different finite-volume schemes with first- or second-order accuracy to numerically study isotachophoretic separation in microchannels in which five ionic components were considered [58]. They obtained qualitative agreement with the existing 1D model and pointed out that the power-law scheme is superior to the other schemes used in the paper due to its higher accuracy. Bhattacharyya et al. adopted the finite volume method using a third-order QUICK scheme to simulate sample dispersion in ITP with pressure-driven or electroosmotic counterflow [59, 60]. In the study, they only considered one sample species besides the LE and TE electrolytes.

1.3 Objectives and Organization

In the previous section, it has been shown that electrokinetic problems are interesting examples of complex, multi-physical flow phenomena on the micro-scales and they have a wide range of applications in microfluidic systems [61–66]. Due to non-linear electromigration physics, steep gradients in species concentration and/or electric fields occur in the electrokinetic phenomena of EKI and ITP. In order to accurately resolve sharp interfaces and simulate essential physics of EKI and ITP, a high order solver is required. Therefore, the primary objective is to provide a high order accurate numerical tool to simulate and study the electrokinetic phenomena of EKI and ITP in microfluidic devices. The solver is an in-house high-order accurate finite-difference incompressible Navier-Stokes solver, originally developed for large eddy simulation of transitional and turbulent flows [67, 68]. Then it is further developed to incorporate a set of species partial differential equations (PDE) including Nernst-Planck transport equations and a charge conservation equation. The present solver is also coupled with a multi-block approach to allow simulations with complex geometries that fit Cartesian grids. Details on the corresponding mathematical models, the numerical methods and the implementations are provided in the chapters 2 and 3.

Another objective of the present research is to apply the developed solver to simulate and gain an insight into ITP and EKI phenomena in microfluidic devices. To understand the basic behavior and mechanism of the electrokinetic phonomena, one-/two-dimensional simulations are first conducted for ITP and EKI in simple, linear microchannels. The relevant results are given and discussed in Chapter 4. After that, a cross-shaped microchannel with rectangular cross-sections is considered. This more complex and realistic three-dimensional flow geometry is directly relevant to electrokinetic injection studies, electrokinetic mixing schemes, and sample preconcentration processes that make use of conductivity gradients. Three-dimensional simulations are carried out for EKI phenomena in such flow geometry under different

parameters including applied electric field strength, conductivity ratio, channel depth-to-width ratio, and electric field ratio etc. The obtained simulations are compared to the numerical and experimental results available in the literature. The corresponding results and discussions are presented in details in Chapter 5. At the end, Chapter 6 summarizes the current research work and proposes possible further enhancements to the present solver for future work.

2. MATHEMATICAL MODEL

2.1 Theoretical Formulation for EKI

2.1.1 Governing Equations

The governing equations adopted in the present work for simulating EKI in a symmetric binary electrolyte are from the modified Ohmic model of Lin et al. [29]. The Ohmic model, or the so-called leaky dielectric model is frequently used as an excellent approximation to deal with electrohydrodynamics in which electric and flow fields are coupled with each other [69]. Instead of individual ions, bulk quantities of conductivity (σ) and charge density (ρ_e) are tracked in the Ohmic model.

Since magnetic effects can be completely ignored in the absence of external magnetic fields, the electrostatic field $\mathbf{E}$ in electrohydrodynamic systems is solenoidal

$$\nabla \times \mathbf{E} = 0 \tag{2.1}$$

For electrically linear medium, the electric field $\mathbf{E}$ which obeys the Gauss's law simplifies to

$$\nabla \cdot \epsilon \mathbf{E} = \rho_e \tag{2.2}$$

where, ϵ is the permittivity.

For a monovalent binary electrolyte which is fully dissociated, charge density (ρ_e) and electric conductivity (σ) are related to ionic concentrations by [70]

$$\rho_e = F(c_+ - c_-) \tag{2.3}$$

$$\sigma = F^2(c_+ m_+ + c_- m_-) \tag{2.4}$$

where, F is the Faraday constant, $m_\pm$ is the ionic mobility (in mol $\mathrm{N}^{-1} m s^{-1}$), and $c_\pm$ is the cationic/anionic molar concentration.

Under the assumption of electro-neutrality which is a good approximation for most electrolyte solutions (typically with $\sigma > 10^{-4}$ S/m (Siemens per meter)) with fast charge relaxation (typically with the charge relaxation time $\tau_e = \epsilon/\sigma < 10\mu s$), the cationic and anionic molar concentrations are approximately equal to each other [19]

$$c_+ \simeq c_- = c \tag{2.5}$$

where, c is the reduced ionic concentration.

From Equation (2.4), the conductivity is proportional to this reduced concentration and can be simplified by

$$\sigma = F^2(m_+ + m_-)c \tag{2.6}$$

By combining the Nernst-Planck equations for ionic species [71]

$$\frac{\partial c_+}{\partial t} + \nabla \cdot (c_+ \mathbf{u}) = D_+ \nabla^2 c_+ - m_+ F \nabla \cdot (c_+ \mathbf{E}) \tag{2.7}$$

$$\frac{\partial c_-}{\partial t} + \nabla \cdot (c_- \mathbf{u}) = D_- \nabla^2 c_- + m_- F \nabla \cdot (c_- \mathbf{E}) \tag{2.8}$$

and using the electro-neutrality condition (2.5), the electro-diffusion equation, i.e. the conservation equation of conductivity can be derived as

$$\frac{\partial \sigma}{\partial t} + \nabla \cdot \sigma \mathbf{u} = D_{eff} \nabla^2 \sigma \tag{2.9}$$

where, $\mathbf{u}$ is the fluid velocity, and D_{eff} is an effective diffusivity that is defined by

$$D_{eff} = \frac{2 D_+ D_-}{D_+ + D_-} \tag{2.10}$$

where, ionic diffusivity $D_\pm$ can be related to mobility $m_\pm$, the universal gas constant R and the absolute temperature T by Einstein's relation $D_\pm = RTm_\pm$.

The conservation equations of charged species, i.e. Equations (2.7) and (2.8) can be also arranged to yield the charge conservation equation

$$\frac{\partial \rho_e}{\partial t} + \nabla \cdot (\rho_e \mathbf{u}) = \nabla \cdot \mathbf{i}_D - \nabla \cdot (\sigma \mathbf{E}) \tag{2.11}$$

where, $\mathbf{i}_D$ is diffusive current.

Since in electrohydrodynamic systems the applied electric field is typically high, the diffusive current can be safely neglected for most practical cases [72]. This assumption gives $\mathbf{i}_D = 0$. In addition, under the electro-neutrality assumption, $\rho_e = 0$. Then Equation (2.11) can be further simplified as

$$\nabla \cdot (\sigma \mathbf{E}) = 0 \tag{2.12}$$

Notice that the quasi-electrostatic field $\mathbf{E}$ is related the potential ϕ by $\mathbf{E} = -\nabla\phi$, as a result, Equation (2.12) becomes

$$\nabla \cdot (\sigma \nabla \phi) = 0 \tag{2.13}$$

Fluid flow in an electrohydrodynamic system can be governed by the incompressible Navier-Stokes equations with electrical body forces included in the conservation equations of momentum [29]

$$\nabla \cdot \mathbf{u} = 0 \tag{2.14}$$

$$\rho \frac{\partial \mathbf{u}}{\partial t} + \rho \mathbf{u} \cdot \nabla \mathbf{u} = -\nabla p + \mu \nabla^2 \mathbf{u} + \mathbf{F}_e \tag{2.15}$$

where, p is the pressure and μ is the dynamic viscosity. The electrical body forces in the momentum equation (2.15) include both a Coulombic and a polarization component $\mathbf{F}_e = \rho_e \mathbf{E} - \frac{1}{2} E^2 \nabla \epsilon$. However, since a dilute solution of electrolyte does not significantly alter the permittivity of pure water, permittivity gradient is negligible and thus the polarization term drops out of Equation (2.15). This yields the simplified momentum equation as

$$\rho \frac{\partial \mathbf{u}}{\partial t} + \rho \mathbf{u} \cdot \nabla \mathbf{u} = -\nabla p + \mu \nabla^2 \mathbf{u} + \rho_e \mathbf{E} \tag{2.16}$$

It should be pointed out that although the material derivative of charge density ρ_e may often be neglected in the charge conservation equation (2.11) with the electroneutrality assumption, it is not appropriate to neglect the Coulombic body force term $\rho_e \mathbf{E}$ in the momentum Equation (2.16) since it is that force drives the electrohydrodynamic flow.

In summary, to model incompressible, electrically linear leaky dielectrics with rapid charge relaxation and negligible diffusive current for a symmetric binary electrolyte solution, the governing equations can be written as

$$\frac{\partial \sigma}{\partial t} + \mathbf{u} \cdot \nabla \sigma = D_{eff} \nabla^2 \sigma \tag{2.17a}$$

$$\nabla \cdot (\sigma \nabla \phi) = 0 \tag{2.17b}$$

$$\nabla \cdot (\epsilon \mathbf{E}) = \rho_e \tag{2.17c}$$

$$\nabla \cdot \mathbf{u} = 0 \tag{2.17d}$$

$$\rho \frac{\partial \mathbf{u}}{\partial t} + \rho \mathbf{u} \cdot \nabla \mathbf{u} = -\nabla p + \mu \nabla^2 \mathbf{u} + \rho_e \mathbf{E} \tag{2.17e}$$

To non-dimensionalize equations (2.17), the following scales are introduced: $[x, y, z] = w$, $[u, v, w] = U_{ev}$, $[t] = w/U_{ev}, [E] = E_0, [\phi] = E_0 w, [\rho_e] = \epsilon E_0/w, [\sigma] = \sigma_0, [\rho] = \rho_0, [p] = \mu U_{ev}/w, [\zeta] = \zeta_0$. Here, w is the half-width of the microchannel, U_{ev} is the so-called electroviscous velocity and is used as the velocity scale. E_0 is taken to be the value of the characteristic electric field. σ_0 is the characteristic conductivity of the electrolyte solution. ζ_0 is the reference zeta potential. Details about this zeta potential will be discussed in the section 2.1.2.

Then the following set of dimensionless governing equations can be obtained

$$\frac{\partial \sigma^*}{\partial t^*} + \mathbf{u}^* \cdot \nabla \sigma^* = \frac{1}{Ra_e} \nabla^2 \sigma^* \tag{2.18a}$$

$$\nabla \cdot (\sigma^* \nabla \phi^*) = 0 \tag{2.18b}$$

$$\nabla \cdot (\nabla \phi^*) = -\rho_e^* \tag{2.18c}$$

$$\nabla \cdot \mathbf{u}^* = 0 \tag{2.18d}$$

$$Re\left(\frac{\partial \mathbf{u}^*}{\partial t^*} + \mathbf{u}^* \cdot \nabla \mathbf{u}^*\right) = -\nabla p^* + \nabla^2 \mathbf{u}^* - \rho_e^* \nabla \phi^* \tag{2.18e}$$

where the two non-dimensional parameters, the electric Rayleigh number and the Reynolds number are respectively defined by

$$Ra_e \equiv \frac{U_{ev} w}{D_{eff}} \tag{2.19}$$

and

$$Re \equiv \frac{\rho_0 U_{ev} w}{\mu} \tag{2.20}$$

where the electroviscous velocity scale is derived from the balance of viscous and electrical body forces in the momentum equation (2.18e)

$$U_{ev} \equiv \frac{\epsilon E_0^2 w}{\mu} \tag{2.21}$$

2.1.2 Boundary Conditions

Since the characteristic length of the electrical double layer (EDL), which can be called the Debye length (λ_D) is considerably less than the width and height of the microchannel ($\lambda_D < 10nm$), the physics of the EDL only determine the electroosmotic velocity in the immediate vicinity of the microchannel walls [73]. The normal components of velocity, electric field, and conductivity gradient vanish at solid walls. The liquid flow field at solid walls is bounded by a slip plane which excludes the EDLs of the system and at which the electroosmotic velocity is directly proportional to the local electric field [70].

Therefore, the boundary conditions at the walls can be written in the following dimensionless form

$$\mathbf{n}\cdot\nabla\sigma^* = 0 \tag{2.22a}$$

$$\mathbf{n}\cdot\nabla\phi^* = 0 \tag{2.22b}$$

$$\mathbf{n}\cdot\mathbf{u}^* = 0 \tag{2.22c}$$

$$\mathbf{t}\cdot\mathbf{u}^* = \mathbf{t}\cdot\left(-\frac{1}{R_v}\zeta^*\nabla\phi^*\right) \tag{2.22d}$$

where, $\mathbf{t}$ and $\mathbf{n}$ denote the wall-tangential and the wall-normal directions, respectively. Equation (2.22a) is consequence of nonconductive walls and Equation (2.22b) indicates that there is no ion diffusion across the boundaries. Equation 2.22c is the condition that the wall is impenetrable. In Equation (2.22d), the electroosmotic velocity at the wall is given by the Helmholtz-Smoluchowski equation [74]. ζ^* is the zeta-potential of the EDL and its value varies as a function of the ionic concentration, which in return depends on the ionic conductivity for dilute solutions under electro-neutrality conditions. And this dependence introduces well-known dispersive

effects [75]. In modeling the zeta potential, the following empirical correlation can be adopted:

$$\zeta^* = (\sigma^*)^{-k} \tag{2.23}$$

where, k is an empirical constant and can be chosen as 0.3 which is consistent with experimental results of both Yao et al. [76] and Sadr et al. [77].

The nondimensional parameter R_v in Equation (2.22d) is the ratio of electroviscous velocity U_{ev} to electroosmotic velocity U_{eo} defined as [20]

$$R_v \equiv \frac{U_{ev}}{U_{eo}} = \frac{E_0 w}{\zeta_0} \tag{2.24}$$

where the electroosmotic velocity is given by the Helmholtz-Smoluchowski formulation

$$U_{eo} = -\frac{\epsilon E_0 \zeta_0}{\mu} \tag{2.25}$$

The boundary conditions for pressure can be derived and obtained by substituting Equation (2.22d) into the momentum equation (2.18e).

2.1.3 Solution Procedure

To solve the governing equations given in the previous subsection for EKI simulations, based on proper initial conditions velocity field $\mathbf{u}^*$ and pressure field p^* are solved from the incompressible Navier-Stokes equations, i.e. Equations (2.18d) and (2.18e). Then with the velocity field, conductivity σ^* can be obtained by solving the conservation equation of conductivity (2.18a). Using the known conductivity σ^* the charge conservation equation (2.18b) can be solved and thus electric potential ϕ^* is determined. Once the electrolytic Ohmic model is obtained, charge density ρ_e^* can be estimated using Gauss' law, i.e. Equation (2.18c), and thus the electrical body force term can be found. In addition, the slip velocities at walls can be determined using Equation (2.22d) with the obtained conductivity σ^* and electric potential ϕ^* at walls. Finally, velocity and pressure field can be solved from the incompressible Navier-Stokes equations with a determined electrical body force for next time step. The solution procedure is illustrated as shown in Figure 2.1.

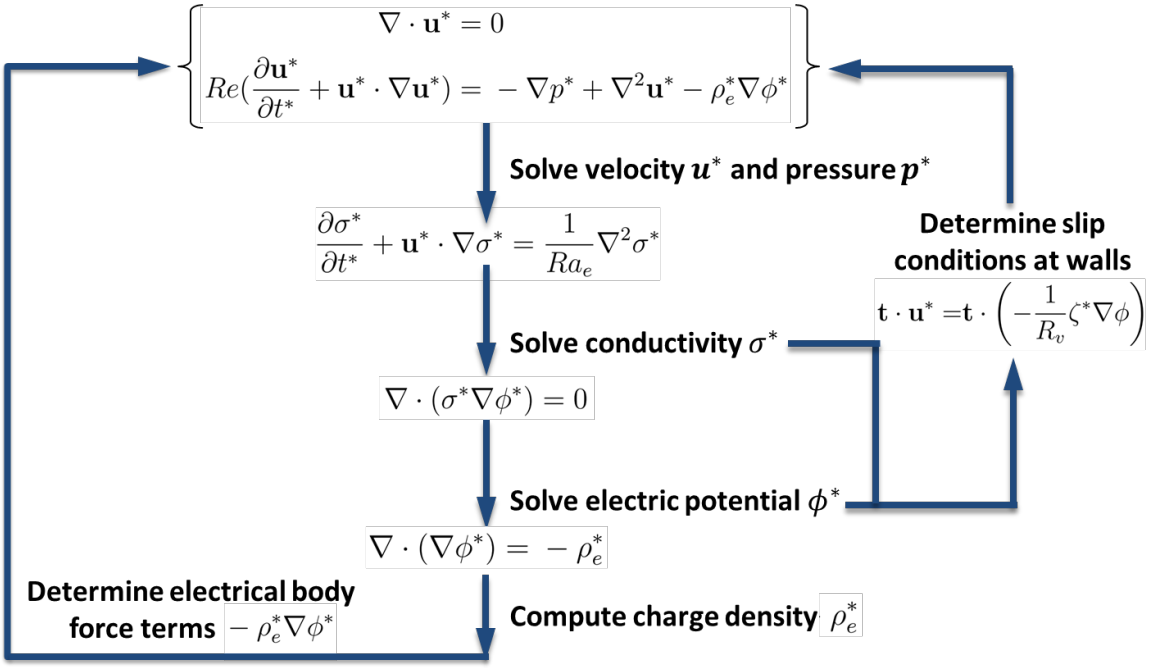

Fig. 2.1. Solution procedure for EKI simulations.

2.2 Theoretical Formulation for ITP

2.2.1 Governing Equations

In Section 2.1 we introduced the theoretical formulation for EKI problems. From the mathematical point of view, the EKI model is a special case of ITP model. In the modeling of ITP, individual speices rather than bulk quantities are computed. The motion of ionized electrolytes in the presence of an applied electric field is governed by their rate of convection, electromigration and diffusion, which are included in the Nersnt-Planck equation [78]

$$\frac{\partial c_i}{\partial t} + \nabla \cdot (\mathbf{u} c_i + z_i \mu_i c_i \mathbf{E} - D_i \nabla c_i) = 0 \tag{2.26}$$

where, $\mathbf{u}$ is the fluid velocity field, c_i, z_i, μ_i, and $D_i = \mu_i RT/F$ is the concentration, the valence, the mobility, and the ionic diffusivity of the ith species respectively.

The multiplication of Equation (2.26) by the Faraday constant F and the species valence z_i, and the summation of all charged species allows to arrive at the charge conservation equation

$$\frac{\partial \rho_e}{\partial t} + \nabla \cdot \mathbf{j} = 0 \tag{2.27}$$

where the free charge density ρ_e is defined as

$$\rho_e = F \sum_i z_i c_i \tag{2.28}$$

and $\mathbf{j}$ is the current density which includes conductive, convective and diffusive components

$$\mathbf{j} = F \left(\mathbf{E} \sum_i z_i^2 \mu_i c_i + \mathbf{u} \sum_i z_i c_i - \sum_i z_i D_i \nabla c_i \right) \tag{2.29}$$

Since in ITP the characteristic length scale of the conductivity interface is typically much larger than the electric length scale associated with regions of significant net charge [39], the contribution of the charge density in Equation (2.27) and the convective term in Equation (2.29) can be neglected. As a result, the electroneutrality approximation can be obtained from Equation (2.28) as

$$\sum_i z_i c_i \approx 0 \tag{2.30}$$

and the charge conservation equation simplifies to

$$\nabla \cdot \left(\mathbf{E} \sum_i z_i^2 \mu_i c_i - \sum_i z_i D_i \nabla c_i \right) = 0 \tag{2.31}$$

Notice the quasi-electrostatic field $\mathbf{E}$ is related the electric potential ϕ by $\mathbf{E} = -\nabla\phi$, then Equation (2.26) can be rewritten as

$$\frac{\partial c_i}{\partial t} + \nabla \cdot [(\mathbf{u} - z_i \mu_i \nabla \phi) c_i] - \nabla \cdot (D_i \nabla c_i) = 0 \tag{2.32}$$

Note that the multiplication of the term $\sum_i z_i^2 \mu_i c_i$ in Equation (2.32) by the Faraday constant F gives the ionic conductivity of the bulk liquid

$$\sigma = F \sum_i z_i^2 \mu_i c_i \tag{2.33}$$

Thus, Equation (2.31) can be expressed as

$$\nabla \cdot (\sigma \nabla \phi) = -F \nabla \cdot \left(\sum_i z_i D_i \nabla c_i \right) \tag{2.34}$$

Fluid flow in ITP is still governed by the incompressible Navier-Stokes equations with electrical body forces, i.e. Equation (2.17e).

In summary, the final form of the dimensional governing equations for ITP can be written as

$$\frac{\partial c_i}{\partial t} + \nabla \cdot [(\mathbf{u} - z_i \mu_i \nabla \phi) c_i] - \nabla \cdot (D_i \nabla c_i) = 0 \tag{2.35a}$$

$$\nabla \cdot (\sigma \nabla \phi) = -F \nabla \cdot \left(\sum_i z_i D_i \nabla c_i \right) \tag{2.35b}$$

$$\rho_e = -\nabla \cdot (\epsilon \nabla \phi) \tag{2.35c}$$

$$\nabla \cdot \mathbf{u} = 0 \tag{2.35d}$$

$$\rho \frac{\partial \mathbf{u}}{\partial t} + \rho \mathbf{u} \cdot \nabla \mathbf{u} = -\nabla p + \eta \nabla^2 \mathbf{u} - \rho_e \nabla \phi \tag{2.35e}$$

Notice here we use η to refer to the dynamic viscosity.

The nondimensional governing equations for ITP will be specifically discussed and given in Section 4.1 when simulating different cases in ITP.

2.2.2 Boundary conditions

In ITP, the boundary conditions at walls are similar to those for EKI. Since the Debye layer thickness is much smaller than the height of the microchannels, the slip velocity condition can be assumed on the channel walls in ITP. We denote such electroosmotic slip velocity along the channel wall for the ith species zone as u_i^{EOF} and it can be determined by the Helmholtz-Smoluchowski's eqaution as [79]

$$\mathbf{u}_i^{EOF} = \mu_i^{EOF} \mathbf{E}_i \tag{2.36}$$

where, $\mathbf{E}_i$ and μ_i^{EOF} are the electric field and the electroosmotic mobility in the corresponding ith species zone respectively.

Thus, in ITP the boundary conditions at the walls can be written as

$$\mathbf{n}\cdot\nabla c_i = 0 \tag{2.37a}$$

$$\mathbf{n}\cdot\nabla\phi = 0 \tag{2.37b}$$

$$\mathbf{n}\cdot\mathbf{u} = 0 \tag{2.37c}$$

$$\mathbf{t}\cdot\mathbf{u} = \mathbf{t}\cdot\left(\mu_i^{EOF}\mathbf{E}_i\right) \tag{2.37d}$$

where, $\mathbf{t}$ and $\mathbf{n}$ denote the wall-tangential and the wall-normal directions, respectively.

2.2.3 Solution Procedure

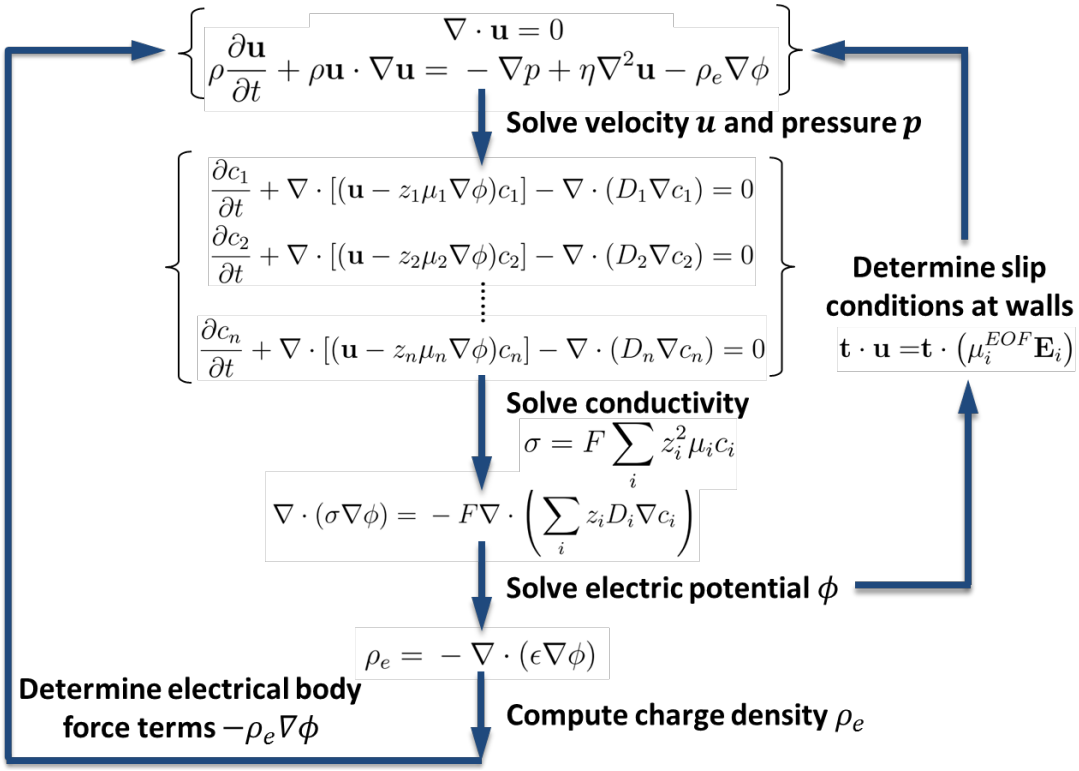

Fig. 2.2. Solution procedure for ITP simulations.

The procedure for solving the governing equations for ITP simulations is similar to that for EKI simulations. The solution procedure for ITP simulations is described as shown in Figure 2.2. Based on proper initial conditions, velocity field $\mathbf{u}$ and pressure

field p are solved from the incompressible Navier-Stokes equations, i.e. Equations (2.35d) and (2.35e). Then with the velocity field, ionic concentration for each species can be obtained by solving a number of Nernst-Planck transport equations like Equation (2.35a) (for example, if there are n species considered in the system, n Nernst-Planck equations need to be solved). According to Equation (2.33), conductivity σ can be evaluated from the ionic concentration of the species. Using the known conductivity σ the charge conservation equation (2.35b) can be solved and thus electric potential ϕ is determined. Charge density ρ_e then can be estimated using Gauss' law, i.e. Equation (2.35c), and the electrical body force term can be found. In addition, the slip velocities at walls can be determined using Equation (2.37d) with the obtained electric potential ϕ at walls (notice the local electric field $\mathbf{E}_i$ is computed using electric potential ϕ at walls in the corresponding species zones). Finally, velocity and pressure field can be solved from the incompressible Navier-Stokes equations with a determined electrical body force for next time step.

3. COMPUTATIONAL METHODOLOGY

The present solver is developed based on a high-order accurate LES solver for simulating transitional and turbulent flows by Shetty et al. [67]. The incompressible Navier-Stokes equations (2.18d) and (2.18e) are solved in a predictor/corrector manner using a fractional time stepping scheme. The time integration is performed by adopting a third-order accurate backward difference (BDF) scheme [80]. The convective terms are discretized by a fifth-order Weighted Essentially Non-Oscillatory (WENO) scheme [81], and the viscous terms are discretized using central finite difference schemes. Ghost points near the boundaries outside the fluid domain are used to maintain the order of accuracy of the spatial discretization by following a Stokes flow boundary condition provided by Morinishi et al. [82]. In a similar way, the species transport equations (2.18a) or (2.35a) are solved using the WENO scheme for the convective terms, the central finite difference schemes for the viscous terms and the fractional time stepping BDF scheme for the time advancement. The elliptic partial differential equations, i.e. the pressure Poisson equation for correcting velocities and the charge conservation equation, are solved using MUDPACK libraries in the 2D version of the solver and using the MPI libraries based *hypre* solver [83] in the 3D version of the solver, respectively.

In order to make the computation of the pressure gradient a bit easier in the correction step of the time advancement, and also to avoid odd-even decoupling issue between the pressure and velocity which may lead to checkerboard patterns in the solutions, a staggered grid is adopted for the computational domain in which the velocity components u, v and w are stored at mid points between the vertices along x-, y-, and z-axis respectively while the values of pressure are located at the vertices. A schematic of such staggered grid used in the solver is shown in Figure 3.1.

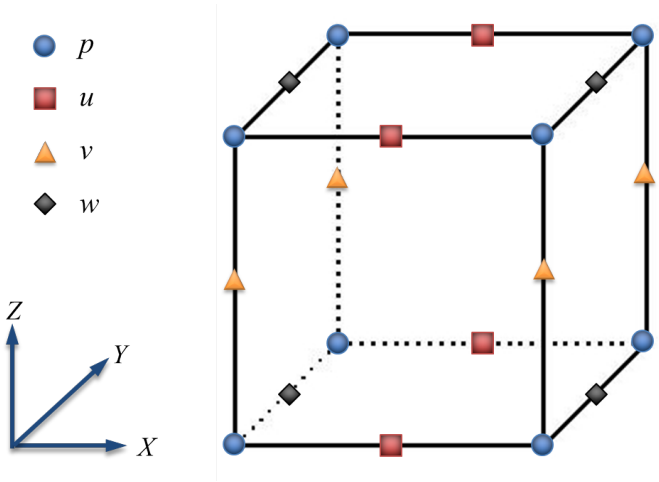

Fig. 3.1. Schematic of the staggered grid used in the present solver.

3.1 Time Integration

The incompressible Navier-Stokes equations are integrated through a fractional time stepping algorithm. In the prediction step, velocity components are predicted by solving the momentum equations (2.18e) without considering the pressure gradient term. The fully explicit third-order accurate BDF scheme used for the time integration in this step can be written as

$$\frac{\alpha_1 u_i^* - (\alpha_2 u_i^n + \alpha_3 u_i^{n-1} + \alpha_4 u_i^{n-2})}{\Delta t} + NLCT_i - VISC_i - EBF_i = 0 \tag{3.1}$$

where, $\alpha_1 = 11/6$, $\alpha_2 = 3$, $\alpha_3 = -3/2$, and $\alpha_4 = 1/3$. u^* is the predicted velocity value. $NLCT_i$, $VISC_i$ and EBF_i refer to the non-linear convective terms, viscous terms and electric body force terms respectively which are expressed as

$$NLCT_i = 2\left(u_j \frac{\partial u_i}{\partial x_j}\right)^n - \left(u_j \frac{\partial u_i}{\partial x_j}\right)^{n-1} \tag{3.2a}$$

$$VISC_i = 2\left(\frac{1}{Re}\frac{\partial^2 u_i}{\partial x_j \partial x_j}\right)^n - \left(\frac{1}{Re}\frac{\partial^2 u_i}{\partial x_j \partial x_j}\right)^{n-1} \tag{3.2b}$$

$$EBF_i = 2\left[\frac{1}{Re}\left(\frac{\partial^2 \phi}{\partial x_j \partial x_j}\right)\frac{\partial \phi}{\partial x_i}\right]^n - \left[\frac{1}{Re}\left(\frac{\partial^2 \phi}{\partial x_j \partial x_j}\right)\frac{\partial \phi}{\partial x_i}\right]^{n-1} \tag{3.2c}$$

During the correction step, the pressure field is then obtained by using the predicted velocity to solve the following Poisson equation

$$\frac{\partial^2 p^{n+1}}{\partial x_i \partial x_i} = \frac{\alpha_1 Re}{\Delta t} \frac{\partial u_i^*}{\partial x_i} \tag{3.3}$$

In the end, the predicted velocity is corrected by the pressure field to obtain the final velocity field by

$$u_i^{n+1} = u_i^* - \frac{\Delta t}{\alpha_1 Re} \frac{\partial p^{n+1}}{\partial x_i} \tag{3.4}$$

For inertial flows ($Re > 1$), explicit methods do not impose a too severe restriction on the time step so that numerical solutions can be obtained in reasonable time. However, in low Reynolds number flows, for example, when Reynolds numbers are of order 10^{-1} or smaller which can be easily found in electrokinetic flows in microfluidic devices, as the viscosity is high the viscous term become a source of stiffness [84]. As a result, explicit methods have a stringent stability restriction leading to very small time steps [85].

In order to improve the efficiency and stability of the present solver, a semi-implicit third-order BDF is used for the time integration where the viscous term is treated implicitly while the nonlinear convective terms and the electrical body force term are still computed explicitly. Then Equation (2.34) for the time integration in the prediction step would be modified to

$$\frac{\alpha_1 u_i^* - (\alpha_2 u_i^n + \alpha_3 u_i^{n-1} + \alpha_4 u_i^{n-2})}{\Delta t} - VISC_i^* = -NLCT_i + EBF_i \tag{3.5}$$

where, the non-linear convective terms $NLCT_i$ and the electrical body force terms EBF_i are the same as given in Equations (2.35a) and (2.35c) respectively, while the viscous terms are expressed in terms of the predicted velocity u^*

$$VISC_i^* = \frac{1}{Re} \frac{\partial^2 u_i^*}{\partial x_j \partial x_j} \tag{3.6}$$

At each time step in the prediction stage, the predicted velocity will be obtained simultaneously throughout the computational domain by solving a system of equations to eliminate the numerical viscous stability restriction. In the present solver, the solution of the predicted velocity is obtained by using the *hypre* library in parallel.

To validate the semi-implicit method, the present solver is applied for a two-dimensional straight microfluidic channel since it is a widely used benchmark test case for microfluidic applications [86]. An analytical solution exists for the fully developed laminar velocity profile that has to be obtained at the outlet of the micro-channel. By comparing the computational results obtained by the semi-implicit method and the explicit method to the analytical solution at a given low Reynolds number of $Re = 0.1$ for a size of $100\mu m \times 10\mu m$ straight microchannel using 180×40 grid points, it was found that for a sufficient accuracy the time step of the semi-implicit method can be chosen as about 20 times larger than the explicit method. Notice that the semi-implicit method is about twice as costly as the explicit method. As a result, the semi-implicit method is overall about 10 times more efficient than the explicit method for time integration.

The convection-diffusion transport equations can be solved in a similar way but with no correction step because there are no gradient terms in the equations. For such scalar equations, the unknown scalar Q can be directly solved by the third-order BDF scheme for the time advancement which is

$$\frac{\alpha_1 Q^{n+1} - (\alpha_2 Q^n + \alpha_3 Q^{n-1} + \alpha_4 Q^{n-2})}{\Delta t} + NLCT - VISC = 0 \tag{3.7}$$

For EKI applications, the non-linear convective term $NLCT$ and the viscous term $VISC$ in Equation (2.18a) are defined by

$$NLCT = 2\left(\hat{u}_j \frac{\partial Q}{\partial x_j}\right)^n - \left(\hat{u}_j \frac{\partial Q}{\partial x_j}\right)^{n-1} \tag{3.8a}$$

$$VISC = 2\left(\frac{1}{Ra_e}\frac{\partial^2 Q}{\partial x_j \partial x_j}\right)^n - \left(\frac{1}{Ra_e}\frac{\partial^2 Q}{\partial x_j \partial x_j}\right)^{n-1} \tag{3.8b}$$

where, $\hat{u}_j = u_j$ is the velocity of the bulk flow, and Q refers to the electrical conductivity of the bulk liquid.

For ITP applications, the non-linear convective term $NLCT$ and the viscous term $VISC$ in Equation (2.35a) are defined by

$$NLCT = 2\left(\frac{\partial(\hat{u}_j Q)}{\partial x_j}\right)^n - \left(\frac{\partial(\hat{u}_j Q)}{\partial x_j}\right)^{n-1} \tag{3.9a}$$

$$VISC = 2\left(D\frac{\partial^2 Q}{\partial x_j \partial x_j}\right)^n - \left(D\frac{\partial^2 Q}{\partial x_j \partial x_j}\right)^{n-1} \tag{3.9b}$$

where, $\hat{u}_j = u_j - z\mu\frac{\partial\phi}{\partial x_j}$ includes the velocity of the bulk flow and the ion velocity due to electromigration. z, μ, Q refer to the ionic valence, mobility and concentration of each individual species, respectively.

3.2 Spatial Discretization

In solving both the incompressible Navier-Stokes equations and the conservation equation of conductivity, the non-linear convective terms are computed using a fifth-order WENO scheme to achieve high-order accuracy. The key idea in WENO schemes is to use a non-linear adaptive procedure to automatically choose the locally smoothest stencil to avoid crossing discontinuities in the interpolation procedure as much as possible, and hence to obtain a higher order accurate approximation. By following the approach by Zhang and Jackson [87], any variable f under consideration can be reconstructed as

$$f_{j+1/2} = \sum_{k=1}^{3} \omega_k f^k_{j+1/2} \tag{3.10}$$

where, $f^k_{j+1/2}$ is a second order polynomial reconstruction of f on the k_{th} set of stencils and the nonlinear weights ω_k are

$$\omega_k = \frac{\tilde{\omega}_k}{\sum_{l=1}^{3} \tilde{\omega}_l} \tag{3.11a}$$

$$\tilde{\omega}_l = \frac{\gamma_l}{(\epsilon + \beta_l)^2} \tag{3.11b}$$

If $u_{j+1/2} \geq 0$ then $\gamma_1 = 0.3$, $\gamma_2 = 0.6$, $\gamma_3 = 0.1$ and $f^k_{j+1/2}$ is computed by

$$f^1_{j+1/2} = \frac{1}{3}f_j + \frac{5}{6}f_{j+1} - \frac{1}{6}f_{j+2} \tag{3.12a}$$

$$f^2_{j+1/2} = -\frac{1}{6}f_{j-1} + \frac{5}{6}f_j + \frac{1}{3}f_{j+1} \tag{3.12b}$$

$$f^3_{j+1/2} = \frac{1}{3}f_{j-2} - \frac{7}{6}f_{j-1} + \frac{11}{6}f_j \tag{3.12c}$$

with the smoothness indicators β_l

$$\beta_1 = \frac{13}{12}(f_j - 2f_{j+1} + f_{j+2})^2 + \frac{1}{4}(3f_j - 4f_{j+1} + fj + 2)^2 \tag{3.13a}$$

$$\beta_2 = \frac{13}{12}(f_{j-1} - 2f_j + f_{j+1})^2 + \frac{1}{4}(f_{j-1} - f_{j+1})^2 \tag{3.13b}$$

$$\beta_3 = \frac{13}{12}(f_{j-2} - 2f_{j-1} + f_j)^2 + \frac{1}{4}(f_{j-2} - 4f_{j-1} + 3fj)^2 \tag{3.13c}$$

For $u_{j+1/2} < 0$ then $\gamma_1 = 0.1$, $\gamma_2 = 0.6$, $\gamma_3 = 0.3$ and $f^k_{j+1/2}$ is computed by

$$f^1_{j+1/2} = \frac{11}{6}f_{j+1} - \frac{7}{6}f_{j+2} + \frac{1}{3}f_{j+3} \tag{3.14a}$$

$$f^2_{j+1/2} = \frac{1}{3}f_j + \frac{5}{6}f_{j+1} - \frac{1}{6}f_{j+2} \tag{3.14b}$$

$$f^3_{j+1/2} = -\frac{1}{6}f_{j-1} + \frac{5}{6}f_j + \frac{1}{3}f_{j+1} \tag{3.14c}$$

with the smoothness indicators β_l

$$\beta_1 = \frac{13}{12}(f_{j+1} - 2f_{j+2} + f_{j+3})^2 + \frac{1}{4}(3f_{j+1} - 4f_{j+2} + fj + 3)^2 \tag{3.15a}$$

$$\beta_2 = \frac{13}{12}(f_j - 2f_{j+1} + f_{j+2})^2 + \frac{1}{4}(f_j - f_{j+2})^2 \tag{3.15b}$$

$$\beta_3 = \frac{13}{12}(f_{j-1} - 2f_j + f_{j+1})^2 + \frac{1}{4}(f_{j-1} - 4f_j + 3fj + 1)^2 \tag{3.15c}$$

Finally, the gradient of the function f is calculated from the above reconstructed fluxes by

$$\frac{\partial f}{\partial x_i} = \frac{f_{j+1/2} - f_{j-1/2}}{\Delta x_i} \tag{3.16}$$

The viscous terms in the momentum equations are discretized by a second-order accurate central difference scheme when using the semi-implicit method. The viscous terms in the scalar transport equations or the other second-order derivatives in the

governing equations are computed using the following fourth-order accurate central difference scheme

$$\frac{\partial^2 f_i}{\partial x_j^2} = \frac{1}{\Delta x_j^2}\left(-\frac{1}{12}(f_{j-2} + f_{j+2}) + \frac{4}{3}(f_{j-1} + f_{j+1} - \frac{5}{2}f_i)\right) \tag{3.17}$$

In addition, a fourth-order accurate central difference scheme is also adopted for the first-order derivatives involved in the governing equations

$$\frac{\partial f_i}{\partial x_j} = \frac{1}{\Delta x_j}\left(\frac{1}{12}(f_{j-2} + f_{j+2}) + \frac{2}{3}(f_{j-1} + f_{j+1})\right) \tag{3.18}$$

3.3 Solution of Predicted Velocity

With the semi-implicit scheme, the present solver implicitly solves the predicted velocity in the prediction stage at each time step by using the *hypre* library [83] in parallel. Preconditioned conjugate gradient (PCG) method with geometric multigrid as the preconditioner is adopted.

The viscous terms in the momentum equations are discretized by a second-order central difference operator. Thus, if we take the x-momentum equation as an example for solving the predicted velocity component u^*, the x-component of the viscous term in Equation (3.6) can be written as

$$VISC_x^* \Big|_{i,j,k} = \frac{1}{Re}\left[\frac{\partial^2 u^*}{\partial x^2} + \frac{\partial^2 u^*}{\partial y^2} + \frac{\partial^2 u^*}{\partial z^2}\right]_{i,j,k} \tag{3.19}$$

with

$$\frac{\partial^2 u^*}{\partial x^2}\Big|_{i,j,k} = \frac{u^*_{i+1,j,k} - 2u^*_{i,j,k} + u^*_{i-1,j,k}}{\Delta x^2} \tag{3.20a}$$

$$\frac{\partial^2 u^*}{\partial y^2}\Big|_{i,j,k} = \frac{u^*_{i,j+1,k} - 2u^*_{i,j,k} + u^*_{i,j-1,k}}{\Delta y^2} \tag{3.20b}$$

$$\frac{\partial^2 u^*}{\partial z^2}\Big|_{i,j,k} = \frac{u^*_{i,j,k+1} - 2u^*_{i,j,k} + u^*_{i,j,k-1}}{\Delta z^2} \tag{3.20c}$$

where, Δx, Δy and Δz are the grid sizes in x, y and z directions respectively.

Then the left hand side of Equation (3.5) has the form

$$\begin{aligned}
&\left[\frac{\alpha_1 u^* - (\alpha_2 u^n + \alpha_3 u^{n-1} + \alpha_4 u^{n-2})}{\Delta t} - \frac{1}{Re}\left(\frac{\partial^2 u^*}{\partial x^2} + \frac{\partial^2 u^*}{\partial y^2} + \frac{\partial^2 u^*}{\partial z^2}\right)\right]_{i,j,k} \\
=&\frac{\alpha_1 u^*_{i,j,k} - (\alpha_2 u^n_{i,j,k} + \alpha_3 u^{n-1}_{i,j,k} + \alpha_4 u^{n-2}_{i,j,k})}{\Delta t} - \frac{1}{Re}\frac{u^*_{i+1,j,k} - 2u^*_{i,j,k} + u^*_{i-1,j,k}}{\Delta x^2} \\
&- \frac{1}{Re}\frac{u^*_{i+1,j,k} - 2u^*_{i,j,k} + u^*_{i-1,j,k}}{\Delta y^2} - \frac{1}{Re}\frac{u^*_{i+1,j,k} - 2u^*_{i,j,k} + u^*_{i-1,j,k}}{\Delta z^2}
\end{aligned} \tag{3.21}$$

To implicitly solve the predicted velocity component u^*, we rearrange the above equation such that only the variable u^* is included in one side of the equation. As a result, the Equation (3.5) arrives at

$$\begin{aligned}
&\left[\alpha_1 + \frac{2\Delta t}{Re}\left(\frac{1}{\Delta x^2} + \frac{1}{\Delta y^2} + \frac{1}{\Delta z^2}\right)\right] u^*_{i,j,k} - \frac{\Delta t}{Re\Delta x^2}\left(u^*_{i+1,j,k} + u^*_{i-1,j,k}\right) \\
&- \frac{\Delta t}{Re\Delta y^2}\left(u^*_{i,j+1,k} + u^*_{i,j-1,k}\right) - \frac{\Delta t}{Re\Delta z^2}\left(u^*_{i,j,k+1} + u^*_{i,j,k-1}\right) \\
&= \alpha_2 u^n + \alpha_3 u^{n-1} + \alpha_4 u^{n-2} - NLCT_x \Delta t + EBF_x \Delta t
\end{aligned} \tag{3.22}$$

where, $NLCT_x$ and EBF_x are the x-components of the non-linear convective terms and the electrical body force terms respectively. Notice these two terms are explicitly evaluated by the fifth-order WENO scheme or the fourth-order central difference scheme in the computation. In a similar way, the y- and z-components of the predicted velocity can be implicitly solved as well.

To impose the Dirichlet boundary conditions using a conjugate gradient method, a symmetric matrix is formed to solve the system. For example, if the grid along x-direction is $i = 0, 1, ..., N-1, N$ where $i = 0$ is the left boundary while $i = N$ is the right boundary, when a Dirichlet boundary condition needs to be applied at the right boundary, i.e. $i = N$, all the entries of the coefficient matrix at the grid node $i = N - 1$ that have the coefficients associated with the known Dirichlet value at $i = N$ need to be transfered to the right hand side vector of the linear system. In this way, Dirichlet boundary conditions can be guaranteed.

3.4 Solution of Elliptic PDEs

The pressure Poisson equation (3.3) involved in the fractional time step method and the charge conservation equation (2.18b) or (2.35b) need to be solved at every time step of the EKI or ITP simulation. Both of them are elliptic PDEs. In the present solver, these two equations are solved on a multiblock grid by using the *hypre* library [83] in parallel. Again, PCG method with geometric multigrid as the preconditioner is adopted.

Discretization of these two elliptic PDE is done by a second-order central difference operator. This results in the left hand side of the pressure Poisson equation (3.3) to be written as

$$\nabla^2 p \Big|_{i,j,k} = \left[\frac{\partial^2 p}{\partial x^2} + \frac{\partial^2 p}{\partial y^2} + \frac{\partial^2 p}{\partial z^2}\right]_{i,j,k} \tag{3.23}$$

where,

$$\frac{\partial^2 p}{\partial x^2}\Big|_{i,j,k} = \frac{p_{i+1,j,k} - 2p_{i,j,k} + p_{i-1,j,k}}{\Delta x^2} \tag{3.24a}$$

$$\frac{\partial^2 p}{\partial y^2}\Big|_{i,j,k} = \frac{p_{i,j+1,k} - 2p_{i,j,k} + p_{i,j-1,k}}{\Delta y^2} \tag{3.24b}$$

$$\frac{\partial^2 p}{\partial z^2}\Big|_{i,j,k} = \frac{p_{i,j,k+1} - 2p_{i,j,k} + p_{i,j,k-1}}{\Delta z^2} \tag{3.24c}$$

and the right hand side of the equation can be written as

$$\frac{\alpha_1 Re}{\Delta t}\nabla \cdot \mathbf{u}\Big|_{i,j,k} = \frac{\alpha_1 Re}{\Delta t}\left[\frac{\partial u}{\partial x} + \frac{\partial v}{\partial y} + \frac{\partial w}{\partial z}\right]_{i,j,k} \tag{3.25}$$

with

$$\frac{\partial u}{\partial x}\Big|_{i,j,k} = \frac{u_{i+1/2,j,k} - u_{i-1/2,j,k}}{\Delta x} \tag{3.26a}$$

$$\frac{\partial v}{\partial y}\Big|_{i,j,k} = \frac{v_{i,j+1/2,k} - v_{i,j-1/2,k}}{\Delta y} \tag{3.26b}$$

$$\frac{\partial w}{\partial z}\Big|_{i,j,k} = \frac{w_{i,j,k+1/2} - w_{i,j,k-1/2}}{\Delta z} \tag{3.26c}$$

where, Δx, Δy and Δz are the grid sizes in x, y and z directions respectively. Δt is the time step used in the computation.

In a similar way, the left hand side of the charge conservation equation (2.18b) or (2.35b) can be discretized by

$$\nabla \cdot (\sigma \nabla \phi) \Big|_{i,j,k} = \left[\sigma \left(\frac{\partial^2 \phi}{\partial x^2} + \frac{\partial^2 \phi}{\partial y^2} + \frac{\partial^2 \phi}{\partial z^2} \right) + \frac{\partial \sigma}{\partial x} \frac{\partial \phi}{\partial x} + \frac{\partial \sigma}{\partial y} \frac{\partial \phi}{\partial y} + \frac{\partial \sigma}{\partial z} \frac{\partial \phi}{\partial z} \right]_{i,j,k} \tag{3.27}$$

where,

$$\sigma \frac{\partial^2 \phi}{\partial x^2} \Big|_{i,j,k} = \sigma_{i,j,k} \frac{\phi_{i+1,j,k} - 2\phi_{i,j,k} + \phi_{i-1,j,k}}{\Delta x^2} \tag{3.28a}$$

$$\sigma \frac{\partial^2 \phi}{\partial y^2} \Big|_{i,j,k} = \sigma_{i,j,k} \frac{\phi_{i,j+1,k} - 2\phi_{i,j,k} + \phi_{i,j-1,k}}{\Delta y^2} \tag{3.28b}$$

$$\sigma \frac{\partial^2 \phi}{\partial z^2} \Big|_{i,j,k} = \sigma_{i,j,k} \frac{\phi_{i,j,k+1} - 2\phi_{i,j,k} + \phi_{i,j,k-1}}{\Delta x^2} \tag{3.28c}$$

$$\frac{\partial \sigma}{\partial x} \frac{\partial \phi}{\partial x} = \frac{\partial \sigma}{\partial x} \Big|_{i,j,k} \frac{\phi_{i+1,j,k} - \phi_{i-1,j,k}}{2\Delta x} \tag{3.28d}$$

$$\frac{\partial \sigma}{\partial y} \frac{\partial \phi}{\partial y} = \frac{\partial \sigma}{\partial y} \Big|_{i,j,k} \frac{\phi_{i,j+1,k} - \phi_{i,j-1,k}}{2\Delta y} \tag{3.28e}$$

$$\frac{\partial \sigma}{\partial z} \frac{\partial \phi}{\partial z} = \frac{\partial \sigma}{\partial z} \Big|_{i,j,k} \frac{\phi_{i,j,k+1} - \phi_{i,j,k-1}}{2\Delta z} \tag{3.28f}$$

Notice that in the above equations, σ and its derivatives $\frac{\partial \sigma}{\partial x}$, $\frac{\partial \sigma}{\partial y}$, $\frac{\partial \sigma}{\partial z}$ are obtained using Equation (2.18a) or (2.35a) and their values are known when solving Equation (2.18b) or (2.35b).

3.5 Multiblock Approach

The present solver has the capability to handle complex geometries that would fit Cartesian grids by utilizing a multiblock approach. Multiple blocks are arranged to exactly cover the flow geometry. Equal blocks with uniform mesh size are used so that the block interfaces are conformal thus no interpolation are required at the block-interfaces. Each block is assigned to one parallel processor. And for each of the blocks, the inlet/outlet or wall faces, or the interfaces to communicate with other adjacent blocks are clearly identified according to the locations of the blocks in the flow geometry. Accordingly, during the computation the solver then will automatically impose the boundary conditions or perform the proper communications at the faces.

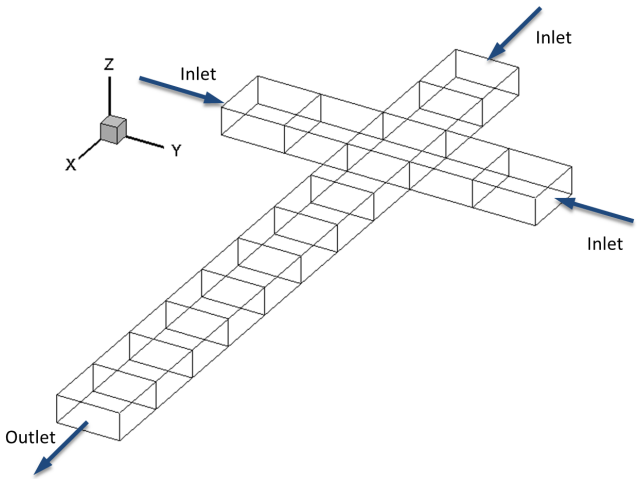

(a) A cross-shaped channel geometry

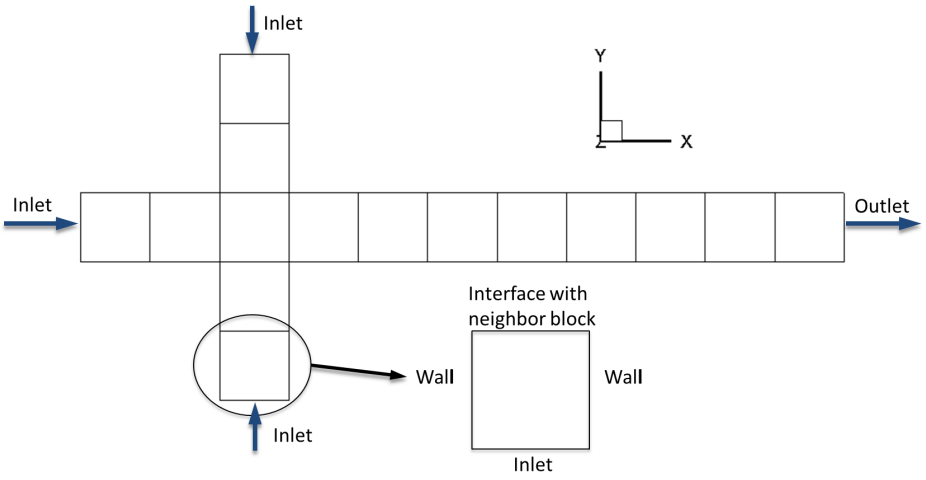

(b) Top view of the channel geometry

Fig. 3.2. Schematic of a cross-shaped channel covered by multiple blocks.

For example, 15 blocks can be used to compose the flow geometry for a cross-shaped channel with a rectangular cross-section as shown in Figure 3.2 (a). Figure 3.2 (b) indicates the top view of the channel and the block at the bottom location is picked to show the identified faces on it. Suppose only four sides of the block are considered from the top view. According to the flow geometry, the bottom side then is identified as the inlet boundary condition, the left and right sides are the wall conditions while the the top side is the interface used to communicate with the above

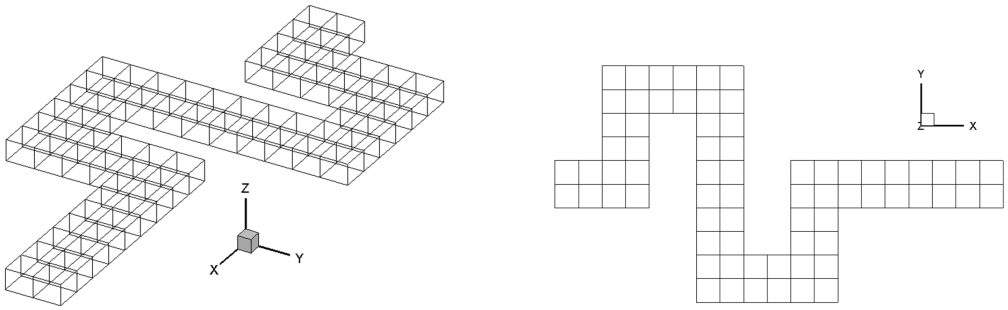

(a) A snake-like channel geometry (b) Top view of the channel geometry

Fig. 3.3. Schematic of a rectangular serpentine channel covered by multiple blocks.

adjacent block. Another example is a rectangular serpentine microchannel as shown in Figure 3.3. 70 blocks are arranged to cover this flow geometry. Though it looks more complicated than the cross-shaped geometry, the solver can still handle it using the multiblock approach as long as the geometry fits the Cartesian grid.

4. ONE-/TWO-DIMENSIONAL NUMERICAL STUDY OF ITP AND EKI IN STRAIGHT MICROCHANNELS

4.1 Simulation of ITP in One-/Two-dimensional Straight Microchannels

Isotachophoresis (ITP) is a common method in the field of analytical chemistry and it has proven to be a powerful technique for sample concentration, separation, and for detection of analytes in microfluidic devices [88, 89]. This technique is based on the difference of migration speed of ionic species under an electric field. In ITP, sample ions are focused between a high mobility leading electrolyte (LE), and a low mobility trailing electrolyte (TE) and they are arranged to migrate in the order of their electrophoretic mobilities when an electric field is applied. Depending on the amount of the sample present in the system, ITP falls in two modes, plateau mode and peak mode. In plateau mode ITP, ionic species form distinct and separate zones with sufficiently high concentrations [90]. In contrast, peak mode ITP arises if one or more ionic species focus at the sharp electric field gradient between the LE and TE zones with sufficiently low concentrations such that their effect on the electric field is negligible [91]. In this section 4.1, we first simulate one-dimensional ideal ITP without sample analytes to test and validate the present solver. Then we conduct two-dimensional simulations to investigate how different parameters including channel height, electrophoretic mobility ratio, and sample amount present in the channel affect the dispersed plateau/peak mode in ITP with Poiseuille counterflow.

4.1.1 One-dimensional Ideal ITP without Sample Analytes

In order to numerically study isotachophoretic phenomena and also to test the performance of the present WENO solver for ITP, we start with the simplest 1D ITP

case in which we ignore the bulk flow (i.e. not solving the Navier-Stokes equations for pressure and velocity fields), but only solve the charge conservation equation and the scalar transport equations for the electric field and three species including the trailing (TE) and leading electrolyte (LE) with respectively higher and lower effective ion mobility and the counter-ionized species (CI). Under the application of an electric field, both TE and LE buffers migrate at the same speed U_{ITP}, see Figure 4.1.

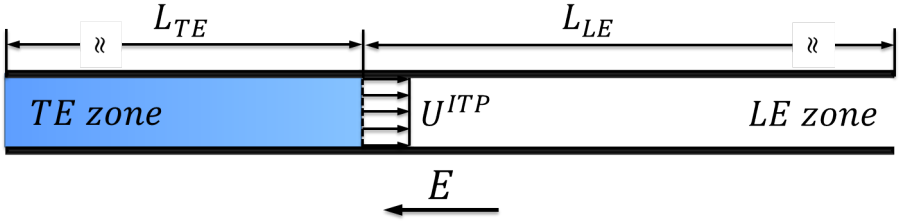

Fig. 4.1. Schematic of one-dimensional ideal ITP without sample analytes.

For such simplest ITP case, the one-dimensional convection-diffusion scalar transport equations and the charge conservation equation become

$$\frac{\partial c_i}{\partial t} = -\frac{\partial}{\partial x}\left(-z_i\mu_i\frac{\partial \phi}{\partial x}c_i\right) + D_i\frac{\partial^2 c_i}{\partial x^2} \tag{4.1a}$$

$$\sigma\frac{\partial^2 \phi}{\partial x^2} + \frac{\partial \sigma}{\partial x}\frac{\partial \phi}{\partial x} = -F\sum_i\left(z_i D_i\frac{\partial^2 c_i}{\partial x^2}\right) \tag{4.1b}$$

where the subscript i = TE, LE, or CI, refers to the trailing electrolyte, leading electrolyte and the counter ionized electrolyte respectively.

To simplify the computation, the concentration of the counter ion can be obtained by using the electroneutrality approximation instead of solving the transport equation. As a result, the system of governing equations for the case can be written as

$$\frac{\partial c_i}{\partial t} = -\frac{\partial}{\partial x}\left(-z_i\mu_i\frac{\partial \phi}{\partial x}c_i\right) + D_i\frac{\partial^2 c_i}{\partial x^2} \qquad \text{for i = TE, LE} \tag{4.2a}$$

$$c_{CI} = -(z_{TE}c_{TE} + z_{LE}c_{LE})/z_{CI} \tag{4.2b}$$

$$\sigma\frac{\partial^2 \phi}{\partial x^2} + \frac{\partial \sigma}{\partial x}\frac{\partial \phi}{\partial x} = -F\sum_i\left(z_i D_i\frac{\partial^2 c_i}{\partial x^2}\right) \qquad \text{for i = TE, LE, CI} \tag{4.2c}$$

The domain considered in the present simulation is a $L = 10mm$ long, $w = 40\mu m$ wide circular microchannel. The lengths of the TE and LE zones are denoted by L_{TE} and L_{LE} respectively, and $L = L_{TE} + L_{LE}$. The TE zone is on the left while the LE zone is on the right, and the LE-TE interface is set at $L_{TE}/L = 0.4$. The parameters used in the simulation are listed in Table 4.1.

Table 4.1
Simulation parameters for one-dimensional ideal ITP case.

Symbol	Description	Value
w	Width of the channel	$4.0 \times 10^{-5}[m]$
c^0_{LE}	LE ion total concentration - LE zone	$100.0[mM]$
c^0_{TE}	TE ion total concentration - TE zone	$100.0[mM]$
μ_{LE}	LE effective mobility	$68.5 \times 10^{-9}[m^2 \cdot V^{-1}s^{-1}]$
μ_{TE}	TE effective mobility	$18.22 \times 10^{-9}[m^2 \cdot V^{-1}s^{-1}]$
μ_{CI}	CI effective mobility	$6.60 \times 10^{-9}[m^2 \cdot V^{-1}s^{-1}]$
z_{LE}	valence of LE	-1
z_{TE}	valence of TE	-1
z_{CI}	valence of CI	$+1$
R	Gas constant	$8.31[J \cdot mol^{-1}K^{-1}]$
T	Temperature	$298[K]$
F	Faraday's constant	$9.65 \times 10^4[C \cdot mol^{-1}]$

The boundary conditions imposed at the inlet are

$$\phi = 0; \quad c_{TE} = c^0_{TE}; \quad c_{LE} = 0; \quad c_{CI} = c^0_{TE} \tag{4.3}$$

At the outlet, a constant current density $j_{applied}$ is applied. From the charge conservation equation, the current density for a one-dimensional problem can be expressed as

$$j_{applied} = F\left(-\frac{\partial \phi}{\partial x}\sum_i z_i^2 \mu_i c_i - \sum_i z_i D_i \frac{\partial c_i}{\partial x}\right) \tag{4.4}$$

Since the outlet is set to be sufficiently far away from the transient interface, all the species concentrations at the outlet are assumed constant. Then the term $\sum_i z_i D_i \frac{\partial c_i}{\partial x}$ drops out and the gradient of the electric potential at the outlet arrives at

$$\frac{\partial \phi}{\partial x} = -\frac{j_{applied}}{F \sum_i z_i^2 \mu_i c_i} = -\frac{j_{applied}}{\sigma} \tag{4.5}$$

In the present simulation, we choose a relatively high current value as $I_{applied} = 6.0\ \mu A$ which results in a current density of $j_{applied} = 4775\ A/m^2$. Therefore, at the outlet the boundary conditions are

$$\frac{\partial \phi}{\partial x} = -\frac{j_{applied}}{\sigma}; \quad c_{TE} = 0; \quad c_{LE} = c_{LE}^0; \quad c_{CI} = c_{LE}^0 \tag{4.6}$$

Initial conditions are important in the simulation of ITP. Typically they should be relatively smooth (not too steep), otherwise it will bring difficulties to solve the equations. To smoothly initialize the concentrations of electrolytes, a type of exponential function is adopted

$$c_i = \frac{c_i^0}{1.0 + e^{\lambda x}} \tag{4.7}$$

where $i =$ TE or LE, c_i^0 is the total concentration of the ith species. λ is a parameter used to control the initial width of the TE-LE interface.

The counter-ionized species concentration c_{CI} is initialized based on c_{TE} and c_{LE} by using the electroneutrality approximation. A set of initial profiles of c_{TE}, c_{LE} and c_{CI} is shown in Figure 4.2.

In order to investigate the performance of the present WENO solver, we compare our WENO solver to different schemes provided by the latest SPRESSO solver [53] (an open source, nonlinear electrophoresis solver developed by the Santiago group at Stanford University) including the second-order central difference, the sixth-order compact, the first-order upwind, and the second-order SLIP (Symmetric Limited Positive) [92, 93] schemes on the same number of 200 uniform grid points.

Figure 4.3 (a) and (b) show the ionic concentration profiles of c_{TE} and c_{LE} solved by the second-order central difference and the sixth-order compact schemes on a mesh of 200 uniform grid points under a current density of $j_{applied} = 4775\ A/m^2$,

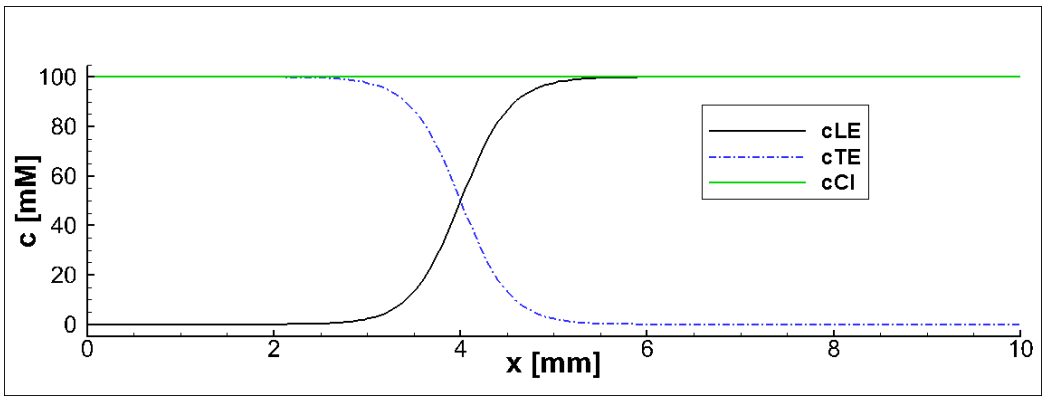

Fig. 4.2. Initialization of ionic concentrations ($t = 0s$).

respectively. It can be seen that only after a short time of $t = 1.4s$ significant numerical oscillations are observed due to the "self-sharpening effect" in ITP. The second-order central difference scheme or even the higher-order compact scheme fail to solve the problem on the given uniform grid though the sixth-order compact scheme gives relatively smaller oscillations compared to the second-order central scheme at the time of $t = 1.4s$.

In contrast to the second-order central difference and the sixth-order compact schemes, the first-order upwind, the second-order SLIP and the fifth-order WENO schemes can eliminate the oscillations and give smooth solutions using the same number of 200 uniform grid points. Figure 4.4 (a), (b), and (c) show the ionic concentration profiles of c_{TE} and c_{LE} solved by the above mentioned three schemes after $t = 10.0s$ under the current density of $j_{applied} = 4775\ A/m^2$, respectively. No undershoots nor overshoots occur at the TE-LE interface in the solutions. However, when taking a close look at the interface as shown in Figure 4.4 (d), the WENO scheme can capture a narrower width compared to the upwind and the SLIP schemes. This may be explained by the fact that for the upwind scheme due to its low-accurate and dissipative nature, though it allows a smooth solution it introduces much numerical diffusion and thus causes an overly diffused interface. The SLIP scheme offers a better solution because of its higher-order accuracy (second-order) compared to the upwind

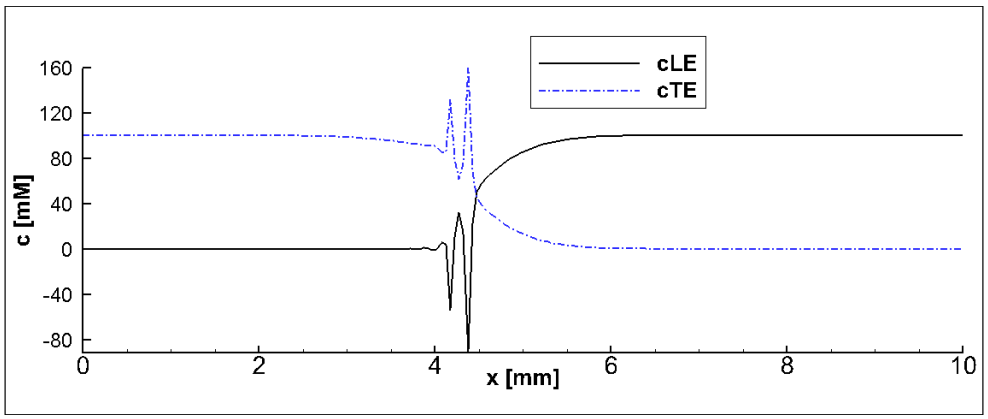

(a) Ionic concentrations solved by the second-order central difference scheme built in the SPRESSO solver [53].

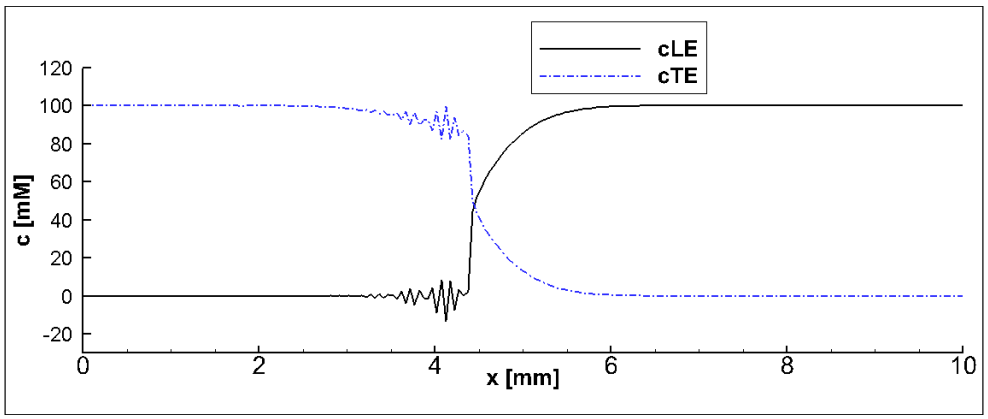

(b) Ionic concentrations solved by the sixth-order compact scheme built in the SPRESSO solver [53].

Fig. 4.3. Ionic concentrations solved by second-order central difference and sixth-order compact schemes on 200 uniform grid points after $t = 1.4s$ under a current density of $j_{applied} = 4775\ A/m^2$.

scheme. For the fifth-order WENO scheme, with the adaptive stencils for higher order approximation it reduces the numerical diffusion, i.e. captures the narrowest TE-LE interface among the three schemes given in Figure 4.4, and significantly improves the accuracy of the solution. In conclusion, we clearly see that the fifth-order WENO scheme can give a smooth solution with reduced numerical diffusion and thus it can be considered as a good option for simulating ITP problems.

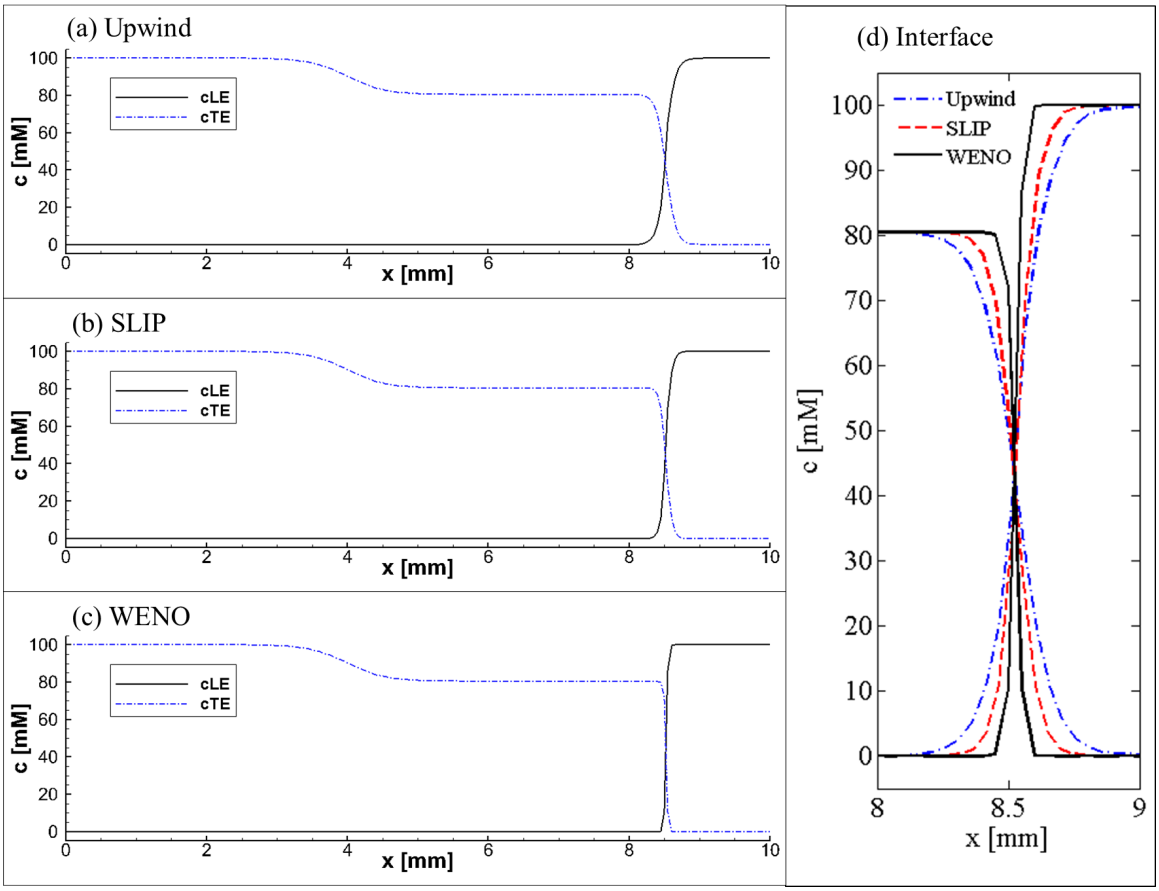

Fig. 4.4. Ionic concentrations solved by different schemes on 200 uniform grid points after $t = 10.0s$ under a current density of $j_{applied} = 4775\ A/m^2$. (a) Ionic concentrations solved by the first-order upwind. (b) Ionic concentrations solved by the second-order SLIP scheme. (c) Ionic concentrations solved by the fifth-order WENO scheme. (d) Comparison of the ionic concentrations solved by different schemes near the TE-LE interface.

Since there is an analytic solution available in the literature [38] for the ideal ITP case illustrated in Figure 4.1, we use this case to further test and validate the WENO solver. The following scales are introduced to obtain the non-dimensional governing equations: $[x] = H$, $[u] = U_{ITP}$, $[t] = H/U_{ITP}, [\phi] = \phi_0 = RT/F, [c_i] = c_{LE}^{\infty}, [E] = E_0 = \phi_0/H$. Here, H is the channel width, U_{ITP} is the isotachophoretic velocity. ϕ_0 is the characteristic electric potential. c_{LE}^{∞} is the bulk LE concentration.

By using the above scales as well as the electroneutrality approximation, the non-dimensional Nernst-Planck and charge conservation equations are obtained as

$$\frac{\partial c_i^*}{\partial t^*} + \frac{\partial}{\partial x^*}[(u^* - z_i \frac{D_i}{D_{CI}} \frac{1}{Pe} \nabla \phi^*) c_i^*] - \frac{D_i}{D_{CI}} \frac{1}{Pe} \frac{\partial^2 c_i^*}{\partial x^{*2}} = 0 \qquad \text{for i = TE, LE} \tag{4.8a}$$

$$\left(c_{LE}^* + \frac{D_{TE} + D_{CI}}{D_{LE} + D_{CI}} c_{TE}^* \right) \frac{\partial^2 \phi^*}{\partial x^{*2}} + \frac{\partial}{\partial x^*} \left(c_{LE}^* + \frac{D_{TE} + D_{CI}}{D_{LE} + D_{CI}} c_{TE}^* \right) \frac{\partial \phi^*}{\partial x^*} \tag{4.8b}$$

$$= -\frac{\partial^2}{\partial x^{*2}} \left(\frac{z_{LE} D_{LE} + z_{CI} D_{CI}}{D_{LE} + D_{CI}} c_{LE}^* + \frac{z_{TE} D_{TE} + z_{CI} D_{CI}}{D_{LE} + D_{CI}} c_{TE}^* \right)$$

where the non-dimensional parameter Peclet number is defined as

$$Pe \equiv \frac{U_{ITP} H}{D_{CI}} \tag{4.9}$$

In the absence of counterflow, the LE-TE interface moves at a constant isotachophoretic velocity

$$U_{ITP} = \mu_{LE} E_{LE} = \mu_{TE} E_{TE} \tag{4.10}$$

where the local electric field strengths in the LE or TE zones are denoted by E_i which can be expressed as

$$E_i = \frac{E_a / \mu_i}{l_{LE}/\mu_{LE} + l_{TE}/\mu_{TE}} \tag{4.11}$$

where, $l_{LE} = L_{LE}/L$ and $l_{TE} = L_{TE}/L$. $E_a = \Delta\phi/L$ is the average electric field due to the voltage drop $\Delta\phi$ along the channel. In the ideal ITP case, the LE-TE interface is assumed to be located in the middle of the channel, i.e. $l_{LE} = l_{TE} = 0.5$.

Since at the far-field the diffusive flux in the charge conservation equation is negligible, when evaluating Equation (4.8b) at the both sides of the transition zone that are sufficiently far away from the transition zone and using Equation (4.10), a relation between the TE and LE concentrations far away from the interfaces can be obtained as [94]

$$\frac{c_{TE}^\infty}{c_{LE}^\infty} = \frac{\mu_{LE} + \mu_{CI}}{\mu_{TE} + \mu_{CI}} \frac{\mu_{TE}}{\mu_{LE}} \tag{4.12}$$

The boundary conditions imposed at the inlet are

$$c_{TE}^* = \frac{\mu_{LE} + \mu_{CI}}{\mu_{TE} + \mu_{CI}} \frac{\mu_{TE}}{\mu_{LE}}; \quad c_{LE}^* = 0; \quad \phi^* = -\frac{E_{TE} H}{\phi_0} x^*(0) \tag{4.13}$$

At the outlet we set

$$c_{TE}^{*} = 0; \quad c_{LE}^{*} = 1.0; \quad \phi^{*} = -\frac{E_{LE}H}{\phi_0}x^{*}(L) \tag{4.14}$$

where, E_{TE} and E_{LE} are evaluated according to Equation (4.11). Notice the above described boundary conditions are all in non-dimensional form.

According to [38], the analytical solution for the TE concentration in a co-moving frame of reference under no bulk fluid flow can be expressed as

$$c_{TE}(x) = c_{TE}^{\infty}\ \mathbf{F}\left[1, \frac{E_{TE}}{\Delta E}; 1 + \frac{E_{TE}}{\Delta E}; -\frac{\mu_{LE} + \mu_{CI}}{\mu_{TE} + \mu_{CI}} e^{\frac{\Delta E}{\phi_0}x}\right] \tag{4.15}$$

where, $\mathbf{F}(a, b; c; z)$ is the hypergeometric function [95], $\Delta E = E_{TE} - E_{LE}$.

The electric field is

$$E(x) = E_{TE}\frac{c_{TE}^{\infty}}{c_{TE}(x)}\left[1 + \frac{\mu_{LE} + \mu_{CI}}{\mu_{TE} + \mu_{CI}} e^{\frac{\Delta E}{\phi_0}}\right]^{-1} \tag{4.16}$$

and at the steady state the LE concentration can be obtained via the relation

$$c_{LE}(x) = c_{TE} e^{\frac{\Delta E}{\phi_0}x} \tag{4.17}$$

Table 4.2
Parameters used in simulations of one-dimensional ideal ITP validation case.

Symbol	Description	Value
H	Width of the channel	$1.0 \times 10^{-5}[m]$
L	Length of the channel	$8.0 \times 10^{-5}[m]$
c_{LE}^{∞}	LE ion total concentration - LE zone	$1.0[mM]$
D_{LE}	Diffusivity of LE ion - LE zone	$7.0 \times 10^{-10}[m^2 \cdot s]$
k	D_{LE}/D_{TE}	2
ϕ_0	electric potential scale	$25.9[mV]$
E_a	Average electric field	$10^5[V \cdot m^{-1}]$

Assume $D_{CI} = D_{LE}$ and define $k = D_{LE}/D_{TE} = \mu_{LE}/\mu_{TE}$. The parameters used in the simulation are listed in Table 4.2.

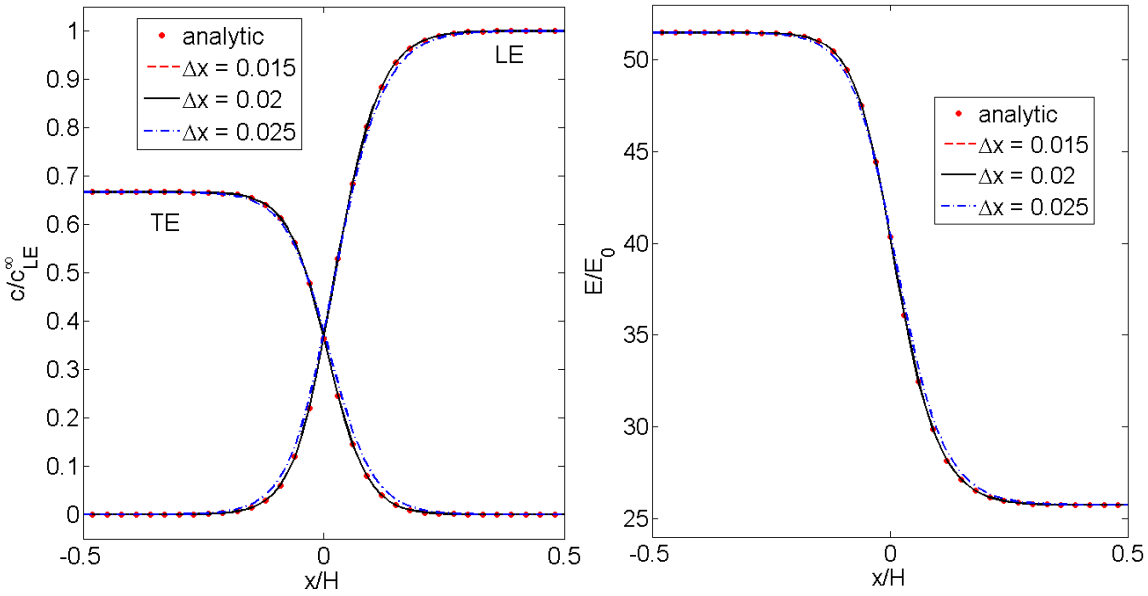

(a) Ionic concentrations (b) Electric field

Fig. 4.5. Numerical results solved by Weno scheme versus the analytic solution given in [38] on different uniform grid meshes.

For the given domain, three different grid sizes, i.e. 320, 400, 540 uniform grid points corresponding to $\Delta x^* = 0.025, 0.02, 0.015$ are used in the simulations. As shown in Figure 4.5, the numerical results agree well with the analytical solution on a grid of spacing $\Delta x^* = 0.02$. Thus the present WENO solver successfully resolves the sharp interface which is only a few micrometers wide for the given ITP problem.

4.1.2 Two-dimensional Sample Dispersion in ITP with Poiseuille Counterflow

As described at the beginning of this chapter, in ITP sample ions with an electrophoretic mobility between the leading (LE) and trailing (TE) ion mobilities are sandwiched between the two electrolytes and thus form a transient zone. In the past decades, researchers introduced a pressure-driven counterflow or electroosmotic counterflow to balance the sample migration in ITP experiments as such counterflow-balanced ITP can be widely used in the applications of sample preconcentration for

improving the sensitivity of capillary electrophoresis [96] or to control the elution of analytes [97].

In this subsection, we use the present WENO solver to numerically study sample dispersion in which electromigration in ITP is balanced by a Poiseuille counterflow. We set up the simulation case by following [60]. Two-dimensional simulations are conducted for the case illustrated in Figure 4.6. Under the action of an external electric field, a single sample zone is formed between the LE and TE electrolytes. The sample ions migrate from left to right at velocity U^{ITP}. A pressure driven flow is introduced in the opposite direction to exactly balance the electromigration and thus make the sample zone stationary.

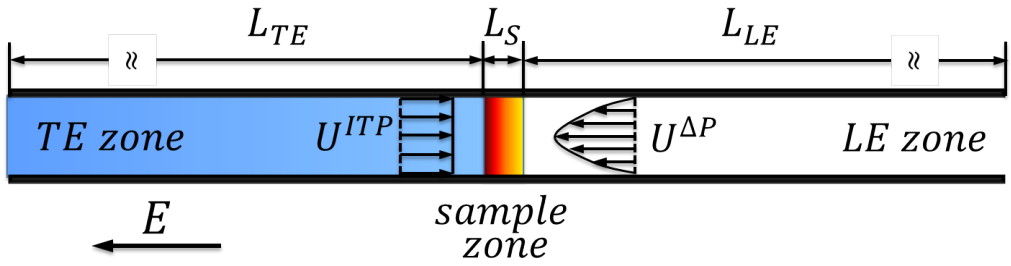

Fig. 4.6. Schematic showing the case of two-dimensional sample dispersion in ITP with Poiseuille counterflow.

Using the same scales as given in the previous subsection, i.e. $[x, y] = H$, $[u, v] = U_{ITP}$, $[t] = H/U_{ITP}, [\phi] = \phi_0 = RT/F, [c_i] = c_{LE}^{\infty}, [E] = E_0 = \phi_0/H$, and also the electroneutrality approximation, the non-dimensional coupled Nernst-Planck and charge conservation equations can be written as

$$\frac{\partial c_i^*}{\partial t^*} + \nabla \cdot [(\mathbf{u}^* - z_i \frac{D_i}{D_S} \frac{1}{Pe} \nabla \phi^*) c_i^*] - \frac{D_i}{D_S} \frac{1}{Pe} \nabla^2 c_i^* = 0 \qquad \text{for i = TE, LE, S} \quad (4.18a)$$

$$\nabla \cdot \left[\left(c_{LE}^* + \frac{D_S + D_{CI}}{D_{LE} + D_{CI}} c_S^* + \frac{D_{TE} + D_S}{D_{LE} + D_{CI}} c_{TE}^* \right) \nabla \phi^* \right] \quad (4.18b)$$

$$= -\nabla^2 \left[\frac{z_{LE} D_{LE} + z_{CI} D_{CI}}{D_{LE} + D_{CI}} c_{LE}^* + \frac{z_S D_S + z_{CI} D_{CI}}{D_{LE} + D_{CI}} c_S^* + \frac{z_{TE} D_{TE} + z_{CI} D_{CI}}{D_{LE} + D_{CI}} c_{TE}^* \right]$$

where the non-dimensional parameter Peclet number is defined by

$$Pe \equiv \frac{U_{ITP} H}{D_S} \quad (4.19)$$

As what has been assumed in the previous subsection, the local electric field strengths in the LE, sample or TE zones are denoted by E_i with $i = LE, S, TE$ respectively, and it can be expressed as

$$E_i = \frac{E_a/\mu_i}{\sum_k (l_k/\mu_k)} \tag{4.20}$$

where, $l_k = L_k/L$. L_k (with k = LE, S or TE) is the portion of the channel filled by the respective electrolyte and L is the total length of the channel. $E_a = \Delta\phi/L$ is the average electric field due to the voltage drop $\Delta\phi$ along the channel. Since in ITP applications, the channel is long compared to the section occupied by sample, then l_S is assumed to be negligible in Equation (4.20). For the sake of convenience, the sample zone is located in the middle of the channel, thus $l_{LE} = l_{TE} \approx 0.5$.

Similar to the relation 4.11, the upper bound of the initial sample concentration in the plateau mode, i.e. the sample concentration forms a distinct zone with constant concentration, may be determined by

$$\frac{c_S^0}{c_{LE}^\infty} = \frac{\mu_{LE} + \mu_{CI}}{\mu_S + \mu_{CI}} \frac{\mu_S}{\mu_{LE}} \tag{4.21}$$

By following the condition given in [60] , to include the effect of the Poiseuille counterflow, instead of solving the Navier-Stokes equations a parabolic velocity profile with an average speed equal and opposite to ITP migration is imposed throughout the computational domain by

$$u(y) = -6U_{ITP}\frac{y}{H}(1 - \frac{y}{H}) \tag{4.22}$$

In non-dimensional form it becomes

$$u^*(y^*) = -6y^*(1 - y^*) \tag{4.23}$$

where, y^* is from 0 to 1.0.

The boundary conditions imposed in the simulation are summarized as follows and they are all in non-dimensional form.

At the inlet, the non-dimensional boundary conditions are

$$c_{TE}^* = \frac{\mu_{LE} + \mu_{CI}}{\mu_{TE} + \mu_{CI}} \frac{\mu_{TE}}{\mu_{LE}}; \quad c_S^* = 0; \quad c_{LE}^* = 0; \quad \phi^* = -\frac{E_{TE}H}{\phi_0} x^*(0) \tag{4.24}$$

At the outlet, we impose

$$c^*_{TE} = 0; \quad c^*_S = 0; \quad c^*_{LE} = 1.0; \quad \phi^* = -\frac{E_{LE}H}{\phi_0}x^*(L) \tag{4.25}$$

where, E_{TE} and E_{LE} are evaluated according to Equation (4.20).

The channel walls are impermeable for all ions, thus at the walls

$$\mathbf{n} \cdot \nabla c^*_i = 0; \quad \mathbf{n} \cdot \nabla \phi^* = 0 \tag{4.26}$$

where, $\mathbf{n}$ denotes the wall-normal direction.

Again, assume $D_{CI} = D_{LE}$ and define $k_1 = D_{LE}/D_{TE} = \mu_{LE}/\mu_{TE}$ and $k_2 = D_{LE}/D_S = \mu_{LE}/\mu_S$. Other basic simulation parameters are listed in Table 4.3. For all the simulations presented afterwards in this subsection, the computational domain is discretized on a uniform grid with a spacing of $\Delta x^* = \Delta y^* = 0.02$.

Table 4.3
Simulation parameters used in case of two-dimensional sample dispersion in ITP with Poiseuille counterflow.

Symbol	Description	Value
c^∞_{LE}	LE ion total concentration - LE zone	$1.0[mM]$
D_{LE}	Diffusivity of LE ion - LE zone	$7.0 \times 10^{-10}[m^2 \cdot s]$
z_{LE}	valence of LE	-1
z_S	valence of LE	-1
z_{TE}	valence of TE	-1
z_{CI}	valence of CI	$+1$
ϕ_0	electric potential scale	$25.9[mV]$
E_a	Average electric field	$10^5[V \cdot m^{-1}]$

In order to obtain comparable results for the distortion of the sample zone due to applied Poisuille flow, by following [60] the area-averaged amount of sample is fixed and defined as

$$C_s = \int_{-\infty}^{\infty} dx \bar{C}_s(x) \tag{4.27}$$

where,

$$\bar{C}_s(x) = \frac{1}{H}\int_0^H dy C_i(x,y) \tag{4.28}$$

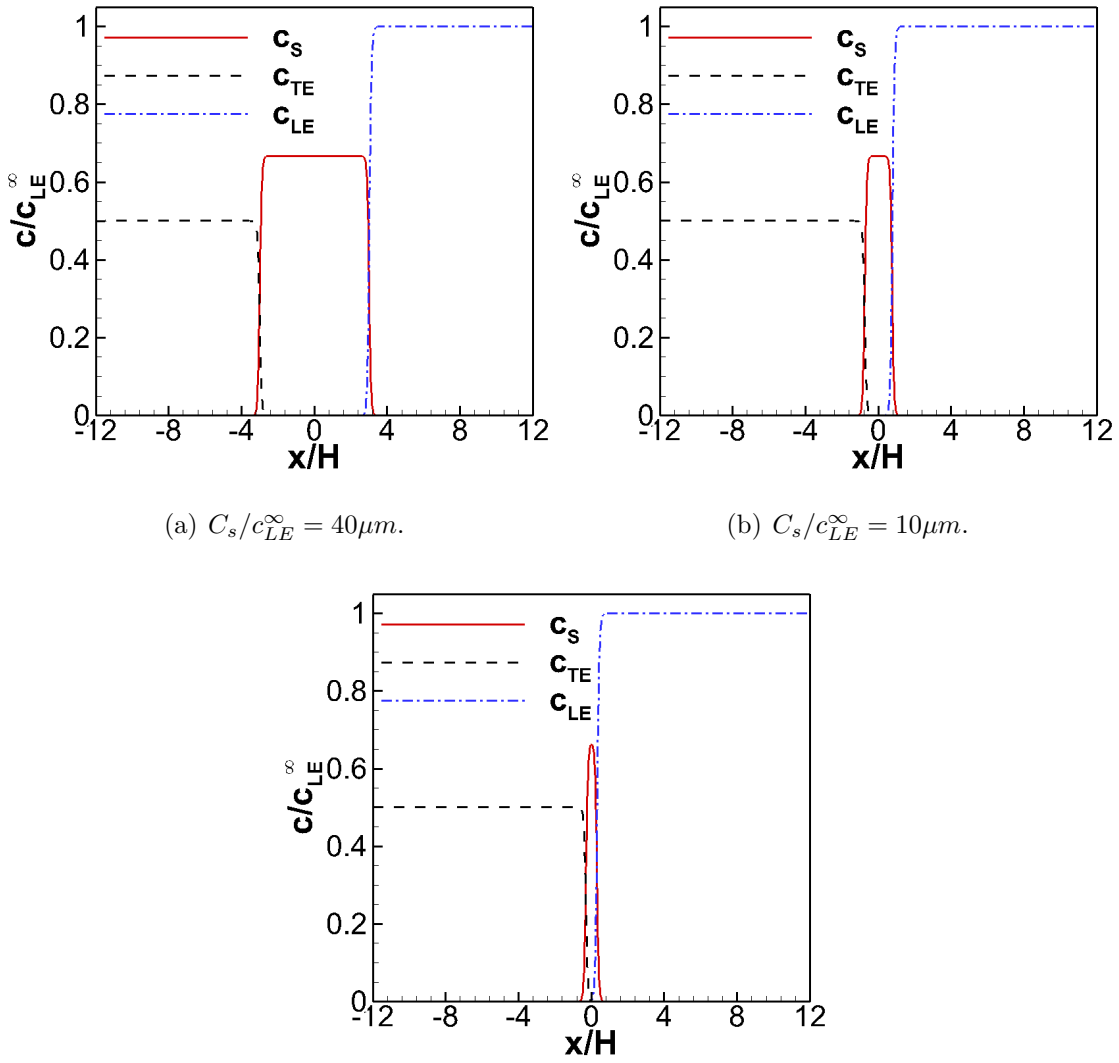

(a) $C_s/c_{LE}^{\infty} = 40\mu m$.

(b) $C_s/c_{LE}^{\infty} = 10\mu m$.

(c) $C_s/c_{LE}^{\infty} = 4\mu m$.

Fig. 4.7. Sample, TE, and LE concentration profiles solved by the present WENO solver at steady state in a moving frame of reference at the constant speed U_{ITP} for three different sample amounts. Here, $H = 10\mu m$ and $k_1 = 3, k_2 = 2$.

The initial condition for the current case is obtained from the solution of the corresponding ITP case without counterflow. In other words, before imposing the

parabolic velocity profile and starting to simulate sample dispersion in ITP with Poiseuille counterflow, a steady-state for the TE, sample and LE concentration profiles without counterflow is achieved first for $l_{LE} = l_{TE} \approx 0.5$ in a co-moving frame of reference at the constant speed U^{ITP}. Figure 4.7 (a)-(c) show such cases for $H = 10\mu m$ and $k_1 = 3,\ k_2 = 2$ with sample amounts from $C_s/c_{LE}^{\infty} = 40\mu m$, $10\mu m$ and $4\mu m$. It can be seen that when $C_s/c_{LE}^{\infty} = 40\mu m$, the sample concentration clearly develops a plateau. As the sample amount decreases, a Gaussian peak is observed. It validates that the present WENO solver can resolve the transient zones for plateau- and peak-mode steady-state ideal ITP.

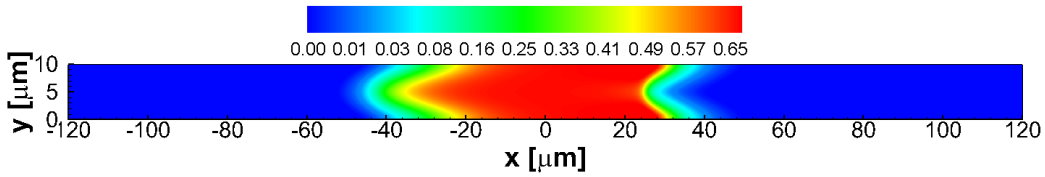

(a) Sample concentration contour for $H = 10\mu m$ ($Pe = 39$).

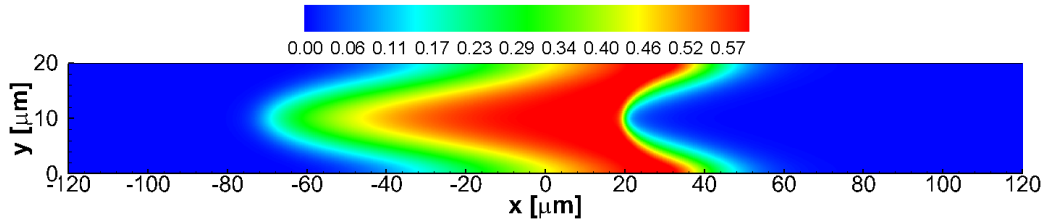

(b) Sample concentration contour for $H = 20\mu m$ ($Pe = 77$).

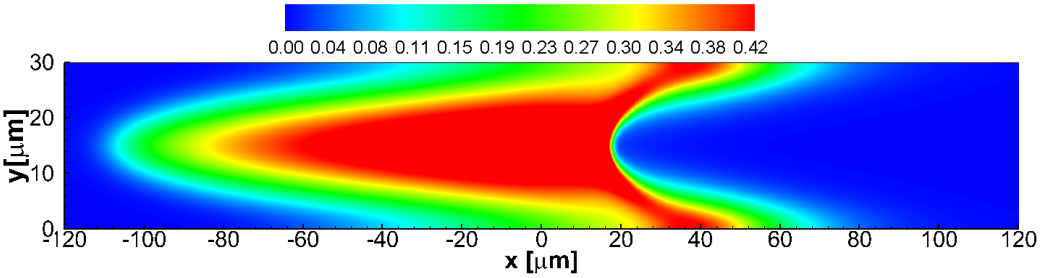

(c) Sample concentration contour for $H = 30\mu m$ ($Pe = 116$).

Fig. 4.8. Sample concentration contours solved by the present WENO solver for three different channel heights with a sample amount of $C_s/c_{LE}^{\infty} = 40\mu m$. Here, $k_1 = 3$ and $k_2 = 2$.

Once the steady state has been reached, the parabolic velocity profile is imposed throughout the domain to simulate sample dispersion in ITP with Poiseuille counter-flow. First, we study the effect of channel height on sample dispersion. Figure 4.8 (a)-(c) show the sample concentration contours for three different channel heights, i.e. $H = 10\mu m, 20\mu m, 30\mu m$, with a sample amount of $C_s/c_{LE}^{\infty} = 40\mu m$. Here, $k_1 = 3$ and $k_2 = 2$. The corresponding area-averaged sample concentration profiles are shown in Figure 4.9.

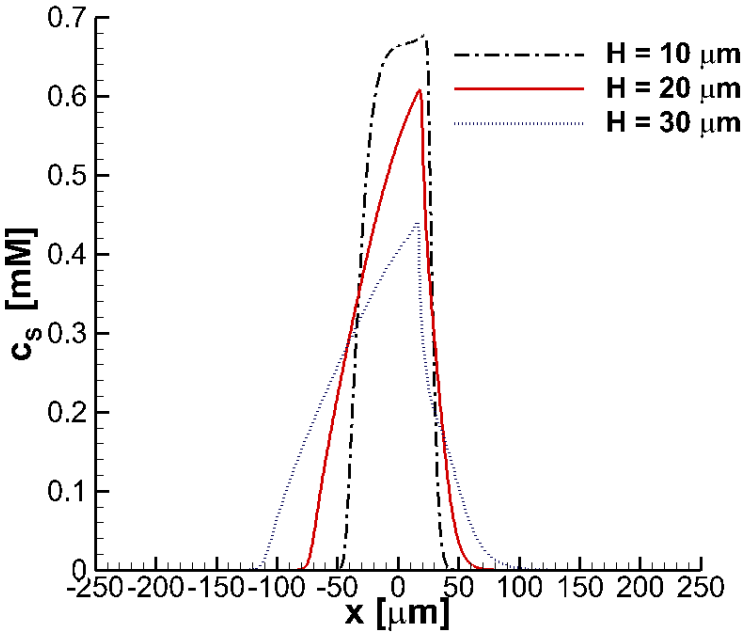

Fig. 4.9. Area-averaged sample concentration profiles solved by the present WENO solver for three different channel heights with a sample amount of $C_s/c_{LE}^{\infty} = 40\mu m$. Here, $k_1 = 3$ and $k_2 = 2$.

From the sample concentration contours it can be seen that as the channel width increases, a stronger sample dispersion is observed. This may be explained by the fact that the wider channel results in a larger Peclet number and thus leads to a larger dispersion. From the area-averaged sample concentration profiles it is apparent that the sample zone changes from a plateau mode to a peak mode with the increase of the channel width. In addition, as the the channel width become wider, the maximum value of the area-averaged sample concentration decreases due to strong dispersion.

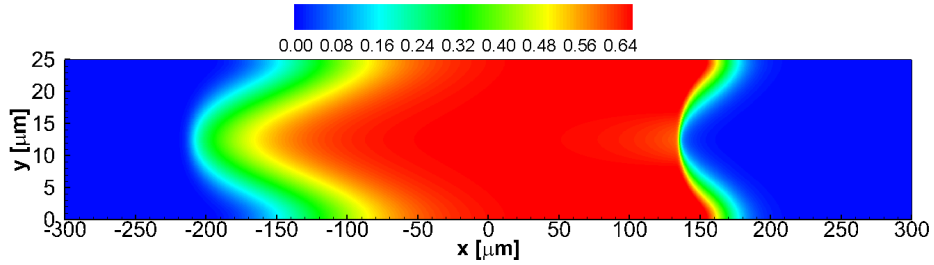

(a) $C_s/c_{LE}^{\infty} = 200\mu m$.

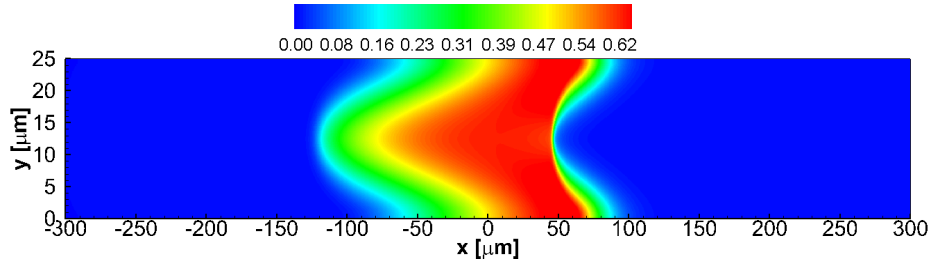

(b) $C_s/c_{LE}^{\infty} = 80\mu m$.

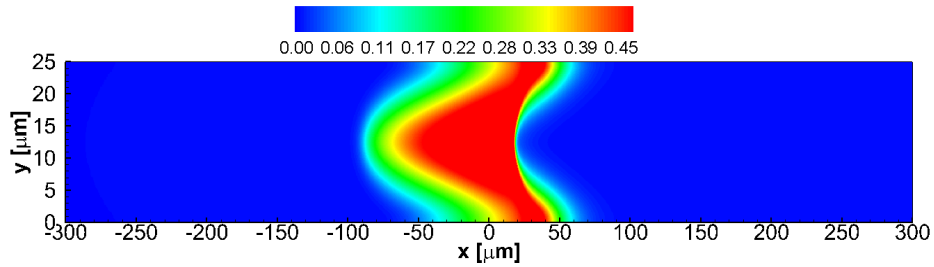

(c) $C_s/c_{LE}^{\infty} = 40\mu m$.

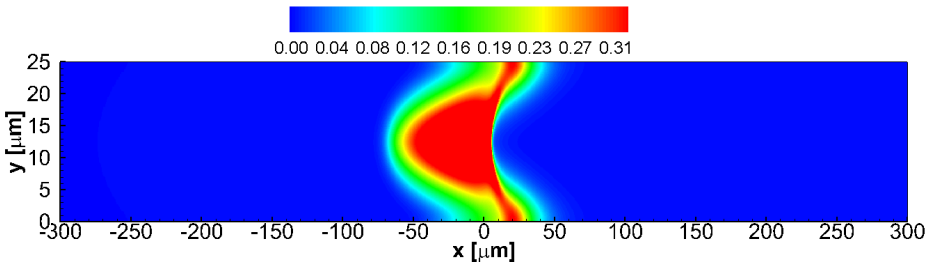

(d) $C_s/c_{LE}^{\infty} = 20\mu m$.

Fig. 4.10. Sample concentration contours solved by the present Weno solver for four different total amounts of sample present in the channel. Here, $H = 25\mu m$, $k_1 = 3$, and $k_2 = 2$.

Next, we study the effect of the sample amount on sample dispersion in ITP with Poiseuille counterflow. As what has been done in [60], four different values of the total amount of sample present in the channel are considered which are varied as $C_s/c_{LE}^{\infty} = 200, 80, 40, 20\ \mu m$. The channel height is fixed as $H = 25\mu m$ and $k_1 = 3$, $k_2 = 2$.

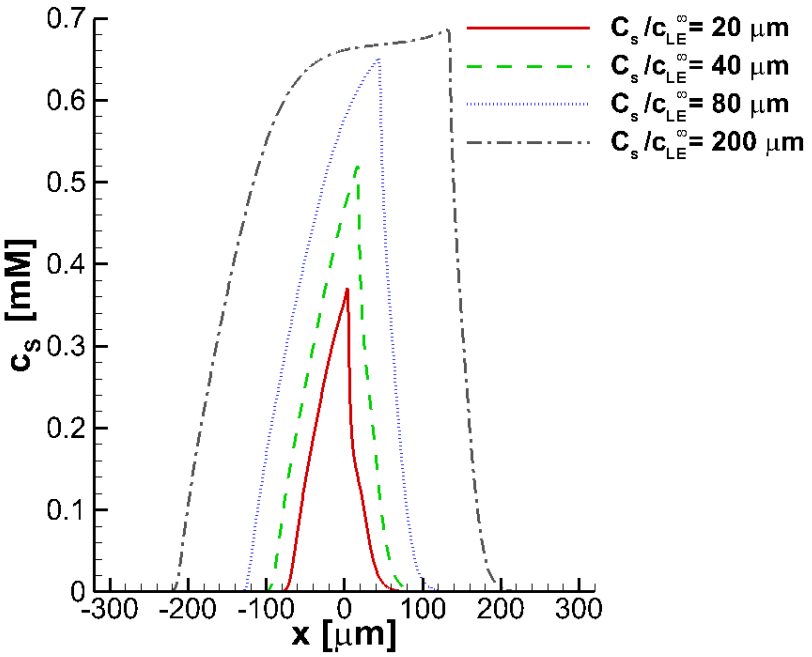

Fig. 4.11. Area-averaged sample concentration profiles solved by the present WENO solver for four different total amounts of sample present in the channel. Here, $H = 25\mu m$, $k_1 = 3$ and $k_2 = 2$.

Figure 4.10 (a)-(d) show the sample concentration contours solved by the present WENO solver for $H = 25\mu m$ with different total amounts of sample present in the channel. The corresponding area-averaged sample concentration profiles are shown in Figure 4.11. For the largest amount of sample present in the channel, i.e. $C_s/c_{LE}^{\infty} = 200\mu m$, the sample zone may be considered in a plateau mode. However, as there is a strong additional dispersion due to convection from the Poiseuille counterflow a peak can still be observed from the area-averaged sample concentration profile. In [60], such phenomenon is termed as "dispersed plateau mode". As the amount of

sample present in the channel decreases the sample focuses in the central region of the channel and a more pronounced peak is observed from the area-averaged sample concentration profiles.

Finally we study the effect of the ratios of ionic mobilities on sample dispersion in ITP with Poiseuille counterflow. Here we fix the ratio of the LE to TE mobilities and set $k_1 = \mu_{LE}/\mu_{TE} = D_{LE}/D_{TE} = 3$. The ratio of the LE to sample mobilities k_2 is varied as $k_2 = \mu_{LE}/\mu_S = D_{LE}/D_S = 1.1,\ 2.0$, and 2.7. Figure 4.12 shows the sample concentration contours for the three different ratios of the mobilities k_2 when the channel height is $H = 25\mu m$ and the sample amount is $C_s/c_{LE}^{\infty} = 40\mu m$. The corresponding area-averaged sample concentration profiles are given in Figure 4.13.

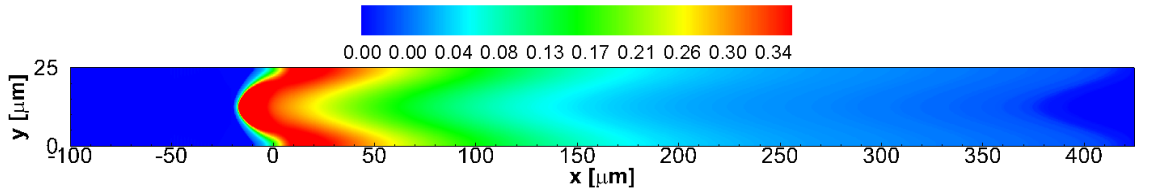

(a) $k_2 = \mu_{LE}/\mu_S = D_{LE}/D_S = 1.1$.

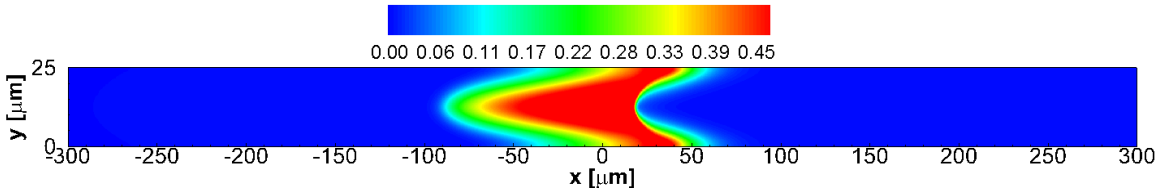

(b) $k_2 = \mu_{LE}/\mu_S = D_{LE}/D_S = 2.0$.

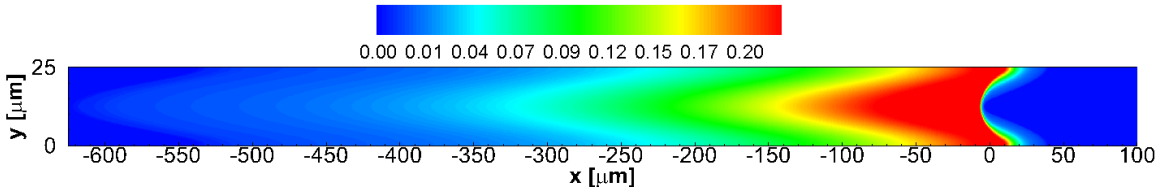

(c) $k_2 = \mu_{LE}/\mu_S = D_{LE}/D_S = 2.7$.

Fig. 4.12. Sample concentration contours solved by the Weno solver for different ratios of ionic mobilities k_2 when the channel height is $H = 25\mu m$, $k_1 = \mu_{LE}/\mu_{TE} = D_{LE}/D_{TE} = 3$, and the sample amount is $C_s/c_{LE}^{\infty} = 40\mu m$.

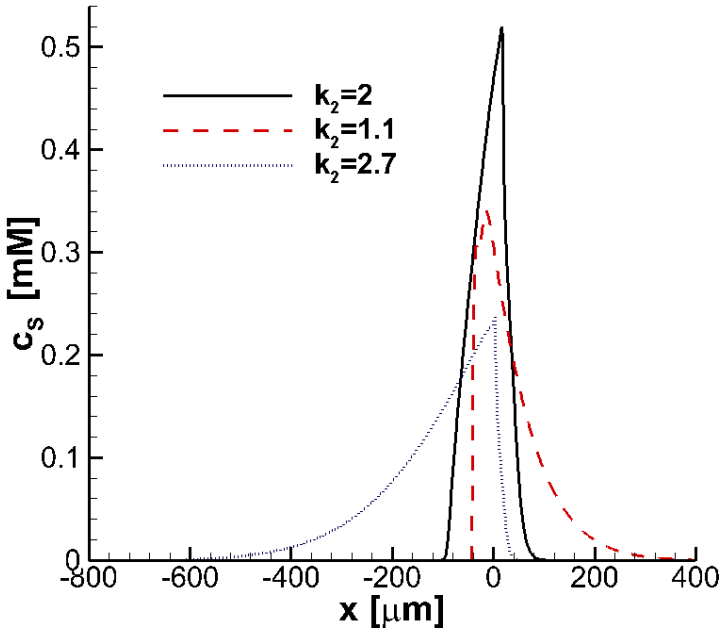

Fig. 4.13. Area-averaged sample concentration profiles solved by the fifth-order Weno solver for different ratios of ionic mobilities k_2 when the channel height is $H = 25\mu m$, $k_1 = \mu_{LE}/\mu_{TE} = D_{LE}/D_{TE} = 3$, and the sample amount is $C_s/c^{\infty}_{LE} = 40\mu m$.

From Figures 4.12 and 4.13 it can be seen that when the sample mobility is close to either the LE mobility ($k_2 = 1.1$) or the TE mobility ($k_2 = 2.7$), a very wide sample transition zone is formed and the long dispersed tails are towards the electrolyte zone with a similar mobility. For example, for $k_2 = 1.1$ meaning the sample mobility is close to the LE mobility, the transition zone is dispersed in the LE (right) zone, see Figure 4.12(a). While for $k_2 = 2.7$ in which the sample mobility is similar to the TE mobility, the long tail is towards the TE (left) zone, see Figure 4.12(c). When the sample is of an evidently different mobility than the LE or TE mobilities, for example, $k_2 = 2$, an electromigrative sharpening is present and a much narrower transition zone is formed, see Figure 4.12(b) and Figure 4.13. In conclusion, in order to have an effective preconcentration (with less dispersion), the net mobilities of TE, LE and sample should be distinct. On the other hand, ITP cannot be used to separate

and preconcentrate samples if the mobilities of the TE, LE, and sample electrolytes are very close to each other.

4.1.3 Summary

In this section 4.1, we first test the performance of the present WENO solver by simulating the simplest ITP case, i.e. one-dimensional ideal ITP without sample analytes. For the case where a relatively high current density (about $5000 A/m^2$) is applied, simulation results obtained by the present WENO solver are compared to those solved by different numerical schemes including the second-order central difference, the sixth-order compact, the first-order upwind, and the second-order SLIP (Symmetric Limited Positive) schemes provided by an open source solver SPRESSO [53]. On a given mesh of the same grid size, it is found that the WENO solver not only gives a smooth solution (compared to the oscillatory solution given by the second-order central difference and the sixth-order compact schemes), but it also captures a much narrower species interface and thus offers a more accurate solution with reduced numerical diffusion (compared to the first-order upwind and the second-order SLIP schemes). For the same 1D ideal ITP case the present WENO solver is also validated by comparing the obtained numerical result with the analytic solution available in the literature.

In the second part of the current section, the validated WENO solver is used to perform a series of two-dimensional simulations for sample dispersion in ITP with Poiseuille counterflow. Such counterflow-balanced ITP has a wide range of applications in sample preconcentration in microfluidic devices. The effect of different parameters on sample dispersion, including channel height, electrophoretic mobility ratio, and sample amount present in the channel are investigated. For the considered cases, all the ITP phenomena simulated by the WENO solver are consistent with those presented in the literature. It indicates that the present WENO solver can

successfully solve ITP problems and thus can be used as a good numerical tool to analyze and study ITP phenomena.

4.2 Simulation of EKI in a Two-dimensional Straight Microchannel

In order to understand the basic mechanism and behavior of EKI, numerical simulations of EKI in a two-dimensional straight microchannel were conducted in this section. Typically, EKI can occur with two basic types of initial states as shown in Figure 4.14, where **E** is electric field while σ_H (darker) and σ_L (brighter) denote high- and low-conductivity regions, respectively [98].

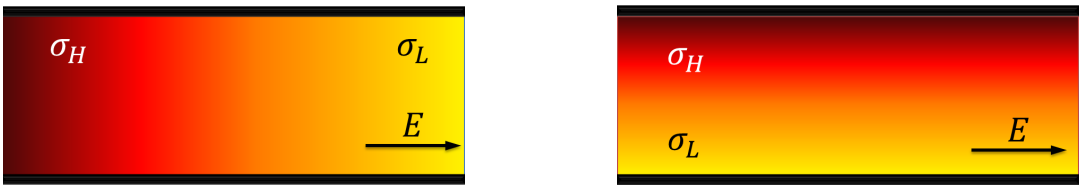

(a) Type I: coaxial gradient case. (b) Type II: orthogonal gradient case.

Fig. 4.14. Schematic of typical initial states for EKI.

For type I, the electric field is parallel to the conductivity gradient and thus this case can be named as coaxial gradient case. From Equation (2.18c), it can be seen that net charge density ρ_e has a non-trivial distribution even in an initial state like this. In microfluidic applications, flows in this type of initial state often occur in the stacking/separation phase [99]. For type II, the electric field is perpendicular to the conductivity gradient and this initial state can be called orthogonal gradient case. Net charge density in such initial state is simply zero according to Equation (2.18c). Compared to type I initial state, this type of initial state is relatively more unstable. Thus, in practice flows in type II initial state are frequently explored for micromixing applications [29].

In the following subsecitons 4.2.1 and 4.2.2, simulations of EKI for the coaxial gradient and the orthogonal gradient initial states are performed, respectively.

4.2.1 Coaxial Gradient Case

In this subsection, the type I initial state for EKI as shown in Figure 4.14(a) is considered. The conductivity gradient of a symmetric binary electrolyte solution in a two-dimensional straight microchannel is assumed along the horizontal wall direction. Different electrical potentials are imposed at the inlet and the outlet such that the applied electric field is colinear with the conductivity gradient. The velocity field is initially zero everywhere and the flow in such an electrokinetic microchannel is then driven by electrical body forces. In general, the velocity of the flow in the channel depends on the applied electric field, the electro-osmotic mobility (for a symmetric binary electrolyte solution, it is simply to be conductivity according to the mathematical model derived in Section 2.1), and both imposed and internally-generated pressure gradients. Although electrokinetic flows with heterogeneous electrolytes or zeta-potentials may generate internal pressure gradients [100], since here we are highly interested in the electrokinetic effects on fluid motion, we impose no external pressure differences, i.e. the pressure imposed at the inlet and the outlet is identical.

Proper boundary conditions described in Section 2.1.2, i.e. Equations (2.22a)-(2.22d), are imposed at the two horizontal walls. At the inlet (left side of the channel), the nondimensional boundary conditions can be written as

$$\mathbf{n} \cdot \nabla \mathbf{u} = 0 \tag{4.29a}$$

$$p = p_{ref} \tag{4.29b}$$

$$\sigma = \sigma_{inlet} \tag{4.29c}$$

$$\phi = \phi_{inlet} \tag{4.29d}$$

while at the outlet (right side of the channel), the imposed boundary conditions are

$$\mathbf{n} \cdot \nabla \mathbf{u} = 0 \tag{4.30a}$$

$$p = p_{ref} \tag{4.30b}$$

$$\mathbf{n} \cdot \nabla \sigma = 0 \tag{4.30c}$$

$$\phi = \phi_{outlet} \tag{4.30d}$$

where, $\mathbf{n}$ denotes the inlet/outlet normal direction, and p_{ref} is the reference pressure imposed at both the inlet and the outlet. σ_{inlet} is the conductivity value at the inlet, while ϕ_{inlet} and ϕ_{outlet} are the electric potentials imposed at the inlet and outlet respectively.

The 2D straight microchannel considered here is $50\mu m$ wide and $500\mu m$ long. Other parameters and fundamental scales are given in Table 4.4. Accordingly, the important nondimensional parameters in the simulation such as the Reynolds number and the electrical Rayleigh number etc. are calculated as $Re \approx 1.08$, $Ra_e \approx 541.4$ and $Rv \approx -17.9$. For convenience, a conductivity ratio is introduced and defined as $\gamma = \sigma_{inlet}/\sigma_{outlet}$. In all the simulations conducted in this subsection γ is chosen as 2.5 while σ_{inlet} is set to 1.0, and thus $\sigma_{outlet} = 0.4$.

Table 4.4
Parameters and fundamental scales used in 2D simulations of EKI for the colinear gradient case.

Symbol	Description	Value
w	Length scale (half width of the channel)	$2.5 \times 10^{-5}[m]$
μ	Absolute viscosity of fluid	$1.0 \times 10^{-3}[kg \cdot m^{-1}s^{-1}]$
ρ	Density of fluid	$1.0 \times 10^{3}[kg \cdot m^{-3}]$
ϵ	Permittivity	$6.93 \times 10^{-10}[C \cdot V^{-1}m^{-1}]$
D_{eff}	Effective diffusivity	$2.0 \times 10^{-9}[m^2s^{-1}]$
E_0	Reference electric field	$5.0 \times 10^{4}[V \cdot m^{-1}]$
ζ_0	Reference EDL zeta-potential	$-7.0 \times 10^{-2}[V]$

For the initial state, the electric field is assumed to be uniform. Thus, the electric potential field is initialized using a linear function

$$f(x) = c_1 x + c_2 \tag{4.31}$$

where, the coefficients c_1 and c_2 in the function are determined by the electric potentials imposed at the inlet/outlet and the locations of the inlet/outlet

$$c_1 = \frac{\phi_{inlet} - \phi_{outlet}}{x_{inlet} - x_{outlet}} \tag{4.32a}$$

$$c_2 = \phi_{inlet} - c_1 x_{inlet} \tag{4.32b}$$

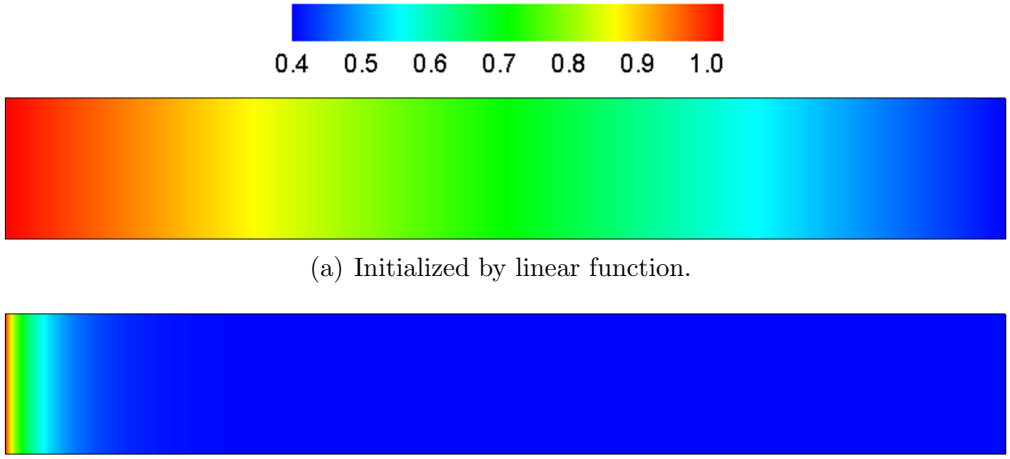

(a) Initialized by linear function.

(b) Initialized by exponential function.

Fig. 4.15. Initialization of conductivity fields in 2D simulations of EKI for the colinear gradient case.

To generate conductivity gradient for the initial state, two types of functions are used in order to study the effect of conductivity gradient on EKI respectively. Besides the linear function 4.31, the conductivity field is also initialized by an exponential function

$$f(x) = \frac{c_2}{c_1 + e^{-x}} \tag{4.33}$$

where, the coefficients c_1 and c_2 in the function can be determined by solving a 2×2 system of equations to fulfill the boundary conditions for conductivity at the inlet and the outlet

$$c_1 = \frac{\sigma_{inlet} e^{-x_{inlet}} - \sigma_{outlet} e^{-x_{outlet}}}{\sigma_{outlet} - \sigma_{inlet}} \tag{4.34a}$$

$$c_2 = \frac{\sigma_{inlet}\sigma_{outlet}\left(e^{-x_{inlet}} - e^{-x_{outlet}}\right)}{\sigma_{outlet} - \sigma_{inlet}} \tag{4.34b}$$

The conductivity fields initialized by the two different functions are visualized in Figure 4.15. It is clear that the conductivity gradient in the state initialized by the exponential function as shown in Figure 4.15(b) is higher than that in the state initialized by the linear function as shown in Figure 4.15(a), though the conductivity ratio γ is the same. From the simulation results that would be provided in this subsection later, it can be found that these two different initial conductivity fields will greatly affect EKI phenomena and conductivity gradient actually plays an important role in the mechanism of EKI.

In order to study the effects of conductivity gradients as well as electric fields on EKI, a series of simulations are performed, in which the strength of the applied electric field starts with $E = 1250$ V/cm, and then is increased to $E = 2500V/cm$ and finally to $E = 5000$ V/cm. For the same applied electric field strength, linear and exponential initialization strategies for conductivity field are used respectively and compared. The simulation results for $E = 1250$V/cm, $E = 2500$V/cm and $E = 5000$V/cm are provided in Figures 4.16, 4.17, and 4.18 respectively. In each figure, the plots in the left column are the conductivity fields evolved from the linear function initialized state, while the plots in the right column show the conductivity fields evolved from the exponential function initialized state.

Figure 4.16 shows the evolving conductivity field for $E = 1250$V/cm. In the snapshots given in the left column, the conductivity field evolves from the state initialized by the linear function. The electrokinetic flow in this condition is driven by the electrical body force from rest and smoothly moves towards the outlet. No instability is observed until the flow completely moves out of the channel and the entire domain is filled with high conductivity. As a contrast, though it is under the same applied electric field, the flow with a high conductivity gradient that is initialized by the exponential function becomes unstable, see the snapshots shown in the right column in Figure 4.16.

Similar phenomena are observed in Figure 4.17 for a higher electric field $E = 2500$ V/cm. The flow with lower conductivity gradient as shown in the left column still

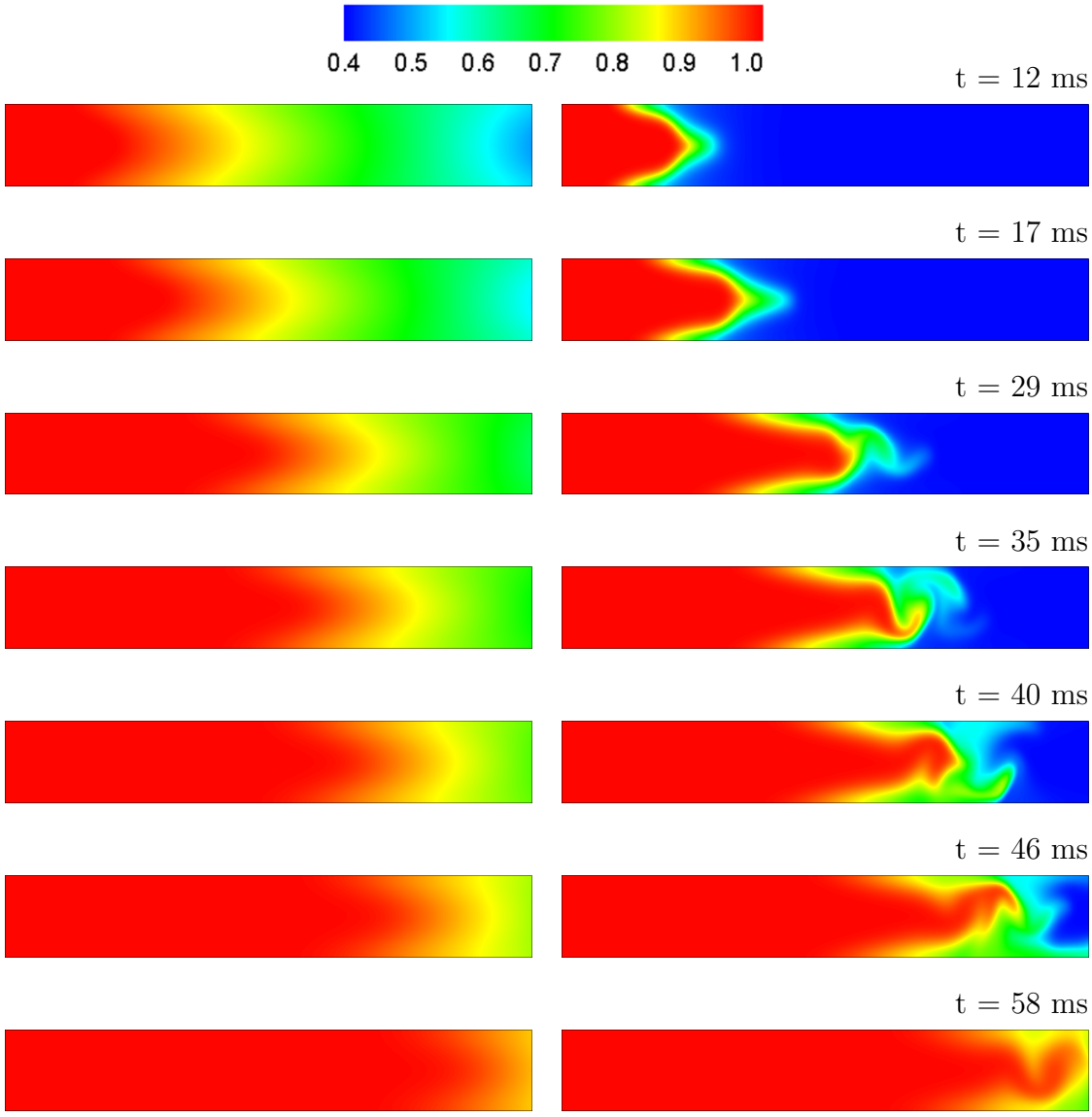

(a) Linear initialization strategy (b) Exponential initialization strategy

Fig. 4.16. Snapshots of the conductivity field evolved from different initial conductivity gradients under $E = 1250$ V/cm.

maintains stable until it completely moves through the channel. Again, in the right column the flow with higher conductivity gradient undergoes instability. However, since the strength of the applied electric field is stronger which will result in a larger electrical body force, the instability is observed more vigorous compared to the pre-

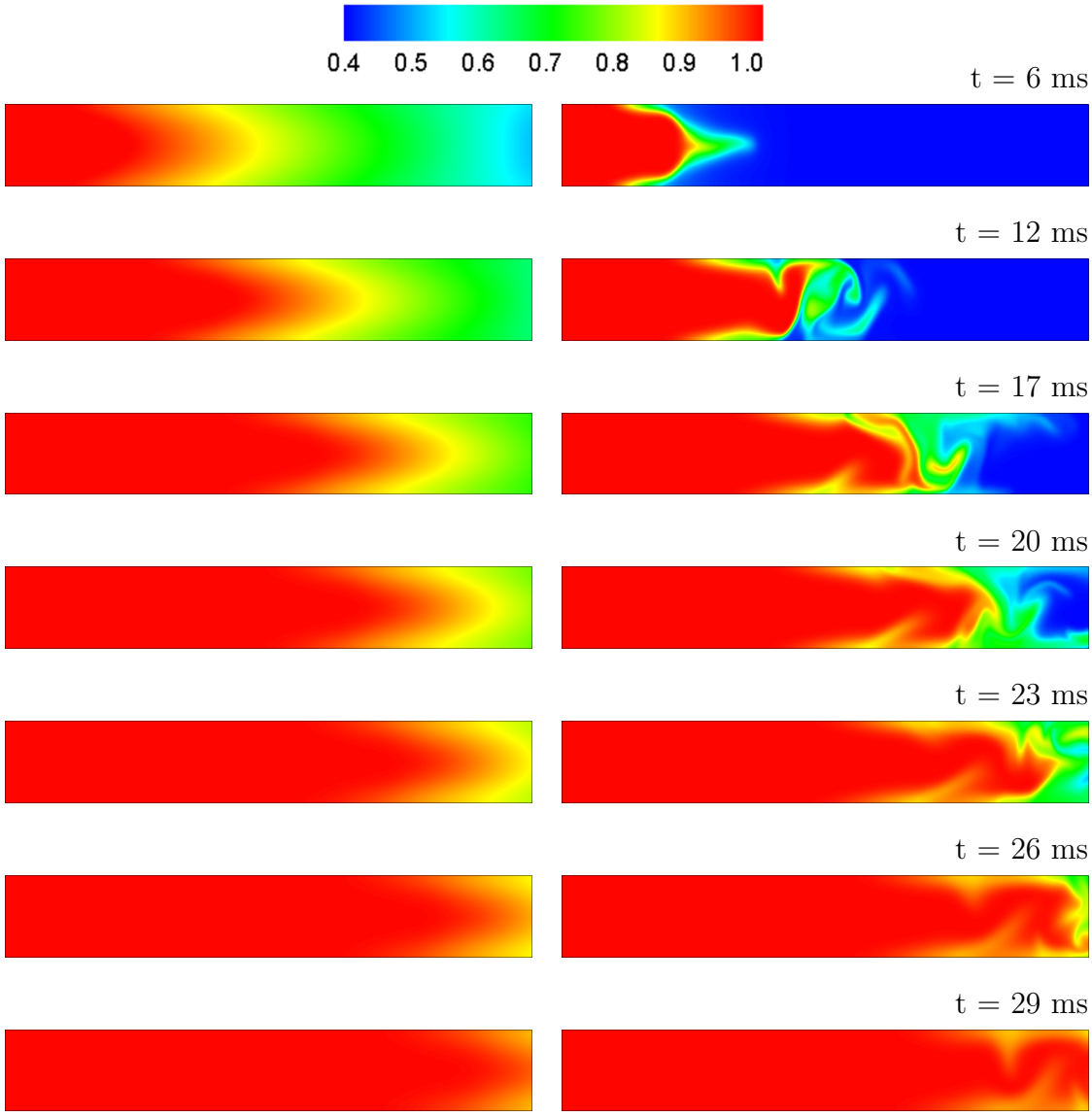

(a) Linear initialization strategy (b) Exponential initialization strategy

Fig. 4.17. Snapshots of the conductivity field evolved from different initial conductivity gradients under $E = 2500$ V/cm.

vious case. If an even higher electric field, for example, $E = 5000$ V/cm, is applied for the channel, instability phenomena can be found even in the flow with lower conductivity gradient. As shown in the left column of Figure 4.18, the flow with lower conductivity gradient that would not undergo instability in previous cases becomes

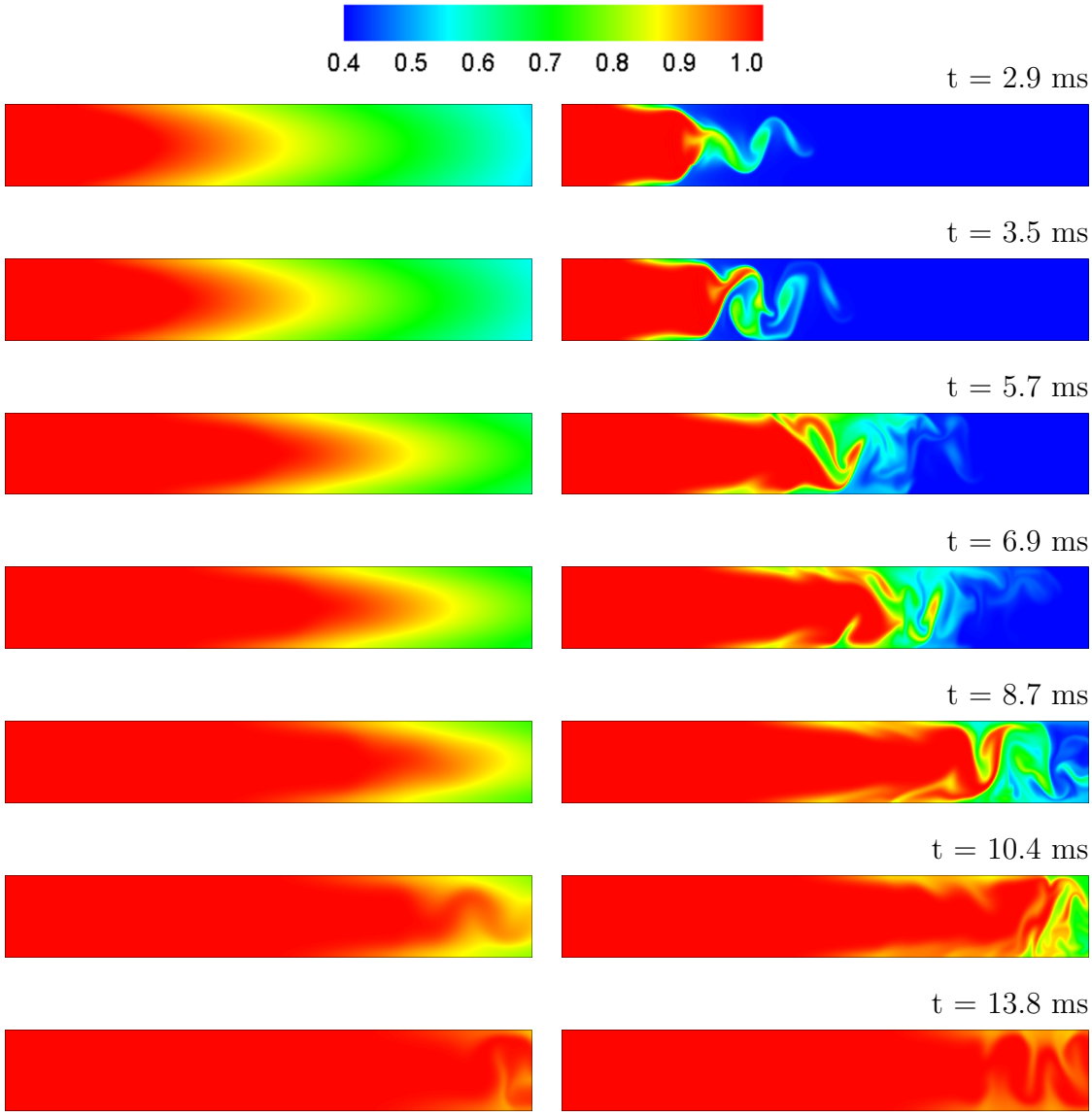

(a) Linear initialization strategy (b) Exponential initialization strategy

Fig. 4.18. Snapshots of the conductivity field evolved from different initial conductivity gradients under $E = 5000$ V/cm.

unstable before it is about to move out of the channel. This indicates that even for a flow with low conductivity gradient, EKI could be still invoked if the applied electric field is sufficient strong. As for the flow with higher conductivity gradient in this case, the instability is much more severe than the previous cases. In addition, according

to the simulation results for different cases presented here it can be seen that as the strength of the applied electric field increases, the velocity of the flow increases as well and it takes shorter and shorter time for the flow to move through the channel.

4.2.2 Orthogonal Gradient Case

The type II initial state for EKI as shown in Figure 4.14 (b) is considered in this subsection. Two buffer streams with different electrical conductivity are introduced into a two-dimensional straight microchannel. One stream with a high conductivity σ_H initially occupies the upper half of the channel while the other stream with a low conductivity σ_L occupies the lower half of the channel. As a result, an interface is formed at the horizontal central-line of the channel and a diffuse conductivity gradient is along width-direction of the channel. When different electrical potentials are imposed at the inlet and the outlet, the applied electric field is orthogonal to the conductivity gradient. Here, assume the conductivity ratio is $\gamma = \sigma_H/\sigma_L = 2.5$. The width and the length of the rectangular channel are 1.0 mm and 3.6 mm respectively. Other physical parameters and scales are from [29] as listed in Table 4.5. Then the important nondimensional parameters used in the simulation are calculated as $Re \approx 108$, $Ra_e \approx 54141$ and $Rv \approx -179$ which are consistent with [29].

As described in [29], the diffuse conductivity interface was approximately 75 μm wide compared to the width of the channel which is 1 mm. Then the exponential function 4.33 is used to define this interface and set up the initial state for conductivity field. The electrical potential field is still assumed uniform and thus is initialized by the linear function 4.31. The electrokinetic flow in the channel is initially at rest and no external pressure differences are imposed at the inlet and the outlet. Boundary conditions 2.22a-2.22d at the walls, 4.29a-4.29d at the inlet, and 4.30a-4.30d at the outlet are adopted in the simulations.

A representative set of images from simulations performed at the electric fields $E = 400$ V/cm, $E = 750$ V/cm, and $E = 1050$ V/cm are shown in Figure 4.19. For

Table 4.5
Parameters and fundamental scales used in 2D simulations of EKI for the orthogonal gradient case.

Symbol	Description	Value
w	Length scale (half width of the channel)	$5.0 \times 10^{-4}[m]$
μ	Absolute viscosity of fluid	$1.0 \times 10^{-3}[kg \cdot m^{-1}s^{-1}]$
ρ	Density of fluid	$1.0 \times 10^{3}[kg \cdot m^{-3}]$
ϵ	Permittivity	$6.93 \times 10^{-10}[C \cdot V^{-1}m^{-1}]$
D_{eff}	Effective diffusivity	$2.0 \times 10^{-9}[m^2s^{-1}]$
E_0	Reference electric field	$2.5 \times 10^{4}[V \cdot m^{-1}]$
ζ_0	Reference EDL zeta-potential	$-7.0 \times 10^{-2}[V]$

each case, the successive images show the temporal evolution of the conductivity field under a constant (DC) electric field. In each column, the top figure gives the initial, undisturbed interface between the two buffer streams with different conductivity.

In Figure 4.19, the red color represents the high-conductivity stream, and the blue color refers to the low-conductivity stream. The physical time considered in the simulation is 5 seconds, and the time of the snapshots is given in each row in the figure. At the electric field of 400 V/cm, only slight fluctuations are observed at t = 5.0 s. Then this electric field may be considered as the threshold field for the time period of interest here. At the two higher applied electric fields, small amplitude waves observed at the early stage quickly grow. As the fluid motion becomes unstable, it buckles the conductivity interface and proceeds to stretch and fold material lines. After t = 4.0 s, at the electric field of 1050 V/cm it results in a well-stirred, nearly homogeneous conductivity concentration field. All the phenomena captured by the simulation including a threshold field and scalar features are qualitatively consistent with the phenomena observed in the experiments provided by [29].

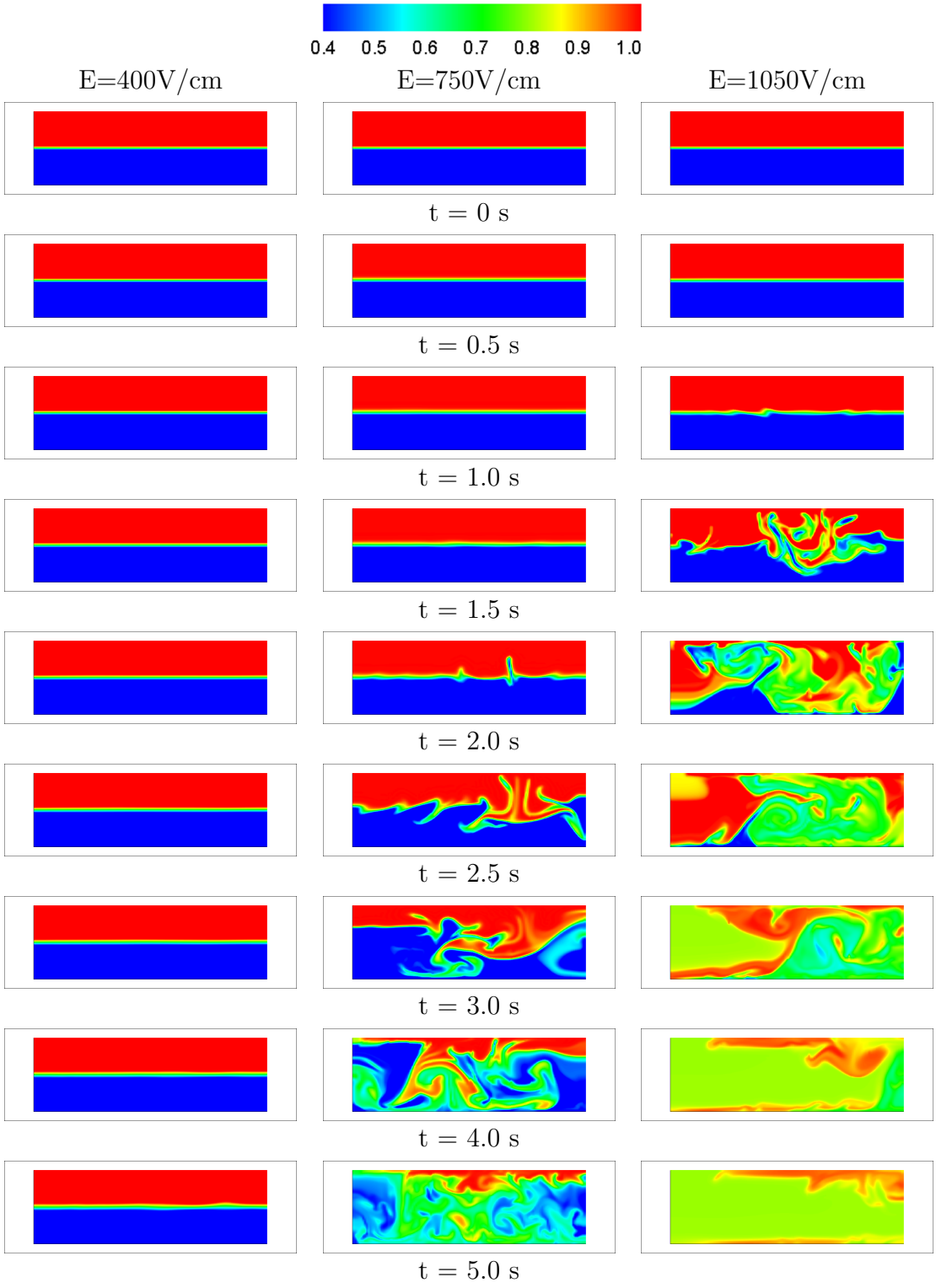

Fig. 4.19. Representative simulation snapshots of conductivity field from the simulation for $E = 400$ V/cm, $E = 750$ V/cm, and $E = 1050$ V/cm corresponding to the first, second, and third column.

4.2.3 Discussion and Summary

In this section 4.2, a series of simulations for two typical initial states for EKI in a simple two-dimensional straight microchannel are performed to understand the basic mechanism and behavior of EKI. In general, fluid flows in microchannels with conductivity gradients subjected to strong external applied electric fields can undergo violent instability and display turbulent characteristics at low Reynolds number.

From the simulation results of type I initial state for EKI as shown in the subsection 4.2.1, it can be found that under the same applied electric fields, the higher the initial conductivity gradients are the more violent instability occurs. On the other hand, for the same initial conductivity gradients the higher the applied electric fields are, the quicker the flow is driven to move and the more vigorous instability can be observed. From the mathematical point of view, this can be explained from the governing equations (2.18a)-(2.18e). The interaction of conductivity gradients and electric fields creates charge density in the fluid flow, see Equations (2.18a)-(2.18c). Then the external applied electric field exerts an electrical body force on this internally generated charge and drives the fluid to move, see Equation (2.18e). In other words, it is conductivity gradients interacting with the applied electric fields that generates fluid motion. Therefore, electric fields and conductivity gradients play an important role in the onset of EKI.

The simulation results of type II initial state for EKI provided in the subsection 4.2.2 show that there is a threshold electric field for the onset of EKI. This states that the electrokinetic flow would remain stable under an electric field that is below the threshold value. However, if the electric field exceeds the threshold value the electrokinetic flow would become unstable and instability phenomena occur. This can be, mathematically, explained by the diffusion term in the conservation equation of conductivity (2.18a). In the work of both Baygents et al. [101] and Lin et al. [29], they pointed out that viscous diffusion alone does not provide a sufficient stabilizing mechanism and molecular diffusion has an important stabilizing effect in

electrokinetic flows. On the one hand, with a time scale of $\tau_d = w^2/D_{eff}$ molecular diffusion relaxes the conductivity gradient that is correlated with charge density and the electrical body force in a way as shown in Equations (2.18c) and (2.18e). On the other hand, the instability grows with the electroviscous time scale [102] $\tau_{ev} = w/U_{ev}$. Thus, instability occurs only when the perturbations grow fast enough to overcome molecular diffusive relaxation. The ratio of τ_d and τ_{ev} gives the electric Rayleigh number defined in Equation (2.19) which is the critical parameter for the onset of instability. In conclusion, the diffusive conductivity term included in Equation (2.18a) is indeed required to capture a threshold instability condition. In addition, similar phenomena were also found in type II initial state compared to those observed in the type I initial state for EKI. For the type II initial state, after the onset of EKI the higher the electric field is applied the more rapidly and severely the instability grows.

5. HIGH FIDELITY SIMULATION OF EKI IN A THREE-DIMENSIONAL CROSS-SHAPED MICROCHANNEL

In this chapter, a series of numerical simulations are performed to study instabilities that develop in the primary step of a pinched flow electrokinetic injection in a cross-shaped microchannel. This realistic cross-shape flow geometry is directly relevant to electrokinetic injection studies, electrokinetic mixing schemes, and sample pre-concentration processes that make use of conductivity gradients [20].

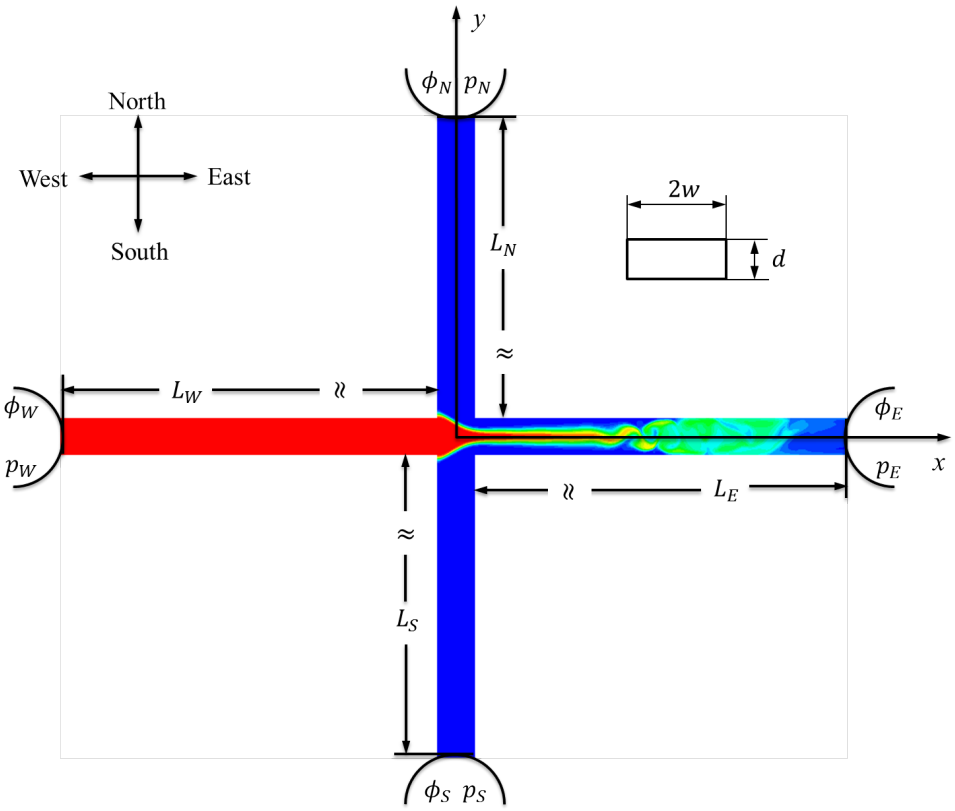

Fig. 5.1. Schematic of the electrokinetic flow in a cross-shaped microchannel.

5.1 Problem Description and Simulation Details

Figure 5.1 shows the top view of the cross-shaped microchannel. The channel lengths of the cross-shaped microchip are denoted by L_n, where the subscript n refers to the east (E), north (N), west (W) and south (S). In experiments, the channels typically have the characteristic D-shape cross-sections of isotropic etching with half-width w and depth d. Since the present solver was developed to handle complex geometries that fit Cartesian grid, the cross-sections of the channels are assumed to be rectangular in the current numerical study. Buffered aqueous solutions flow toward the channel intersection from the north (top), south (bottom) and west (left) wells, and flow away from the intersection along the positive x-axis (streamwise direction) towards the east (right) well. The sheath streams flow symmetrically from the north and south wells if the same electric fields are applied in the two channels. Both of the two sheath streams have an ionic conductivity σ_S, i.e. $\sigma_S = \sigma_N$. The sample stream from the west well has a conductivity σ_W. A conductivity ratio is introduced to relate the two conductivities by $\gamma = \sigma_W/\sigma_S$. From the experimental phenomena provided by [20] and [32], the center stream is sandwiched between the sheath streams forming a double conductivity interface in the east channel. As what will be discussed in this chapter, when the distortion of the conductivity interfaces due to internally-generated electroviscous velocities occurs more rapidly than the dispersion of this interface due to molecular diffusion, electrokinetic flows become unstable. An example of such instability obtained from the simulation result is shown in Figure 5.1, which is consistent with the phenomena observed in the experiments presented in the literature [20]. Electrical potentials ϕ_n are applied at the wells at the end of each channel. The applied potentials in the north and south wells can be maintained the same, i.e. $\phi_N = \phi_S$, for a symmetric electric field case, or can be varied differently for a non-symmetric applied field case. The ratio of the west (sample) well to the north/south (sheath) well potentials can actually be used to control the width of the center stream which will be discussed later in this chapter. In addition, as we focus on the study

of electrokinetic effects, no external pressure gradient is imposed at each well such that $p_E = p_N = p_S = p_W$.

In the numerical simulation, proper wall boundary conditions 2.22a-2.22d are imposed at the walls of the channel. Conditions 4.29a-4.29d are applied at all the three inlets for the east, north, and south channels, respectively. Conditions 4.30a-4.30d are adopted at the outlet for the west channel.

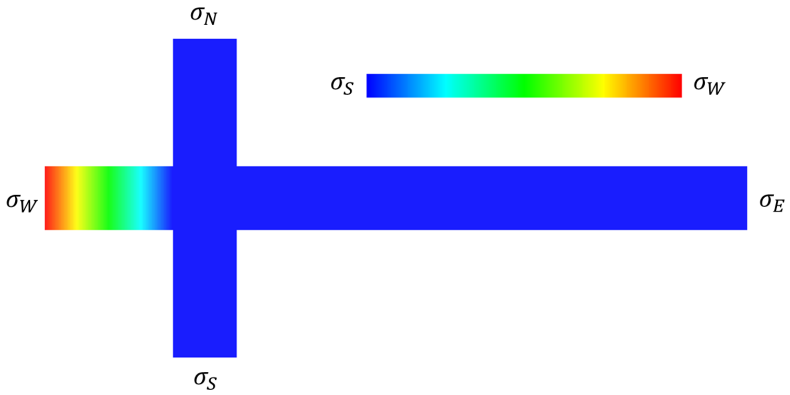

(a) Conductivity field initialized by linear function

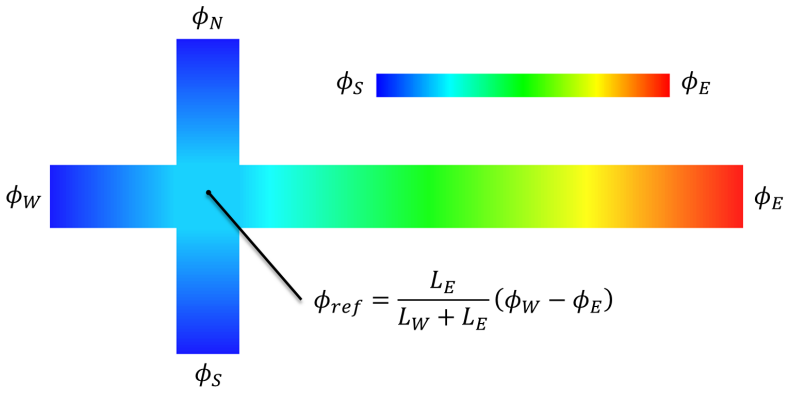

(b) Electric field initialized by linear function

Fig. 5.2. Schematic diagrams of initialization of conductivity and electric potential fields in the cross-shaped microchannel.

To initialize the conductivity field for the cross-shaped flow geometry, the linear function 4.31 is used to set conductivity in the west channel while conductivity in the north, south, and east channels is all set to σ_S. Then the initialized conductivity field

for the cross-shaped channel could look like Figure 5.2 (a). For the initialization of the electric potential field, the potentials at the end of each channel are determined at first according to the corresponding electrical fields and channel lengths. Then a proper reference potential is set at the intersection region of the channel. Finally the linear function 4.31 is used to initialize the electric potentials in each channel. An example of the initialized electric potential for $\phi_W = \phi_N = \phi_S$ is shown in Figure 5.2(b).

In order to efficiently and clearly present the results, several parameters such as the conductivity ratio γ, the nominally applied field E_a, and electric field ratios β_W and β_N are introduced. The quantities γ, E_a, β_W and β_N are defined as follows

$$\gamma = \frac{\sigma_W}{\sigma_S} \tag{5.1a}$$

$$E_a = \frac{\phi_S - \phi_E}{L_E + L_S} \tag{5.1b}$$

$$\beta_W = \frac{\phi_W - \phi_E}{E_a(L_W + L_E)} \tag{5.1c}$$

$$\beta_N = \frac{\phi_N - \phi_E}{E_a(L_W + L_E)} \tag{5.1d}$$

The nominal applied field E_a for the flow field is the potentials applied between the south and east channel reservoirs divided by the appropriate channel lengths. In the experiments presented in [20], this characteristic field is used as a function of directly specified experimental parameters. The electric field ratio β_W is a ratio between the west and south nominal fields, while β_N is a ratio between the north and south nominal fields. If the lengths of the north, south, and west channels are identical, i.e. $L_N = L_S = L_W$ and the outlet of the east channel is grounded, i.e. $\phi_E = 0\ V$, these two electric field ratios become the ratio of the west to the south electric potentials and the ratio of the north to the south electric potentials respectively, i.e. $\beta_W = \phi_W/\phi_S$ and $\beta_N = \phi_N/\phi_S$.

In the following subsections, numerical simulations are conducted to study the EKI phenomena observed in the experiments done by Luo [32] and by Posner et al. [20]. Basically, these two papers investigated very similar flow geometry and EKI

phenomena. If not stated otherwise, microchannel parameters and fluid properties used in the simulations presented in this section are from [32] as summarized in Table 5.1. Then the obtained simulation results will be directly compared with the numerical and experimental results presented in [32], and qualitatively compared with the experiments presented in [20] as well.

Table 5.1
Parameters and fundamental scales used in the present three-dimensional EKI simulations taken from [32].

Symbol	Description	Value
w	Half width of the channel (length scale)	$3.0 \times 10^{-5}[m]$
d	Depth of the channel	$1.0 \times 10^{-5}[m]$
μ	Absolute viscosity of fluid	$0.9 \times 10^{-3}[kg \cdot m^{-1}s^{-1}]$
ρ	Density of fluid	$1.0 \times 10^{3}[kg \cdot m^{-3}]$
ϵ	Permittivity	$6.93 \times 10^{-10}[C \cdot V^{-1}m^{-1}]$
D_{eff}	Effective diffusivity	$1.0 \times 10^{-9}[m^2s^{-1}]$
E_0	Reference electric field	$2.5 \times 10^{4}[V \cdot m^{-1}]$
ζ	EDL zeta-potential	$-7.5 \times 10^{-2}[V]$

For all the simulation results presented in this chapter, a uniform grid with a spacing of $\Delta x^* \times \Delta y^* \times \Delta z^* = 0.025 \times 0.025 \times 0.016$ is adopted. Such spatial resolution was confirmed to be sufficient by comparing with a uniform mesh with a spacing of $\Delta x^* \times \Delta y^* \times \Delta z^* = 0.02 \times 0.02 \times 0.012$ for the case of steady EK flow through the downstream channel of the cross-shaped microchip. Electrical conductivity concentration profiles were examined at the outlet of the downstream channel when the EK flow reached the steady state under a relatively low electric field and it was found that the results obtained with the two computational meshes agree very well with each other. Thus, the uniform mesh with a spacing of $\Delta x^* \times \Delta y^* \times \Delta z^* = 0.025 \times 0.025 \times 0.016$ was deemed sufficient. The time step in the simulation is chosen as $\Delta t^* = 1 \times 10^{-3}$ to

1×10^{-4} depending on the strength of applied electric fields as in the cases in which the EK flow is under a high electric field it requires a smaller time step to maintain the numerical stability of the solver.

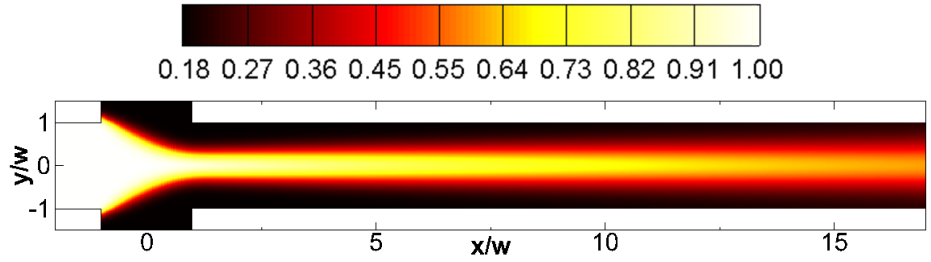

(a) Conductivity concentration field obtained by the upwind scheme.

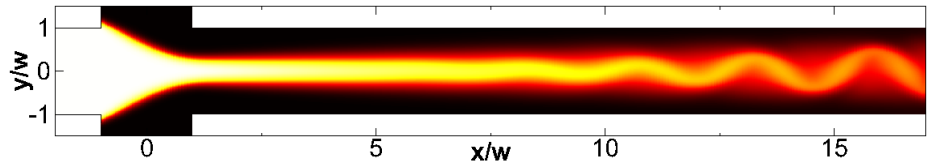

(b) Conductivity concentration field obtained by the present WENO solver.

Fig. 5.3. Representative instantaneous conductivity concentration field for $E_a = 350$ V/cm, $\gamma = 5.5$ and $\beta_W = \beta_N = 1.0$ in a cross-shaped microchannel.

Before performing high fidelity EKI simulations, again, we compare the first-order upwind scheme with the fifth-order WENO scheme to confirm that the present WENO solver is a better numerical tool to simulate EKI phenomena. We use the parameters listed in Table 5.1 and consider a cross-shaped microchannel with the following dimensions: the lengths of the north, south, and west channels are identically $150\mu m$ long and the length of the east channel is $510\mu m$. 60 blocks are arranged to exactly compose such flow geometry. Thus, for the uniform mesh with a spacing of $\Delta x^* \times \Delta y^* \times \Delta z^* = 0.025 \times 0.025 \times 0.016$, the mesh size is $41 \times 41 \times 21 \times 60 \approx 2.12$ million grid points. Assume that a constant DC voltage, i.e. the same value of electric potential, is applied at the three inlets while the outlet in the east channel is grounded. This results in the parameters $\beta_W = \beta_N = 1.0$ and $E_a = \phi_S/(L_E + L_S) = \phi_W/(L_W + L_E)$.

Two electrolyte solutions, one with a low conductivity σ_S from the north and south inlets and one with a high conductivity σ_W from the west inlet, are introduced into the microchip. The conductivity ratio is assumed to be $\gamma = \sigma_W/\sigma_S = 5.5$.

Figures 5.3 and 5.4 give the results obtained by the upwind scheme and the present Weno solver under the applied electric fields of $E_a = 350V/cm$ and $E_a = 600V/cm$, respectively. From the figures it can be seen that as the upwind scheme introduces more numerical diffusion to the solution, at a relatively low electric field of $E_a = 350V/cm$ (but high enough to trigger the EK instability according to the experiments given in [32]) the upwind scheme fails to capture instable phenomenon, see Figure 5.3(a). While at the higher electric field of $E_a = 600V/cm$, the upwind scheme offers less details of EKI phenomena compared to the WENO solver when looking at the shape of the injection head and disturbed throat in the upstream region and the pattern of EKI in the downstream region.

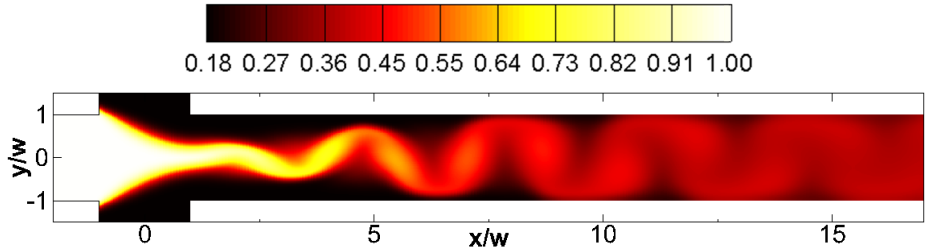

(a) Conductivity concentration field obtained by the upwind scheme.

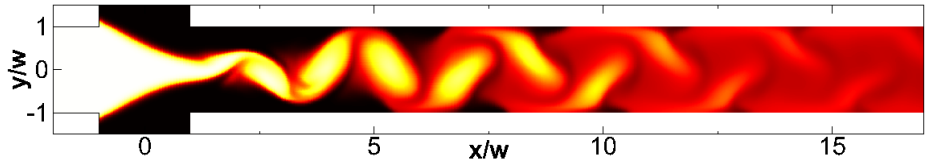

(b) Conductivity concentration field obtained by the present WENO solver.

Fig. 5.4. Representative instantaneous conductivity concentration field for $E_a = 600$ V/cm, $\gamma = 5.5$ and $\beta_W = \beta_N = 1.0$ in a cross-shaped microchannel.

Again, it clearly shows that the performance of the fifth-order WENO scheme is better than the first-order upwind scheme. Thus, the present WENO solver is a good

numerical tool to simulate EKI phenomena in microfluidic devices. Detailed EKI simulation results for different conditions will be given in the following subsections.

5.2 Specific Case Study

In [32], both experimental and two-dimensional numerical investigations were performed for EKI phenomena in a cross-shaped microchannel when the conductivity ratio $\gamma = 3.5$ or $1/3.5$ under $E_a = 778V/cm$. In this subsection, three-dimensional simulations for the same two specific cases are conducted to validate whether the present WENO solver can capture critical EKI features. A cross-shaped microchip with the following dimensions is considered: the lengths of the north, south, and west channels are identically $150\mu m$ and the length of the east channel is $870\mu m$. 84 blocks are arranged to exactly compose the flow geometry and within each block the mesh size is $41 \times 41 \times 21$ which makes a total resolution of about 3.0 million grid points for the computational domain. For the simulations given in the following two subsections 5.2.1 and 5.2.2, the electric field ratios are assumed to be $\beta_W = \beta_N = 1.0$ which are consistent with the study presented in [32].

5.2.1 $\gamma = 3.5$ under $E_a = 778$V/cm

Three-dimensional simulations for the conductivity ratio $\gamma = 3.5$ at $E_a = 778$V/cm are carried out in this subsection using the WENO solver. The obtained numerical results are compared with the experimental as well as the simulation results given in [32]. According to the experiments presented in [32], the threshold value of the applied electric field E_a for the onset of EKI was found to be $E_a = 385$V/cm. Thus in the simulation, a lower electric field of $E_a = 360V/cm$ is imposed to achieve the steady state first. Then a DC voltage with a strength of 778 V/cm which is higher than the threshold electric field is applied at the three inlets to invoke the EKI effect. Figure 5.5 shows the temporal evolution of the fluid stream electrical conductivities (top view of the microchannel) under $E_a = 778$V/cm for $\gamma = 3.5$ and $\beta_W = \beta_N = 1.0$.

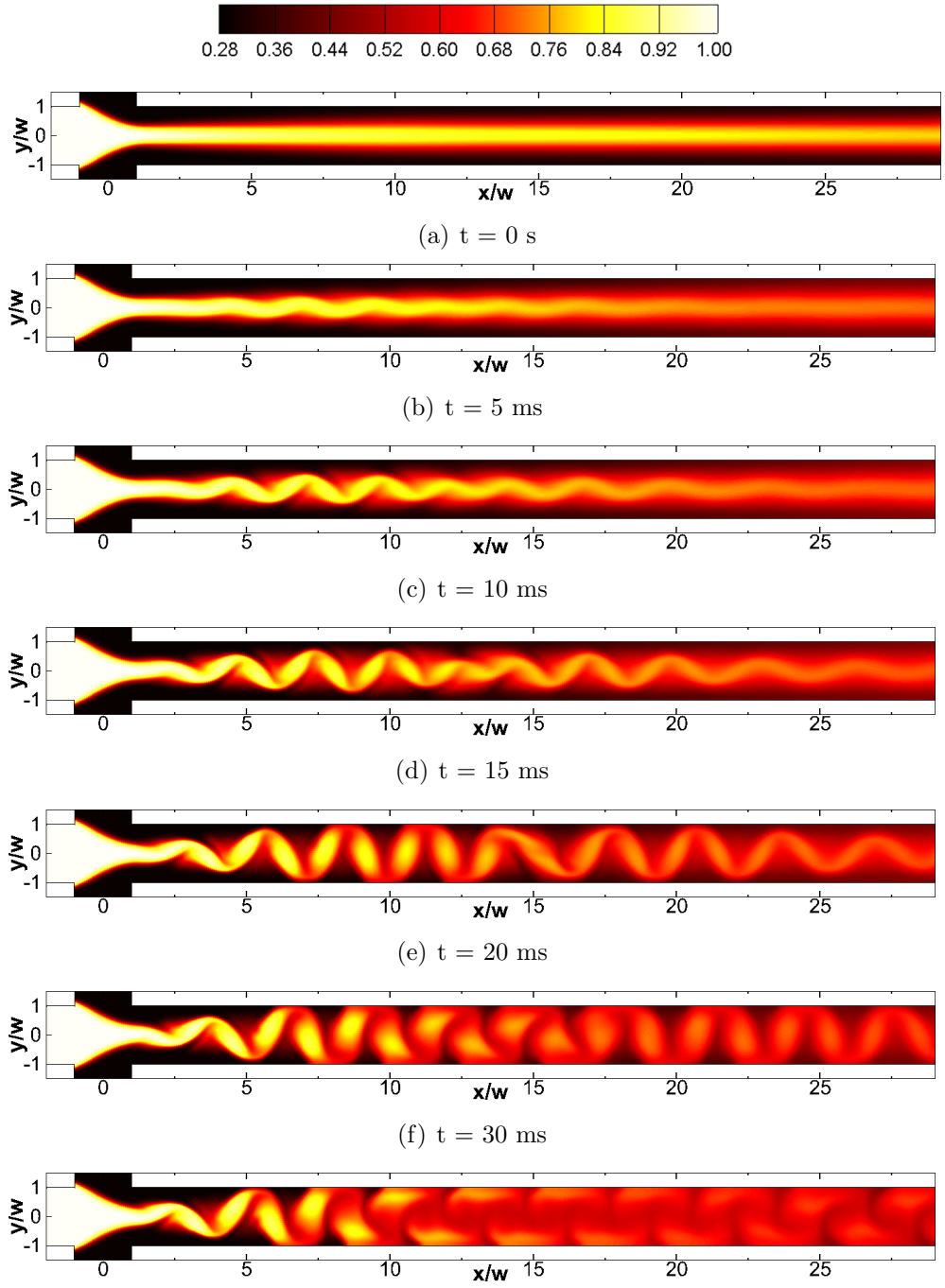

(a) t = 0 s

(b) t = 5 ms

(c) t = 10 ms

(d) t = 15 ms

(e) t = 20 ms

(f) t = 30 ms

(g) t = 100 ms

Fig. 5.5. Evolution of conductivity concentration for $E_a = 778$ V/cm, $\gamma = 3.5$ and $\beta_W = \beta_N = 1.0$ in a cross-shaped microchannel.

As shown in Figure 5.5 (a), when the electrolyte solutions are smoothly introduced into the east channel from the three inlet channels under the steady condition, the sample stream with a high conductivity σ_W from the west channel is pinched by the two sheath streams with a low conductivity σ_S from the north and south channels. In the channel intersection region, a triangle-shaped injection head is formed and the two interfaces are clearly defined. From the steady state when the time is counted as t = 0 s, a high external electric field $E_a = 778$V/cm is applied to the microchannel. In a very short time, i.e. at t = 5 ms as shown in Figure 5.5 (b), perturbation at the two interfaces between the sample stream and the sheath streams near the triangle-shaped head is observed along the downstream direction. Over the interval from t = 5 ms to t = 20 ms, the straight interfaces formed in the steady state are buckled into a wave-like pattern and the perturbation phenomenon becomes more and more severe. In the entrance region of the east channel, the high-conductivity sample stream periodically fluctuates up and down between the upper and lower walls. This results in a series of circulations in the downstream region. As time elapses, after t = 30 ms the conductivity concentration fluctuations with a periodic and symmetrical alignment are formed and occupy the full channel width along the downstream direction.

Figure 5.6 shows the comparison among the experimental and the two-dimensional simulation results presented in [32] and the three-dimensional simulation results obtained by the present solver at $E_a = 778$V/cm for $\gamma = 3.5$ and $\beta_W = \beta_N = 1.0$. Figure 5.6(a) are the fluorescent images from the experiments by [32] showing the distribution of the sample stream with high conductivity in the east channel. From the experimental visualization, apparent disturbances were found. Coherent structures caused by the disturbances originated from near the pinched throat at $x/w \approx 1.5$ at the upstream section. At the downstream section, conductivity concentration fluctuations with a periodic alignment occupy the full width of the channel. From the two-dimensional simulation results as shown in Figure 5.6(b), however, more severe instabilities were observed. The source of disturbances moved from the throat at

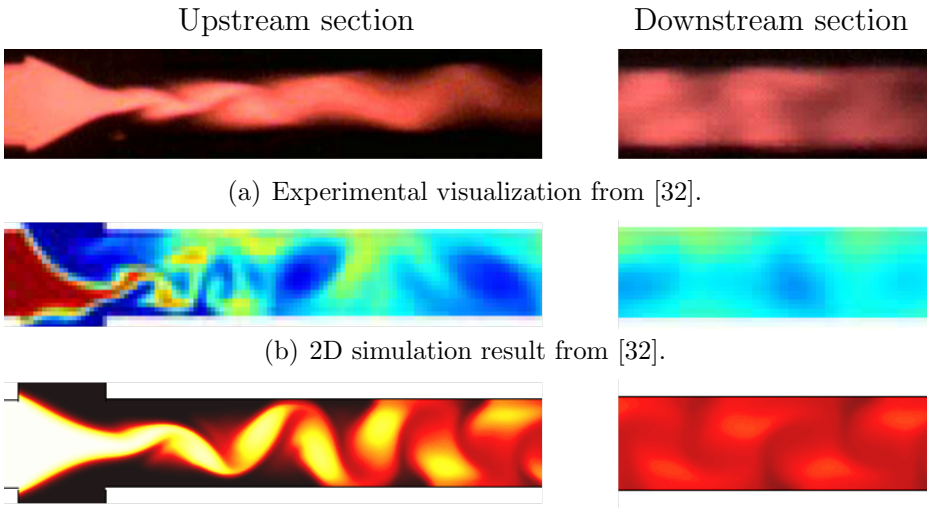

(a) Experimental visualization from [32].

(b) 2D simulation result from [32].

(c) 3D simulation result by the present WENO solver.

Fig. 5.6. Comparison among the experimental result, the 2D simulation results presented in [32], and the 3D simulation results obtained by the present WENO solver for $E_a = 778\text{V/cm}$, $\gamma = 3.5$ and $\beta_W = \beta_N = 1.0$.

the upstream section to the triangle-shaped head. This results in the entire injection head also periodically oscillated along the y-direction in the intersection region. At the downstream section, no periodic fluctuations were observed though the scalar concentration was distributed to the full width of the channel. The three-dimensional simulation results obtained in the present work are provided in Figure 5.6(c). Though obvious instabilities are found for sure, the triangle-shaped head does keep staying in the intersection region. Coherent structures are formed after the head near the location of $x/w \approx 1.5$. Then the disturbances convect downstream and grow rapidly. At the downstream of the throat, the concentration of conductivity periodically fluctuates up and down. High conductivity is thus left near the upper and lower walls while the concentration of conductivity in the central region between the two walls is relatively low. From the observation, it is apparent that three-dimensional simulations give a better qualitative agreement with the experimental results compared to the two-dimensional simulations.

5.2.2 $\gamma = 1/3.5$ under $E_a = 778$V/cm

In this subsection, the case of the conductivity ratio $\gamma = 1/3.5$ is considered. In contrast with the previous case, an electrolyte stream with a low conductivity concentration is injected from the west channel, while two high-conductivity solutions are introduced into the microchip via the north and the south channels. Like what has been done in the $\gamma = 3.5$ case, a steady state was achieved first by imposing an electric field that is lower than the threshold value. Notice from the experiments conducted in [32], the threshold value for the nominal electric field was found to be $E_a = 355$ V/cm. Thus a lower electric field of $E_a = 340$ V/cm is imposed to obtain the equilibrium condition. Then the electric field strength is increased to $E_a = 778$ V/cm to trigger EKI phenomena.

Figure 5.7 shows the temporal evolution of the conductivity field (top view of the microchannel) for $\gamma = 1/3.5$ and $\beta_W = \beta_N = 1.0$ at $E_a = 778$V/cm. At the steady state from which the time is counted as $t = 0$ s, the low-conductivity sample stream from the west channel is sandwiched in the central region of the east channel by the two high-conductivity electrolyte solutions from the north and south channels. Similar to what was observed in the $\gamma = 3.5$ case, a triangle-shaped injection head is formed in the channel intersection region and two interfaces that split the three electrolyte streams are clearly defined, see Figure 5.7 (a). As shown in Figures 5.7 (b)-(e), in the presence of the strong electric field of $E_a = 778$ V/cm after about 20 ms , the EK flow becomes unstable and the original straight interfaces are symmetrically perturbed. As the EK flow moves toward the outlet in the east channel, the central low-conductivity stream is squeezed or stretched by the two outer high-conductivity streams due to the wave-like perturbations. Notice that the perturbations always maintain symmetric though the two interfaces break off somehow as the perturbations develop in the east channel, see Figures 5.7 (e) and (f). As time further passed by, a melon-seed-shaped structure is formed in the upstream region while a string of individual pearl-like structures is observed in the downstream region, see Figure 5.7(g).

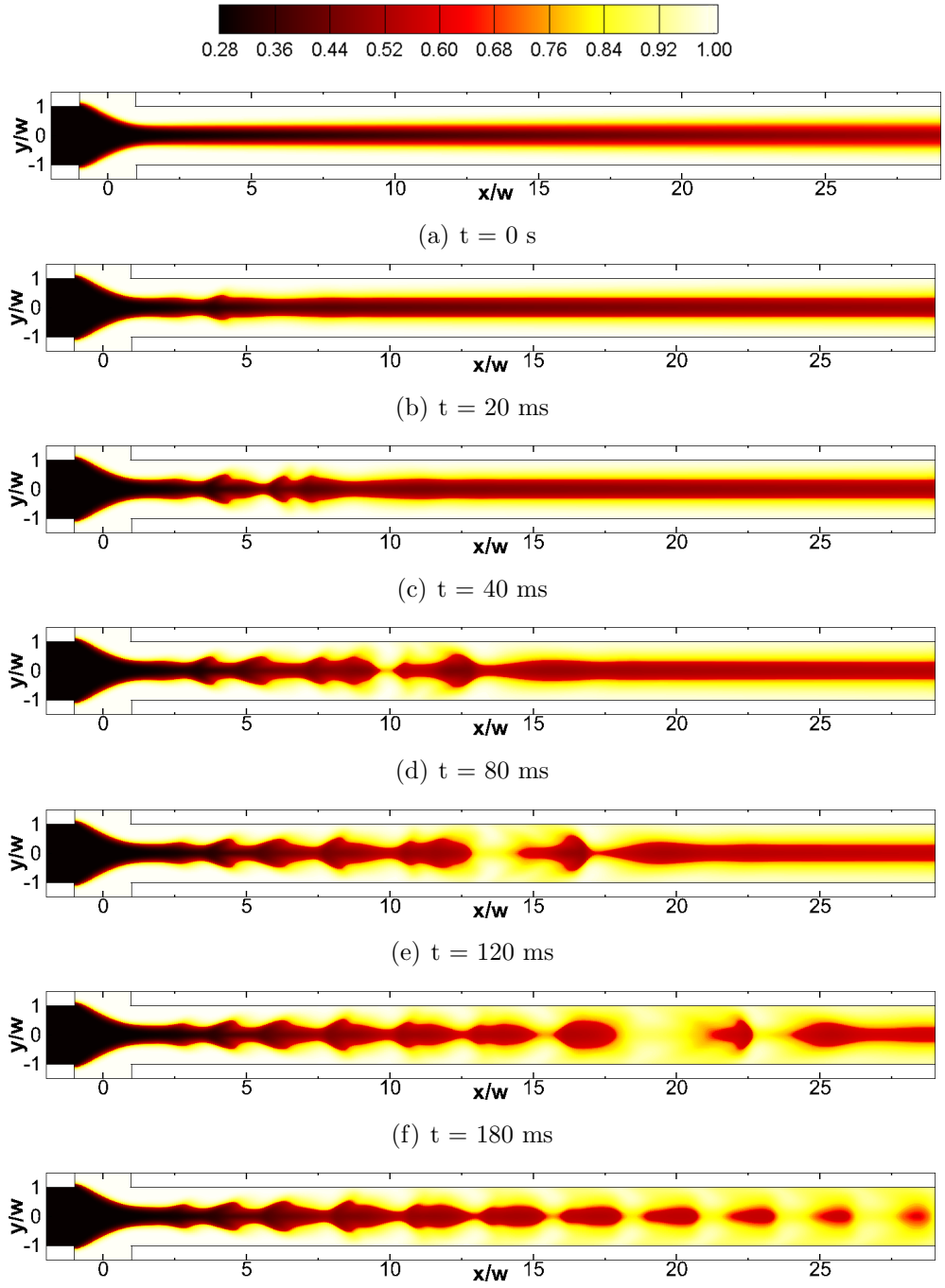

(a) t = 0 s

(b) t = 20 ms

(c) t = 40 ms

(d) t = 80 ms

(e) t = 120 ms

(f) t = 180 ms

(g) t = 300 ms

Fig. 5.7. Evolution of conductivity concentration for $E_a = 778$ V/cm, $\gamma = 1/3.5$ and $\beta_W = \beta_N = 1.0$ in a cross-shaped microchannel.

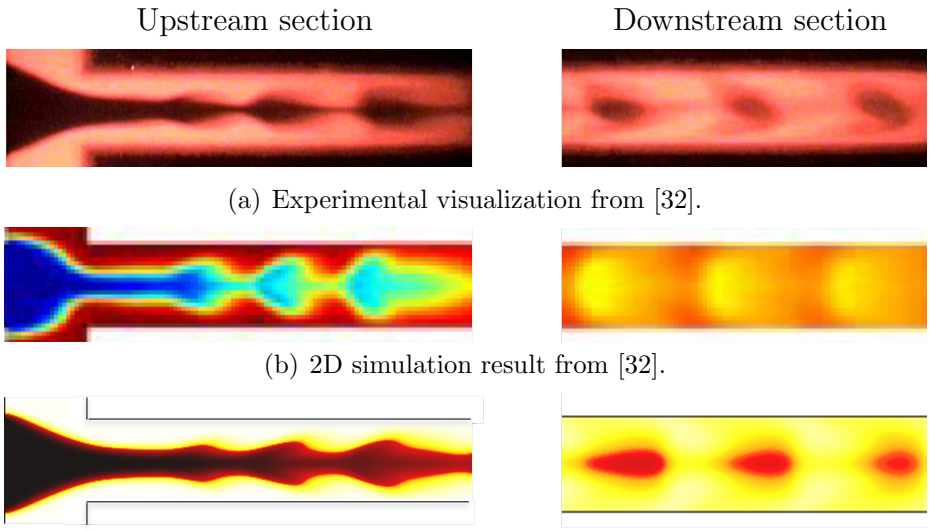

(a) Experimental visualization from [32].

(b) 2D simulation result from [32].

(c) 3D simulation result by the present WENO solver.

Fig. 5.8. Comparison among the experimental result, the 2D simulation results presented in [32], and the 3D simulation results obtained by the present WENO solver for $E_a = 778\text{V/cm}$, $\gamma = 1/3.5$ and $\beta_W = \beta_N = 1.0$.

Again, we compare the the three-dimensional numerical results obtained by the WENO solver with the experimental and the two-dimensional simulation results presented in [32] at $E_a = 778\text{V/cm}$ for $\gamma = 1/3.5$ and $\beta_W = \beta_N = 1.0$. From the experimental visualization as given in Figure 5.8 (a), a pearl-like structure is clearly observed and such structure moderately propagates along the downstream direction. Both the two-dimensional and the three-dimensional simulations basically capture such instable electrokinetic phenomena. However, the three-dimensional results obtained by the present WENO solver offers a more similar phenomena compared to the experiments when looking at the shape of the disturbed interfaces between the central low-conductivity stream and the outer high-conductivity streams, for example, the triangular injection head in the channel intersection region, the melon-seed-shaped structure in the upstream region, and the pearl-like structure in the downstream region.

5.2.3 Discussion

From the results presented in the previous two subsections 5.2.1 and 5.2.2, it is clear to see that the present WENO solver is capable of accurately capturing the critical features of EKI in the cross-shaped microchannel. In addition, for the corresponding EKI phenomena it can be found that under the application of a relatively high electric field ($E_a = 778$ V/cm), instabilities occur in both two cases of $\gamma = 3.5$ and $\gamma = 1/3.5$. Actually these two cases are representative examples in two types of injection configurations/modes based on the conductivity ratio γ, i.e. the two injection configurations of $\gamma > 1$ and $\gamma < 1$ respectively. Suppose both of these two injection configurations are applied for micromixing (as one of the major applications of EKI in the considered cross-shaped microchannel is mixing), it is interesting and useful to find in which injection configuration a more rapid and efficient mixing can be achieved.

To quantify the degree of mixing within the microfluidic device, the concentration mixing intensity $I_m(x)$ at any cross section along the mixing channel (i.e. x-axis) is introduced by following [103]

$$I_m(x) = \left(1.0 - \frac{\int_0^d \int_0^{2w} |\sigma - \sigma_\infty| dydz}{\int_0^d \int_0^{2w} |\sigma_0 - \sigma_\infty| dydz}\right) \times 100\% \tag{5.2}$$

where, d and w are the depth and the half-width of the mixing channel respectively, σ is the species concentration across the mixing channel, σ_0 and σ_∞ are the species concentrations in the completely unmixed and completely mixed states, respectively.

Figure 5.9 shows the comparison of the conductivity mixing intensities along the downstream direction for the two injection configurations of $\gamma = 3.5$ and $\gamma = 1/3.5$ at $E_a = 778$ V/cm. From the numerical result for the case of $\gamma = 3.5$, it can be found that the mixing intensity starts at the entrance region of the east mixing channel at about 30%. In the upstream region, the mixing intensity grows rapidly in a wave-like pattern along the stream-wise direction. Then it increases to over 70% and keeps increasing slightly like a straight line after a mixing distance of $x/w \approx 12.0$. In the injection configuration of $\gamma = 1/3.5$, the mixing intensity, in contrast to that for

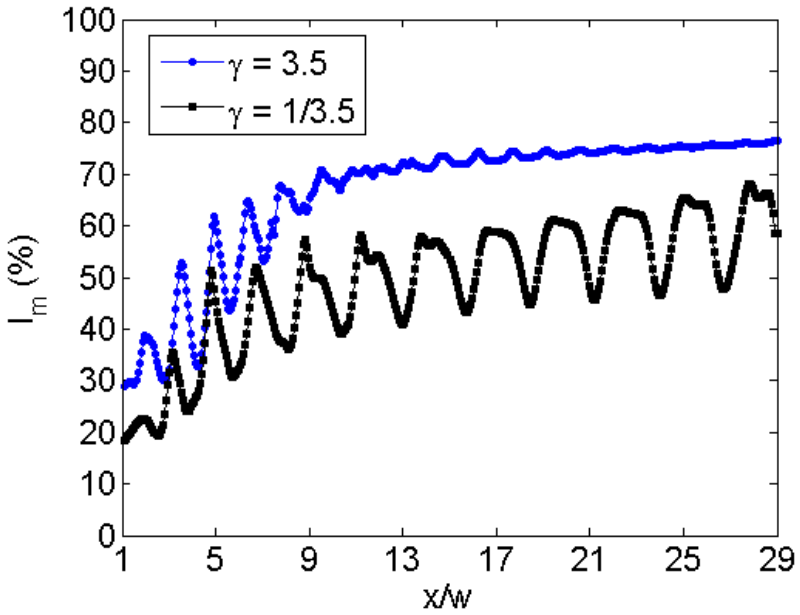

Fig. 5.9. Comparison of conductivity mixing intensities along the downstream direction for the two injection configurations of $\gamma = 3.5$ and $\gamma = 1/3.5$ at $E_a = 778$ V/cm.

the $\gamma = 3.5$ case, is lower throughout the east mixing channel. As shown in Figure 5.7(g), since a pearl-like structure is formed in the downstream channel along the low-conductivity stream, though the mixing intensity grows from the entrance region it always increases in a sinuous tendency. From a point of mixing, this large variation may not be acceptable as it may cause the heterogeneous composition of the mixture. In conclusion, compared to the injection configuration of $\gamma = 1/3.5$, the injection mode of $\gamma = 3.5$ offers a more rapid and efficient mixing effect. Thus, the injection mode with $\gamma > 1.0$ can be considered as a more appropriate choice for the application of micro-mixing in a cross-shaped microchannel. In the following general parametric study on EKI, we will focus on such injection mode rather than that with $\gamma < 1.0$.

5.3 General Parametric Study

In this section, we perform a general parametric study on EKI phenomena in a cross-shaped microchannel. Three-dimensional simulations are conducted to investigate the effects of different parameters including the conductivity ratio γ, the electric field strength E_a, the channel depth d, and the electric field ratios β_W and β_N on EKI. The parameters and fluid properties used in the simulations are still, if not stated otherwise, as listed in Table 5.1. A cross-shaped microchip with the following dimensions is considered: the lengths of the north, south, and west channels are identically $150\mu m$ and the length of the east channel is $510\mu m$. 60 blocks are arranged to exactly cover the flow geometry and the uniform mesh with a spacing of $\Delta x^* \times \Delta y^* \times \Delta z^* = 0.025 \times 0.025 \times 0.016$ is used for the corresponding computational domains for different cases. In the present parametric study on EKI, we focus on the injection mode for $\gamma > 1$, i.e. high conductivity in center stream from the west channel.

5.3.1 Effect of Conductivity Ratio on EKI

To investigate the effect of conductivity ratio γ on EKI, we conduct simulations for five different values of conductivity ratio γ varying from 1.5 to 10.0 by using the present WENO solver. The threshold values of the nominal electric field E_a for the corresponding cases are found numerically and summarized in Figure 5.10 with the experiment measurements provided by [32]. From the figure it can be seen that the present solver captures the critical electric fields for the onset of EKI at various conductivity ratios though for the low conductivity ratios, for example, γ from 1.5 to 5.5, the threshold values found in the simulations are a bit higher compared to the experiment results.

From the fundamental numerical study of EKI conducted in Section 4.2, we know that due to the interaction of conductivity gradients and electric fields an electrical body force is exerted on the EK flow and thus generates fluid motion. Under

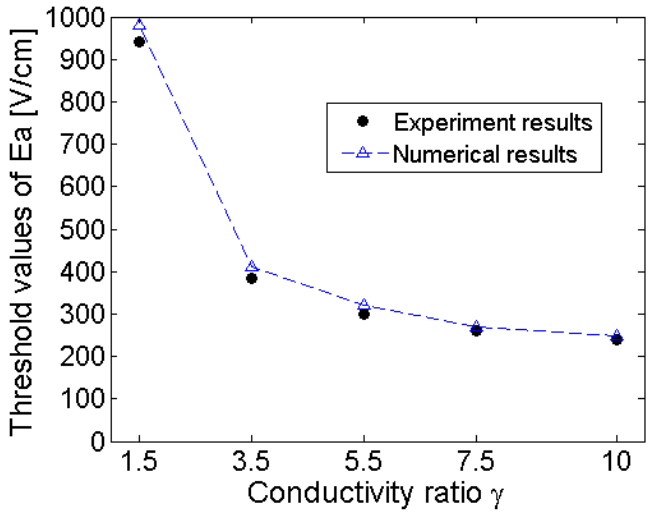

Fig. 5.10. The threshold values of the nominal electric field E_a for the conductivity ratio γ varying from 1.5 to 10.0.

the same applied electric field, when conductivity gradients are high (namely high conductivity ratio) more vigorous instabilities are expected to occur. The simulation results given in Figure 5.11 confirm such expected phenomenon. At the same applied field of $E_a = 650$ V/cm, the conductivity concentration field changes from the steady state, to periodic oscillation, and then to more vigorous unstable state (slightly non-periodic perturbation) as the conductivity ratio γ increases from 1.5 to 10.0, see Figures 5.11(a)-(e). For $\gamma = 1.5$, as $E_a = 650$ V/cm is lower than its threshold value (960 V/cm) according to Figure 5.10, the conductivity concentration field maintains stable, see Figure 5.11(a). As shown in Figure 5.11(b)-(d) with the increase of γ from 3.5 to 7.5, since the applied electric field of $E_a = 650$ V/cm exceeds the corresponding threshold values for all these cases periodic fluctuations are clearly observed in the downstream channel. The position of the coherent structures where the disturbances originate are changed from $x/w \approx 2.5$ to $x/w \approx 1.0$. For the highest conductivity ratio $\gamma = 10.0$, the concentration field starts to fluctuate non-periodically along the spanwise direction and the source of disturbances moves further upstream to $x/w < 1.0$, see Figure 5.11(e).

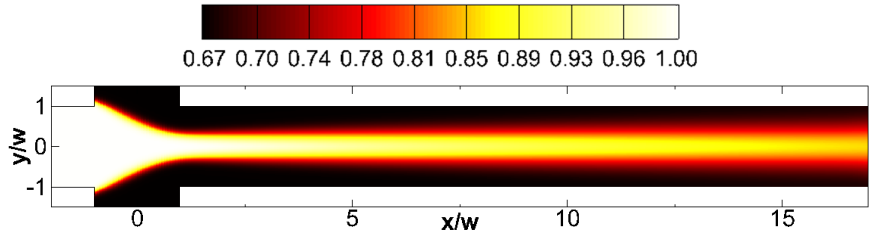

(a) $\gamma = 1.5$

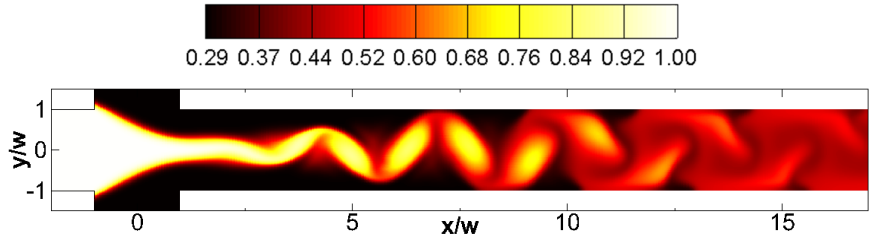

(b) $\gamma = 3.5$

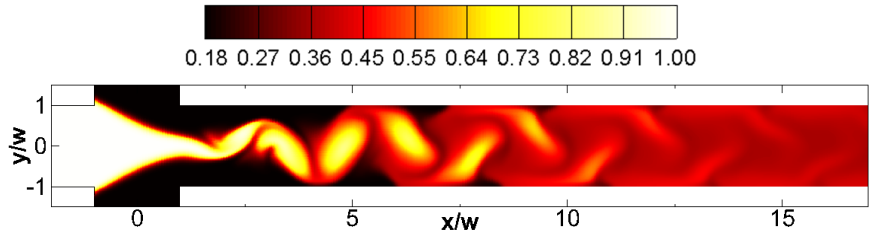

(c) $\gamma = 5.5$

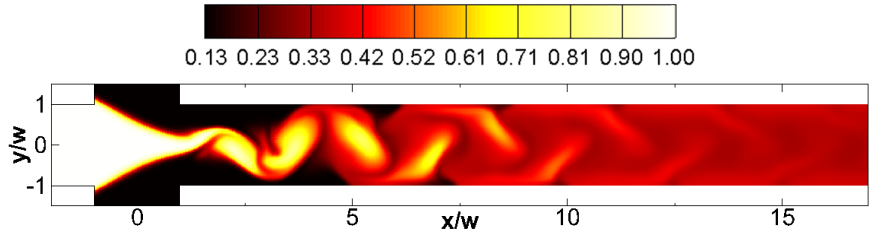

(d) $\gamma = 7.5$

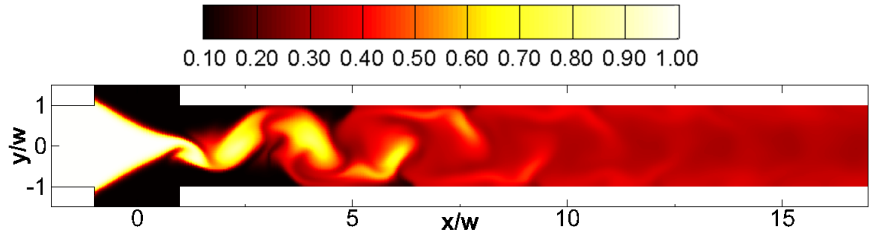

(e) $\gamma = 10.0$

Fig. 5.11. Representative instantaneous snapshots of conductivity concentration fields at an applied electric field of $E_a = 650$ V/cm for different conductivity ratios.

In order to gain insight into the disturbed scalar field, the average and perturbation concentration fields are calculated and presented. The time-averaged mean concentration field for the variable, conductivity $\sigma(x, y, z, t)$, can be defined as

$$\bar{\sigma}(x, y, z, t) = \frac{1}{T_f} \int_{t_0}^{t_0+T_f} \sigma(x, y, z, t) dt \tag{5.3}$$

where, T_f is flow time over which the averaging is accomplished and t_0 is the time after the start of the simulation at which the averaging process is initiated.

In a disturbed EK flow since the concentration field is quickly changing, one can define a perturbation of the scalar variable $\sigma(x, y, z, t)$ as the deviation from its time-averaged value as follows,

$$\sigma'(x, y, z, t) = \sigma(x, y, z, t) - \bar{\sigma}(x, y, z, t) \tag{5.4}$$

Then the mean square perturbation is calculated by

$$\bar{\sigma}'(x, y, z, t)^2 = \frac{1}{T_f} \int_{t_0}^{t_0+T_f} \sigma'(x, y, z, t)^2 dt \tag{5.5}$$

Figure 5.12 shows the average conductivity concentration fields under the applied electric field of $E_a = 650$ V/cm for different conductivity ratios varying from 1.5 to 10.0. As described in [20], since typically the disturbances of EKI convect downstream too fast and the flow structures can hardly be resolved by the human eye, the average scalar fields can be viewed as and be comparable to what is observed by eyes through the microscope binoculars when running the experiments. From Figure 5.12, it can be seen that for a low conductivity ratio of $\gamma = 1.5$ the center stream remains in a thin filament as no disturbances occur in that case. As the conductivity ratio increases, the center stream is dispersed along the spanwise direction in the east channel and the source of disturbances moves back towards $x/w = 0$.

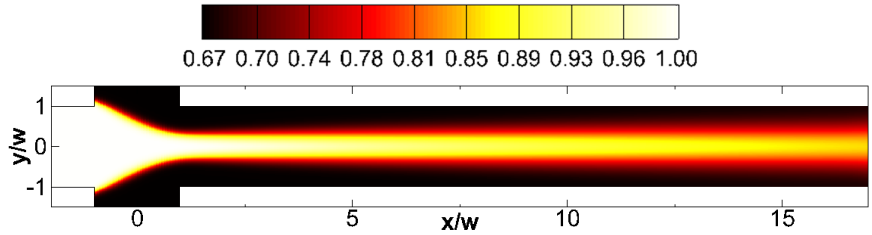

(a) $\gamma = 1.5$

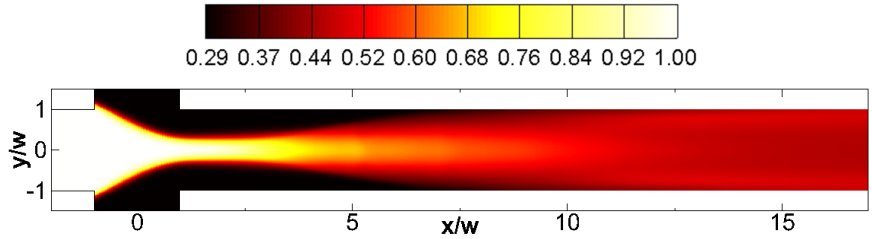

(b) $\gamma = 3.5$

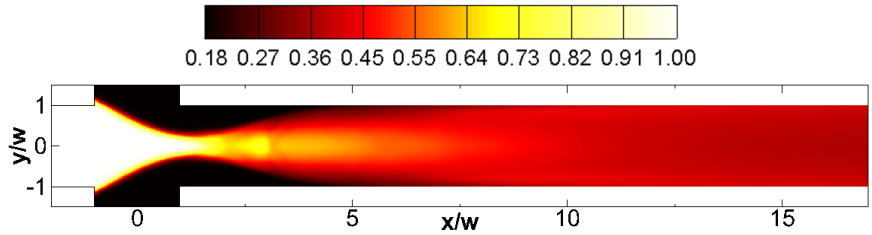

(c) $\gamma = 5.5$

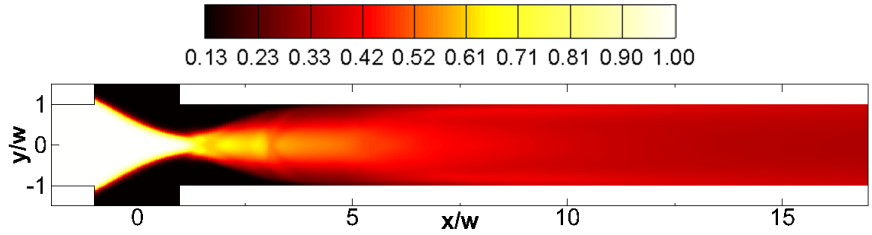

(d) $\gamma = 7.5$

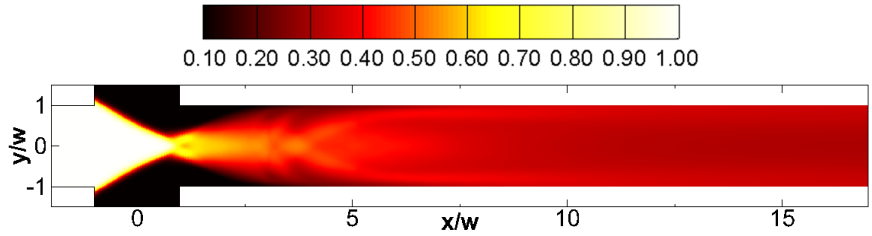

(e) $\gamma = 10.0$

Fig. 5.12. Average conductivity concentration fields at an applied electric field of $E_a = 650$ V/cm for different conductivity ratios.

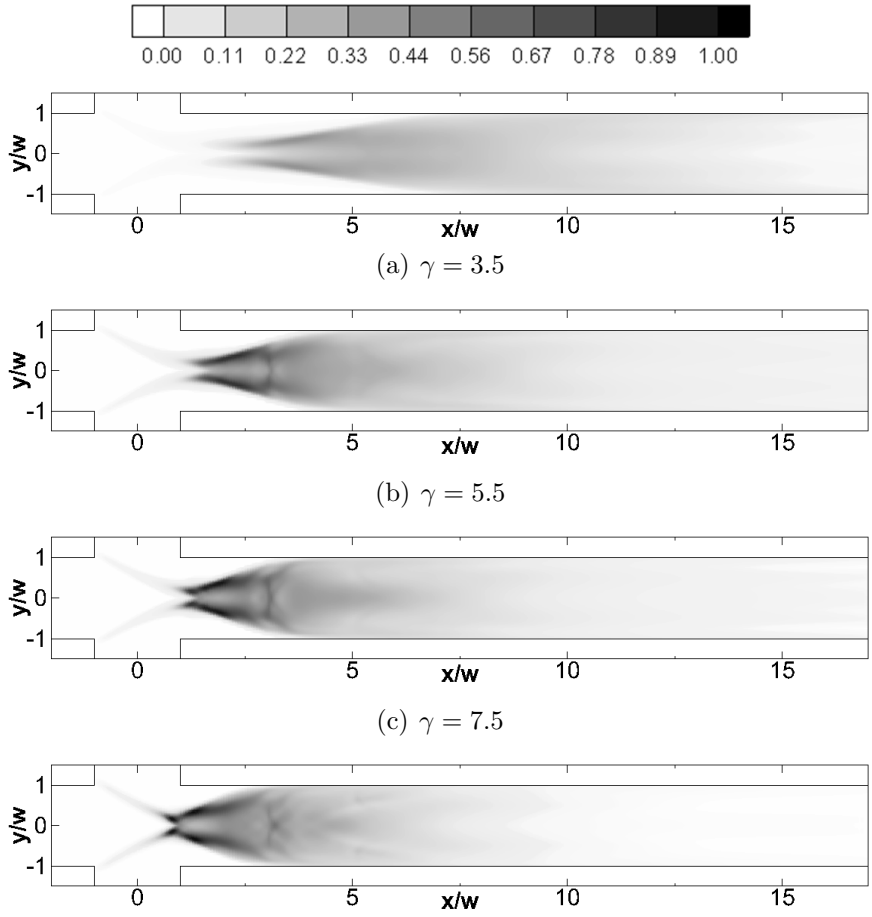

(a) $\gamma = 3.5$

(b) $\gamma = 5.5$

(c) $\gamma = 7.5$

(d) $\gamma = 10.0$

Fig. 5.13. Mean square conductivity concentration perturbation fields at an applied electric field of $E_a = 650$ V/cm for different conductivity ratios.

Such phenomena can be illustrated more clearly by the mean square perturbation fields. Figure 5.13 show the mean square perturbation fields under the applied electric field of $E_a = 650$ V/cm for different conductivity ratios varying from 3.5 to 10.0. Note that since for $\gamma = 1.5$ the concentration field stays at its stable state, the calculated mean square perturbation field has negligible small values (very close to 0) throughout the domain and thus is not included in Figure 5.13. From the mean square perturbation fields it clearly shows that as the conductivity ratio γ increases

perturbations grow in strength and the origin point of disturbances changes upstream from the location of $x/w \approx 2.5$ to $x/w \approx 0.8$.

5.3.2 Effect of Electric Field Strength on EKI

In this subsection, critical features of EKI phenomena in a cross-shaped microchannel are qualitatively described by three-dimensional simulation results. The conductivity ratio γ is considered as $\gamma = 10.0$ and the electric field ratios are assumed to be $\beta_W = \beta_N = 1.0$. The external electric field E_a is increased from a low value of 250 V/cm for steady state to a high strength of 1350 V/cm under which a chaotic flow characteristic can be found.

Representative instantaneous snapshots of the conductivity concentration field at different applied fields from 250 V/cm to 500 V/cm are given in Figure 5.14. According to the experiments done in [32], for the conductivity ratio $\gamma = 10.0$ the threshold value of the nominal electric field E_a for the onset of EKI was found to be $E_a \approx 260$V/cm. Thus, as shown in Figure 5.14 (a) for $E_a = 250$ V/cm the EK flow remains in its stable state. However, when the electric field is set to $E_a = 280$ V/cm which exceeds the critical value of 260 V/cm, small disturbances are observed from $x/w \approx 8.0$. Along the downstream direction, the size and strength of those disturbances slightly grows but right after a short distance at $x/w \approx 15.0$ the disturbance amplitude vanishes, see Figure 5.14 (b). After the applied field is increased to $E_a = 350$ V/cm, as shown in Figure 5.14 (c), the original straight interfaces are buckled into a sinuous-wave pattern from $x/w \approx 5.0$ and the amplitude gradually grows to the full width of the channel as the disturbances convect downstream. At the higher applied field of $E_a = 500$ V/cm, disturbances develop rapidly. As shown in Figure 5.14 (d), coherent structures are formed and the location where the disturbances originate becomes closer to the intersection of the microchannel (i.e. at $x/w \approx 2.0$) compared to the $E_a = 350$ V/cm case. In the downstream region, the high-conductivity center stream fluctuates with a periodic alignment between the up-

per and lower walls (along the y-direction) and the mixed conductivity concentration occupies the full channel width from $x/w \approx 8.0$ along the downstream direction.

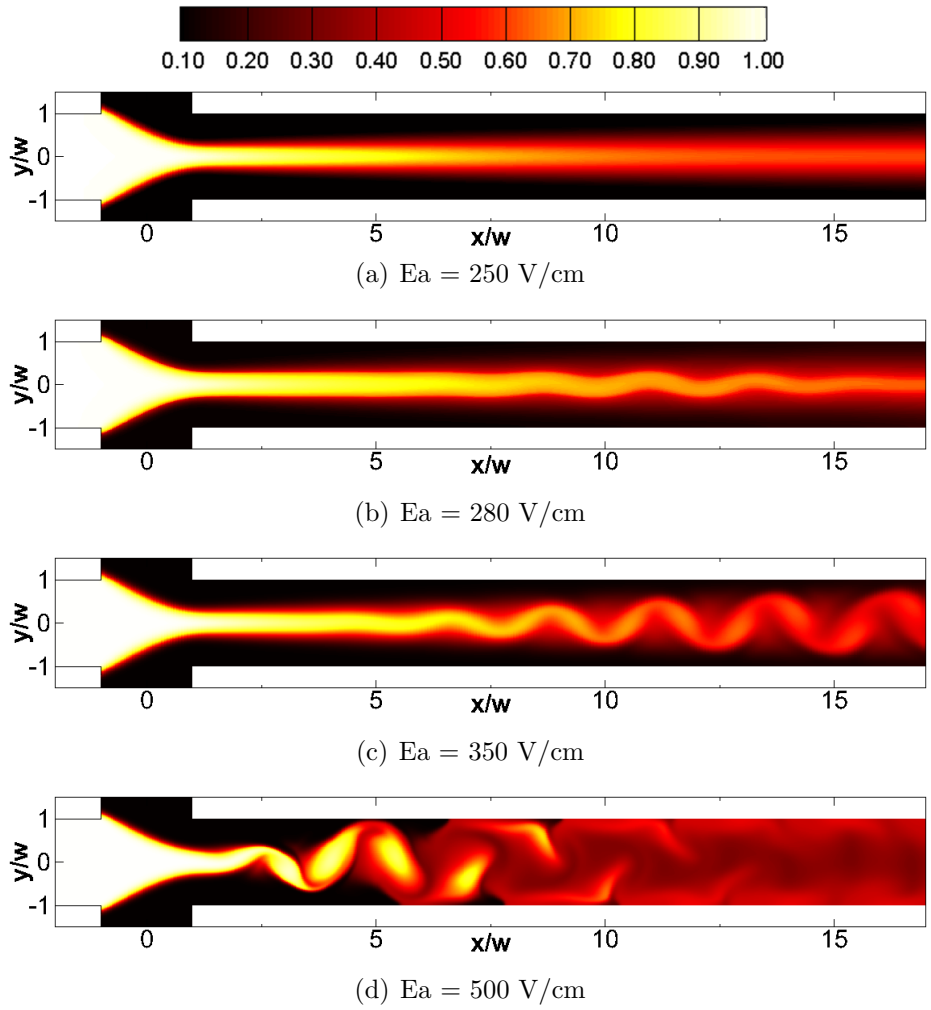

(a) Ea = 250 V/cm

(b) Ea = 280 V/cm

(c) Ea = 350 V/cm

(d) Ea = 500 V/cm

Fig. 5.14. Representative instantaneous snapshots of conductivity concentration fields at different applied fields from 250 V/cm to 500 V/cm for $\gamma = 10.0$ and $\beta_W = \beta_N = 1.0$.

If the nominal electric field E_a is further raised, for example, beyond 700 V/cm, more chaotic EKI phenomena can be observed as shown in Figures 5.15 (a)-(c). As the applied field E_a is increased to 700 V/cm, see Figure 5.15 (a), the source of disturbances approaches upstream to the triangle-shaped injection head at $x/w \approx 1.0$. The throat quickly swings between the upper and lower walls. Previously observed

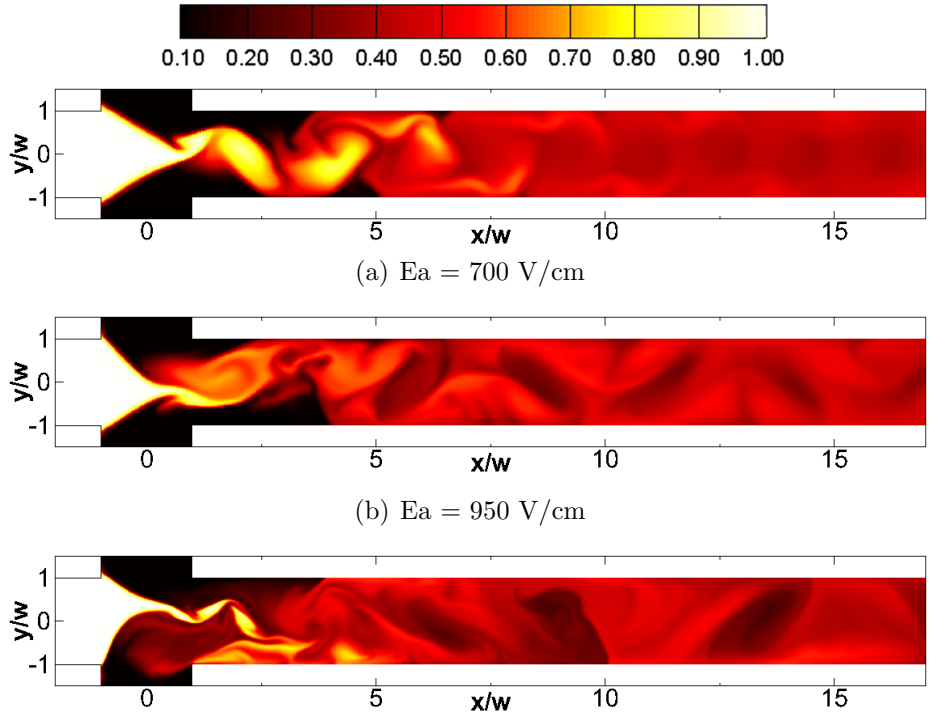

(a) Ea = 700 V/cm

(b) Ea = 950 V/cm

(c) Ea = 1350 V/cm

Fig. 5.15. Representative instantaneous snapshots of conductivity concentration fields at different applied fields from 700 V/cm to 1350 V/cm for $\gamma = 10.0$ and $\beta_W = \beta_N = 1.0$.

coherent structures disappear. More complex scalar structures in the downstream region are formed and they are no longer periodic. Under a higher electric field of $E_a = 950$ V/cm as shown in Figure 5.15 (b), the EK flow undergoes more severer instability. The triangle-shaped head becomes thinner and completely moves back into the intersection region of the microchannel at $x/w \approx 0.5$. High-conductivity sample stream is rapidly injected into the downstream region. At a further increased electric field of $E_a = 1350$V/cm, the source of disturbances approaches further upstream, i.e. at $x/w < 0.0$. The triangle-shaped head is additionally compressed to a thin filament. It rapidly oscillates in an aperiodic way along the spanwise direction (y-direction), and thus strongly injects high-conductivity electrolyte into the downstream region.

As a result, highly disordered scalar patterns are formed and a well-mixed fluid is observed downstream in the east channel.

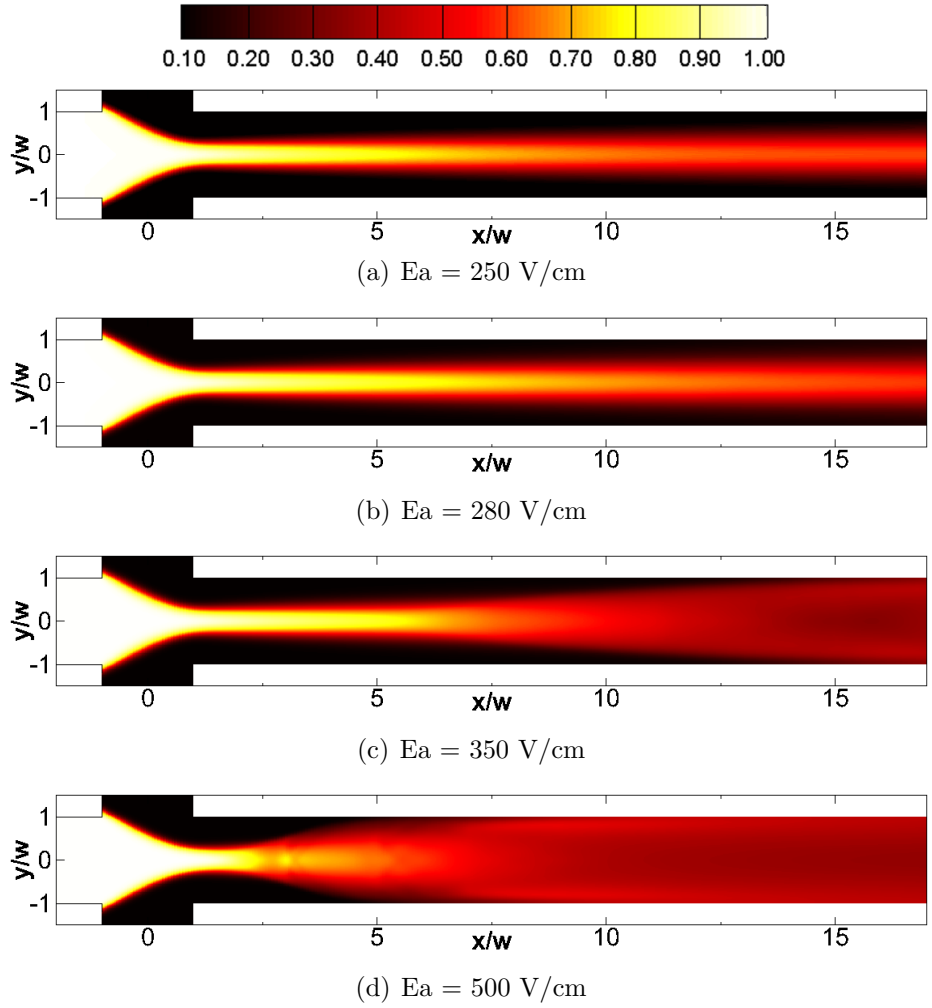

(a) Ea = 250 V/cm

(b) Ea = 280 V/cm

(c) Ea = 350 V/cm

(d) Ea = 500 V/cm

Fig. 5.16. Average conductivity concentration fields at different applied fields from 250 V/cm to 500 V/cm for $\gamma = 10.0$ and $\beta_W = \beta_N = 1.0$.

Figure 5.16 presents the average conductivity concentration fields at different applied fields from 250 V/cm to 500 V/cm for $\gamma = 10.0$ and $\beta_W = \beta_N = 1.0$. It can be seen that as the EK flow stays in the stable state at the electric field $E_a = 250$ V/cm which is below the threshold value of $E_a = 260$ V/cm, the corresponding average concentration field looks identical to its instantaneous scalar field, see Figure 5.16(a).

When $E_a = 280$ V/cm, since only small-amplitude perturbations are observed in a part of the downstream region, the average concentration field looks very similar to that for $E_a = 250$ V/cm case except that the center stream is slightly dispersed from $x/w \approx 8.0$ to the outlet. As the electric fields are increased to $E_a = 500$ V/cm, the center stream is gradually widened in the average scalar fields and the source of perturbations moves from $x/w \approx 5.0$ to 2.0, see Figures 5.16 (c) and (d). Figure 5.17 shows the corresponding average scalar fields at higher applied fields from 700 V/cm to 1350 V/cm for $\gamma = 10.0$ and $\beta_W = \beta_N = 1.0$. As the electric field strength increases, the origin location of disturbances moves further and further into the intersection region of the microchannel and the center stream is highly dispersed due to large-amplitude disturbances, see Figures 5.17 (a)-(c).

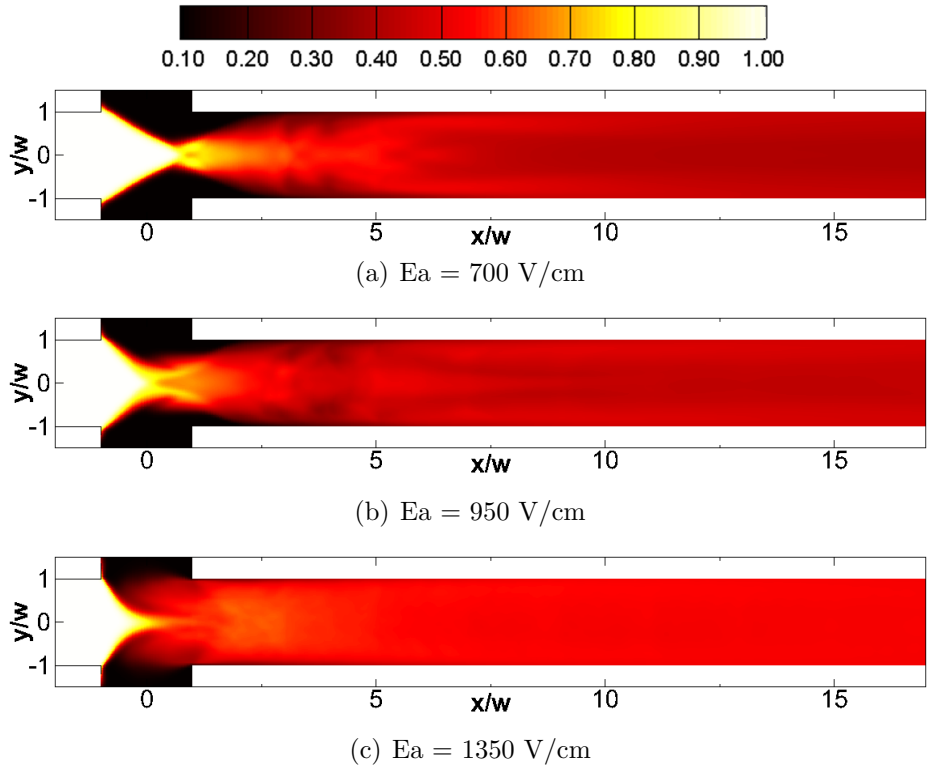

(a) Ea = 700 V/cm

(b) Ea = 950 V/cm

(c) Ea = 1350 V/cm

Fig. 5.17. Average conductivity concentration fields at different applied fields from 700 V/cm to 1350 V/cm for $\gamma = 10.0$ and $\beta_W = \beta_N = 1.0$.

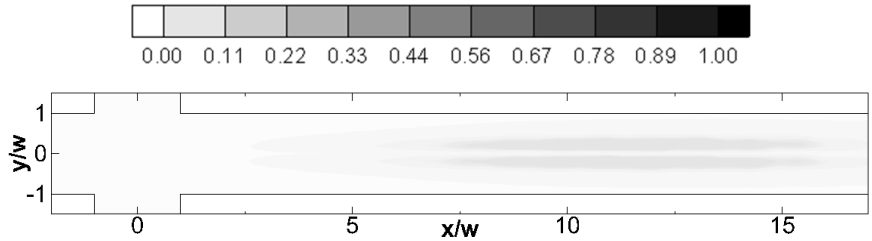

(a) Ea = 280 V/cm

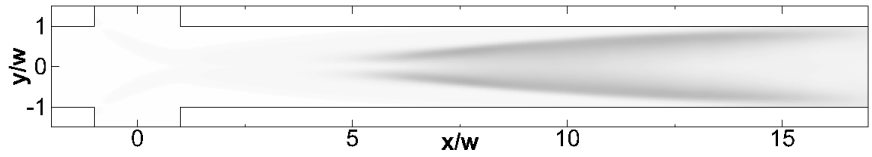

(b) Ea = 350 V/cm

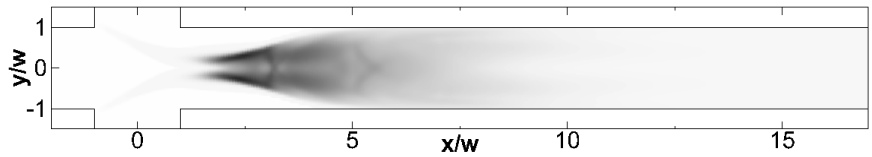

(c) Ea = 500 V/cm

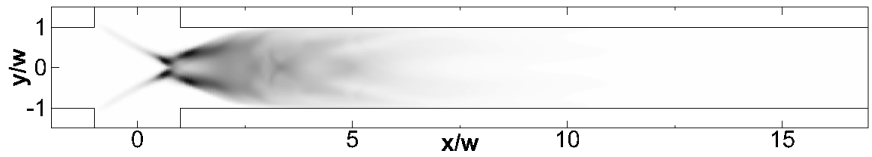

(d) Ea = 700 V/cm

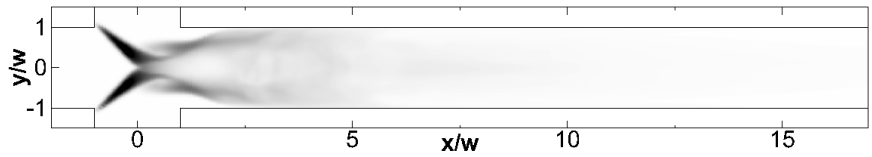

(e) Ea = 950 V/cm

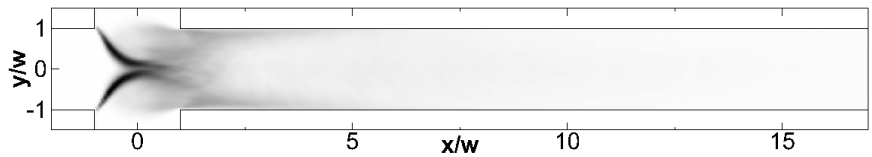

(f) Ea = 1350 V/cm

Fig. 5.18. Mean square perturbation fields at seven applied fields from 280 V/cm to 1350 V/cm for $\gamma = 10.0$ and $\beta_W = \beta_N = 1.0$.

Figure 5.18 gives the mean square perturbation fields at six applied fields from 280 V/cm to 1350 V/cm for $\gamma = 10.0$ and $\beta_W = \beta_N = 1.0$. Note that the result for $E_a = 250$ V/cm is not included in the figure as at the stable state the calculated mean square perturbation field has negligible small values (very close to 0) throughout the domain. Figure 5.18 (a) shows the slightly disturbed EK flow at $E_a = 280$ V/cm. In the east channel, two thin perturbation bands are observed along the streamwise direction starting at the downstream position of $x/w \approx 7.5$ and vanishing near $x/w \approx 16.0$, which reflects the phenomenon presented in Figure 5.14 (b). At the higher applied field of $E_a = 350$ V/cm, perturbations originate at $x/w \approx 5.0$. The disturbance region is gradually widened to the full channel width as perturbations convect downstream, see Figure 5.16(b). Under $E_a = 500$ V/cm as shown in Figure 5.18 (c), the source of perturbations is located backward at $x/w \approx 2.0$ and the perturbation region occupies the full width of the channel from $x/w \approx 5.0$. The region of strong disturbances is observed from $x/w \approx 2.0$ to 8.0. With the increase of the electric field, the perturbations grow in strength and the location of the perturbation origin moves back to the microchannel intersection region, i.e. $x/w < 1.0$. When the applied field is above $E_a = 700$ V/cm, for example, $E_a = 950$ V/cm as shown in Figure 5.18(e), the source of strong disturbances approaches upstream to $x/w \approx 0.0$ and the triangle-shaped injection head swings periodically along the spanwise direction. At a further increased electric field of $E_a = 1350$V/cm, see Figure 5.18 (f), the origin point of strong fluctuations moves further back to $x/w \approx -0.5$. The injection head oscillates more violently in the vertical direction. A shortened region of strong disturbances is observed from $x/w \approx 0.0$ to 2.5. It can be seen that as the electric field is raised, more vigorous instabilities occur in the EK flow and they originate further and further upstream towards $x/w = -1.0$. In addition, the region of strongly disturbed EK flow becomes shorter and shorter along the streamwise direction. As a result, the EK flow reaches a highly disordered status more rapidly at the location closer to the channel intersection region. For example, at the applied fields beyond $E_a = 700$V/cm the EK

flow in the east channel is observed to be well mixed after the downstream point of $x/w \approx 7.0$.

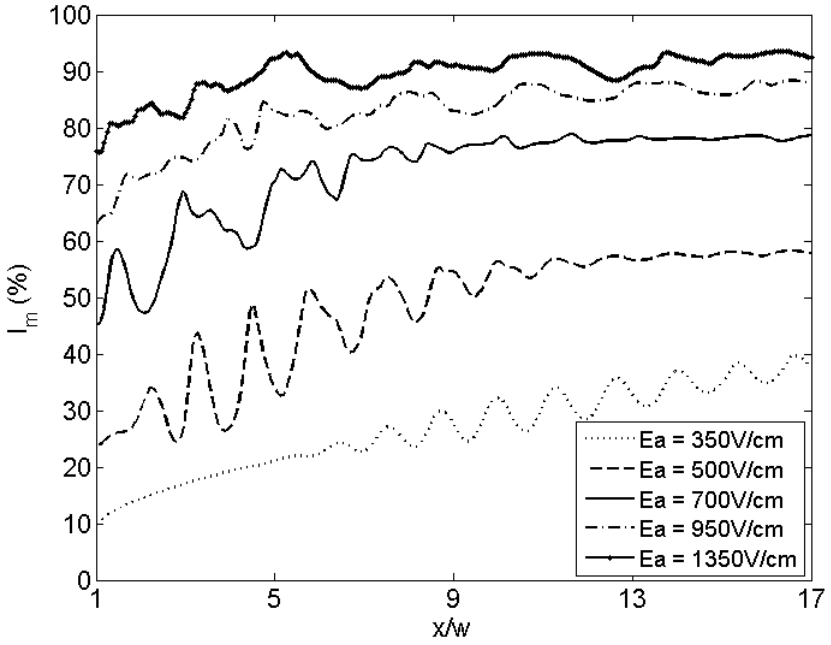

Fig. 5.19. Comparison of conductivity mixing intensities along the downstream direction for the nominal electric field E_a varying from 350 to 1350 V/cm.

To quantify and compare the degree of mixing occurred in the cross-shaped microchip at different electric field strengths, the mixing intensities I_m in the east channel under E_a varying from 350 V/cm to 1350 V/cm are given in Figure 5.19. From the figure, it is clear to see that with the increase of the electric field E_a the degree of mixing is enhanced. A strong applied field strength results in higher values of mixing intensity throughout the entire east channel. At $E_a = 350$ V/cm and 500 V/cm, the sinuous increase patterns in mixing intensities correspond to the periodic fluctuations are observed. Under $E_a = 700$ V/cm and higher applied fields, the corresponding mixing intensity fluctuates in a random way but keeps increasing along the east channel and finally reaches a high value, for example, around 90% at $x/w = 17.0$.

Overall, the EKI phenomena at different electric field strengths in a cross-shaped microchannel described by the three-dimensional simulations in this subsection give a good qualitative agreement with the experimental results available in the literature, for example, provided by [20] in which an extensive parametric study of EKI was performed and detailed EKI phenomena through a wide range of conductivity ratio (γ) and electric field ratio (β_W and β_N) were presented. Though the parameters used in the simulations such as γ and β_W, β_N are different from [20], as pointed out by [20] that the values of the conductivity ratio (γ) and the applied field ratios (β_W, β_N) only affect the applied field required to reach each flow regime, and the qualitative nature of the instability does not vary with the parameter γ. Thus, it clearly shows that the present WENO solver can capture critical features of EKI phenomena in the considered cross-shaped microchannel.

5.3.3 Effect of Channel Depth on EKI

In this subsection we investigate the effect of channel depth d on EKI in the cross-shaped microchannel. Again, we consider the injection mode for $\gamma = 10.0$ and assume the same electric field ratios $\beta_W = \beta_N = 1.0$. With the same channel width of $60\mu m$, the channel depth will be varied in the simulations.

In order to clearly present and compare the results, a parameter α is introduced to relate the channel depth d with the half of the channel width w as $\alpha = w/d$. Simulations for four different values of the width-to-depth ratio α varying from 2.0 to 3.75 are performed by using the present WENO solver. Figure 5.20 summarizes the threshold values of the applied electric field E_a found in the simulations for the corresponding cases. It can be seen that as α increases meaning the channel depth is decreasing, the threshold value of the nominally applied field E_a increases as well. In other words, a thicker microchannel requires a lower threshold value of the electric field for the onset of EKI.

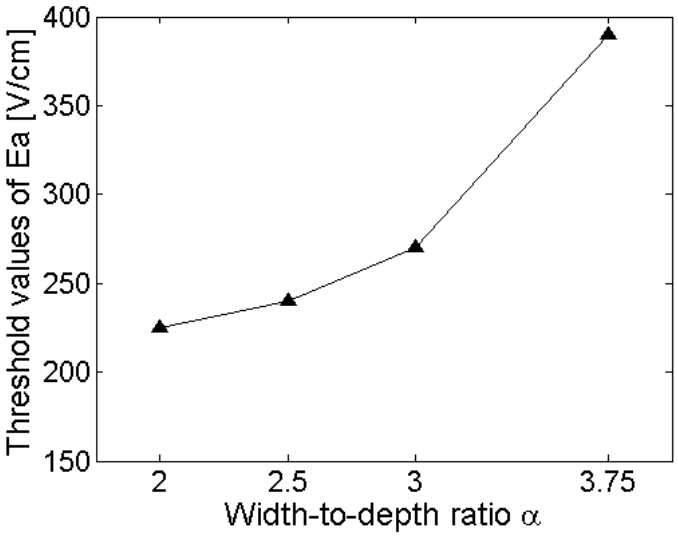

Fig. 5.20. The threshold values of the nominal electric field E_a for different width-to-depth ratio α varying from 2.0 to 3.75.

To show the effect of the channel depth on EKI phenomena, representative instantaneous snapshots of conductivity concentration fields at an applied field of $E_a = 650$V/cm for different values of the width-to-depth ratio α are presented in Figure 5.21. When $\alpha = 3.75$ which refers to a very thin channel depth of 8μm, high-conductivity center stream is disturbed and periodically fluctuates in the east channel, see Figure 5.21 (a). As α decreases (i.e. the channel depth increases), more severe instabilities are observed in the EK flow. Disturbances develop rapidly in more complex, aperiodic patterns along the downstream direction, see Figure 5.21 (b)-(d).

From Figure 5.22 that gives the mean square perturbation fields for the corresponding different values of depth-to-width ratio at the applied field of $E_a = 650$ V/cm, it can be found that with the decrease of α (the channel depth is increasing) perturbations grow in strength and their origin location moves from the point of $x/w \approx 2.5$ for $\alpha = 3.75$ back into the microchannel intersection region at $x/w \approx -0.5$ for $\alpha = 2.0$. The triangle-shaped injection head that originally stays in the microchannel intersection region for $\alpha = 3.75$ or 3.0 is compressed due to strong disturbances

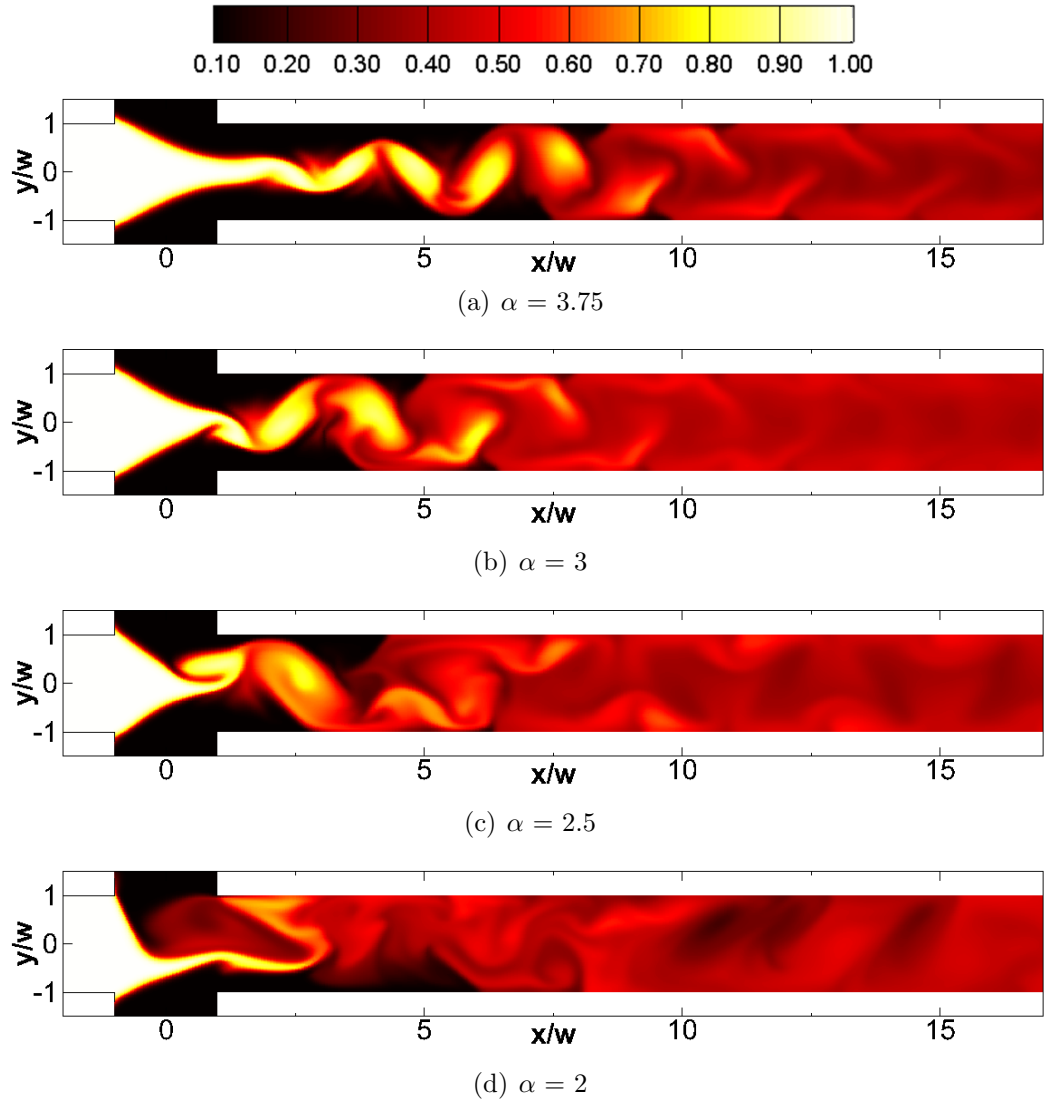

(a) $\alpha = 3.75$

(b) $\alpha = 3$

(c) $\alpha = 2.5$

(d) $\alpha = 2$

Fig. 5.21. Representative instantaneous snapshots of conductivity concentration field at an applied field of $E_a = 650$ V/cm for different width-to-depth ratios with $\gamma = 10.0$.

for $\alpha = 2.5$ and 2.0. When $\alpha = 2.0$ as shown in Figure 5.22 (d), the injection head oscillates strongly in the spanwise direction which results in a shortened perturbation region in the upstream part of the east channel and thus leads to a well mixed EK flow in the downstream region of the channel.

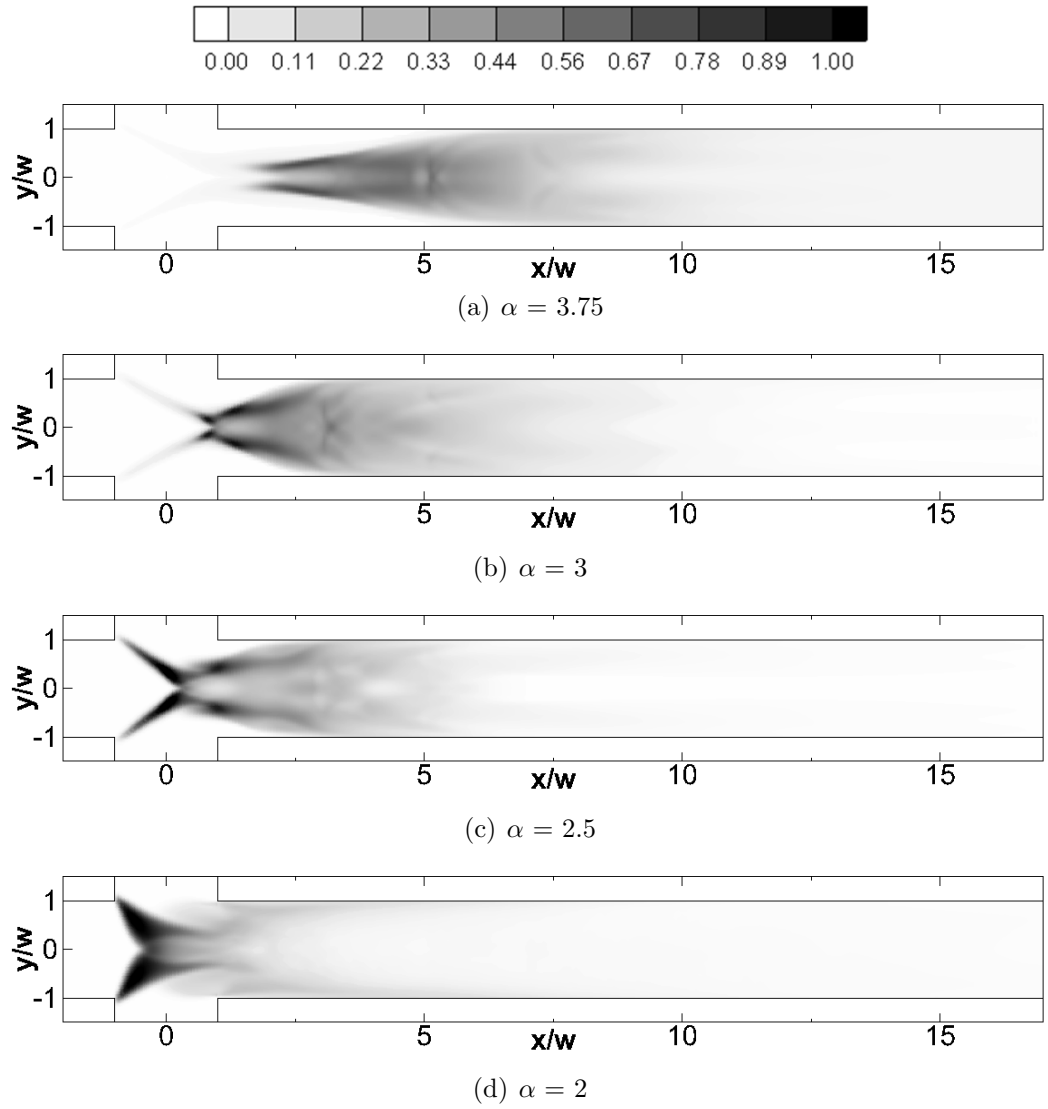

(a) $\alpha = 3.75$

(b) $\alpha = 3$

(c) $\alpha = 2.5$

(d) $\alpha = 2$

Fig. 5.22. Mean square perturbation fields at an applied field of $E_a =$ 650 V/cm for different depth-to-width ratios with $\gamma = 10.0$.

According to the above presented simulation results, it seems that at the same applied electric field instabilities are more likely to develop in the microchannel as the channel depth increases. This can be confirmed by looking at the cross-sectional snapshots of conductivity concentration field and the mixing intensity along the east channel. Figure 5.23 (a) and (b) show the corresponding conductivity concentration

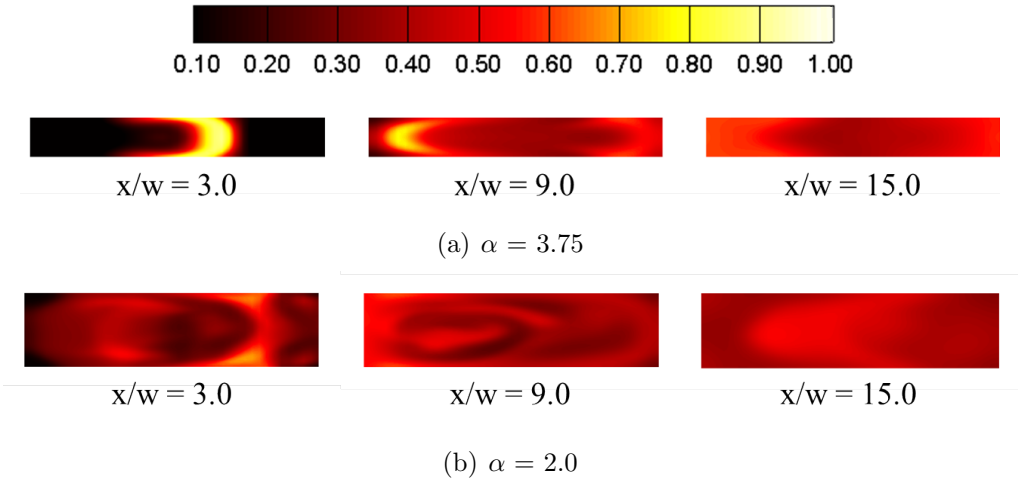

Fig. 5.23. Representative instantaneous cross-sectional snapshots of conductivity concentration field at an applied field of $E_a = 650$ V/cm for the width-to-depth ratio $\alpha = 3.75$ and 2.0.

fields at the cross-sections of x/w = 3.0, x/w = 9.0 and x/w = 15.0 under the applied field of $E_a = 650$ V/cm for the width-to-depth ratio $\alpha = 3.75$ and 2.0, respectively. For a thin channel depth of $\alpha = 3.75$, the distribution of conductivity concentration is nearly symmetric through the three selected cross-sections. However, when the channel is thicker as $\alpha = 2.0$ the EK flow in the east channel undergoes more severe instability and strongly rolls up in the vertical direction (z-direction) as well which results in an asymmetric concentration distribution at all of the three cross sections. As the EK flow approaches towards the outlet, the z-axial fluctuations become more pronounced and finally leads to a well stirred concentration field throughout the cross section near the outlet.

Figure 5.24 shows the mixing intensities I_m along the east channel for different values of the width-to-depth ratio α varying from 2.0 to 3.75 at $E_a = 650$ V/cm. Though the EK flow is under the same applied field, a higher mixing intensity throughout the east channel is observed as the ratio α decreases which corresponds to a thicker channel depth. This indicates the mixing of electrolytes with different conductivity

concentrations in the east channel is evidently enhanced due to the increase of the channel depth.

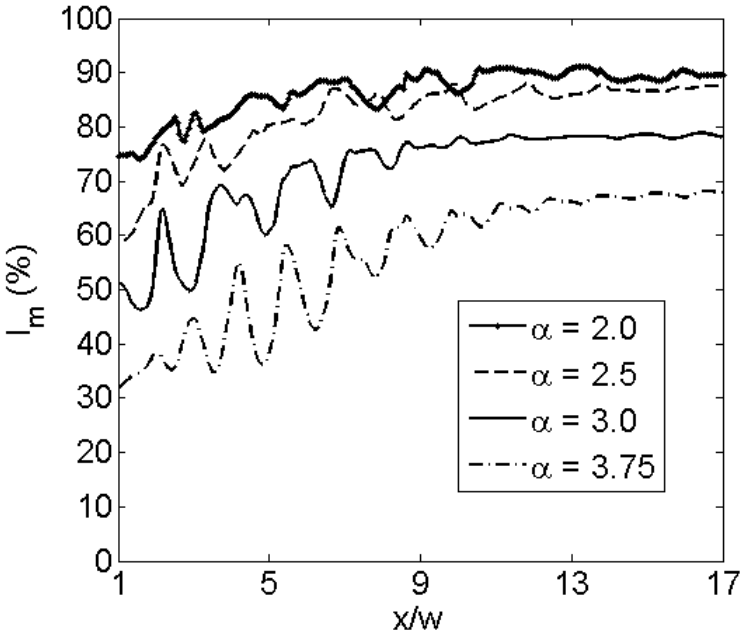

Fig. 5.24. Comparison of conductivity mixing intensities along the downstream direction for different width-to-depth ratio α varying from 2.0 to 3.75 at an applied field of $E_a = 650$ V/cm.

In summary, we can draw a conclusion that a thicker microchannel requires a lower threshold value of the external applied field for the onset of EKI. Under the same electric field strength that can trigger EKI, intensive instabilities are more likely to develop in the EK flow and thus a well-mixed fluid is easier to be achieved as the channel depth increases.

5.3.4 Effect of Electric Field Ratio on EKI

In the previous numerical study on EKI, we imposed the same electrical potentials at the three inlets of the cross-shaped microchannel by setting $\beta_W = \beta_N = 1.0$ for all the cases. Since the cross-shaped microchannel considered in the present study

has identical lengths for the north, south, and west channels (i.e. $L_N = L_S = L_W$), and the outlet of the east channel is grounded (i.e. $\phi_E = 0$), the electrical potentials imposed at the three inlets can be derived from Equations (5.1b)-(5.1d) as

$$\phi_S = E_a(L_E + L_S) \tag{5.6a}$$

$$\phi_W = \beta_W \phi_S \tag{5.6b}$$

$$\phi_N = \beta_N \phi_S \tag{5.6c}$$

Thus, when $\beta_W = \beta_N = 1.0$, the potentials applied at the three inlets arrive at the same value, i.e. $\phi_N = \phi_S = \phi_W$.

In this subsection, we vary the values of the electric field ratios β_W and β_N and investigate their effect on EKI in the cross-shaped microchannel. The conductivity ratio is assumed to be $\gamma = 10.0$. Basically we consider two general cases. First, we symmetrically impose the same electrical potentials at the north and south inlets by setting $\beta_N = 1.0$ and then change the other electric field ratio β_W such that $\beta_W > 1.0$ or $\beta_W < 1.0$. We call this case as symmetric electric field case. For the second general case, we apply different potentials at the north and south inlets as well such that none of the potentials imposed at the three inlets are identical. Thus we call such case as non-symmetric electric field case.

Figure 5.25 shows the conductivity concentration fields at the corresponding stable states for $\beta_N = 1.0$ and different values of $\beta_W = 0.95, 1.0$, and 1.05 in the symmetric electric field case. Since the flow rate in each channel is proportional to the strength of the electric field applied in the corresponding channel, as β_W increases meaning higher electric fields are applied in the west channel than those applied in the north and south channels the center-to-sheath flow-rate ratio increases as well. In other words, the flow from the west channel moves faster and faster compared to the streams from the north and south channels with the increase of β_W. As a result, more high-conductivity center stream is driven from the west channel to the downstream east channel which leads to a bigger triangle-shaped injection head and a wider band of high-conductivity stream in the east channel as the electric ratio β_W is raised from 0.95 to 1.05.

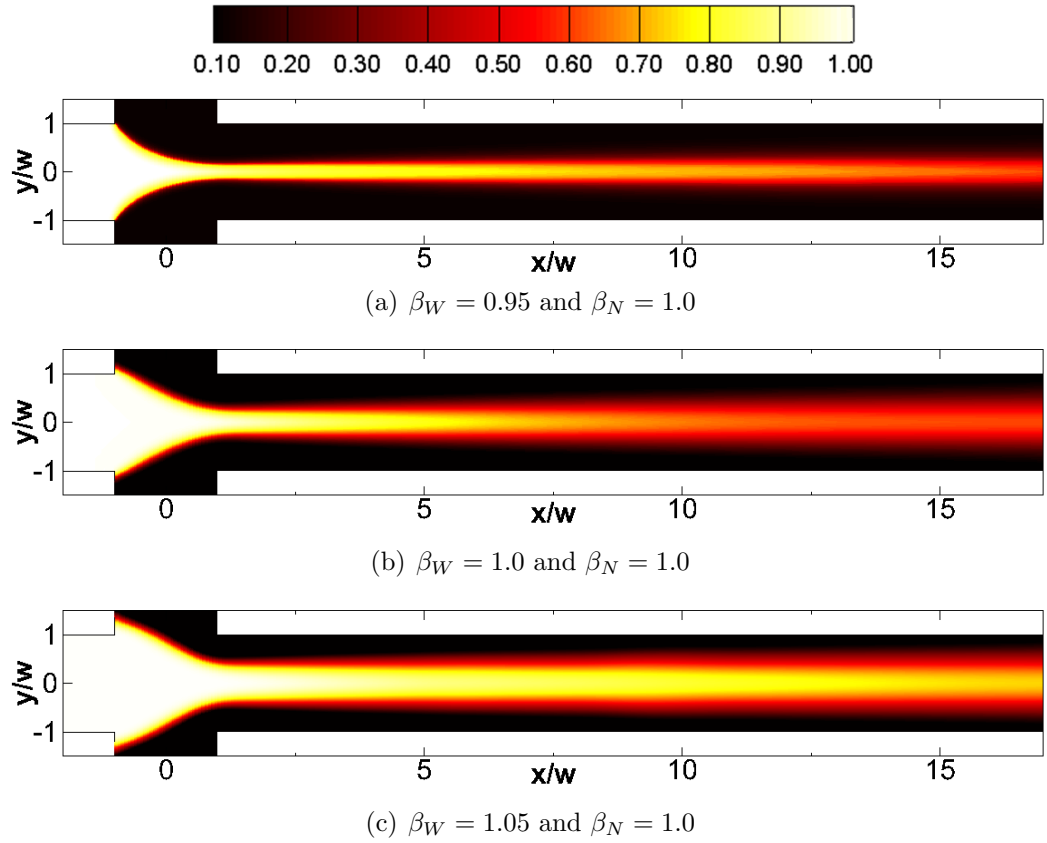

(a) $\beta_W = 0.95$ and $\beta_N = 1.0$

(b) $\beta_W = 1.0$ and $\beta_N = 1.0$

(c) $\beta_W = 1.05$ and $\beta_N = 1.0$

Fig. 5.25. Conductivity concentration fields at stable states for different electric field ratios with $\gamma = 10.0$.

As shown in Figure 5.25 (a), for a lower value of $\beta_W = 0.95$ a thin triangular injection head is formed within the intersection region of the microchannel. The interfaces of the high- and low-conductivity streams in the intersection region are concave curves to the center of the head. The undisturbed straight center stream in the east channel is narrow and only occupies a small portion of the channel width. As β_W is increased to $\beta_W = 1.05$, the injection head is enlarged outside the microchannel intersection region and the interfaces of the high- and low-conductivity streams are changed to convex curves to the center of the head. In addition, a much wider center stream with higher concentration intensity is formed in the east channel, see Figure 5.25 (c).

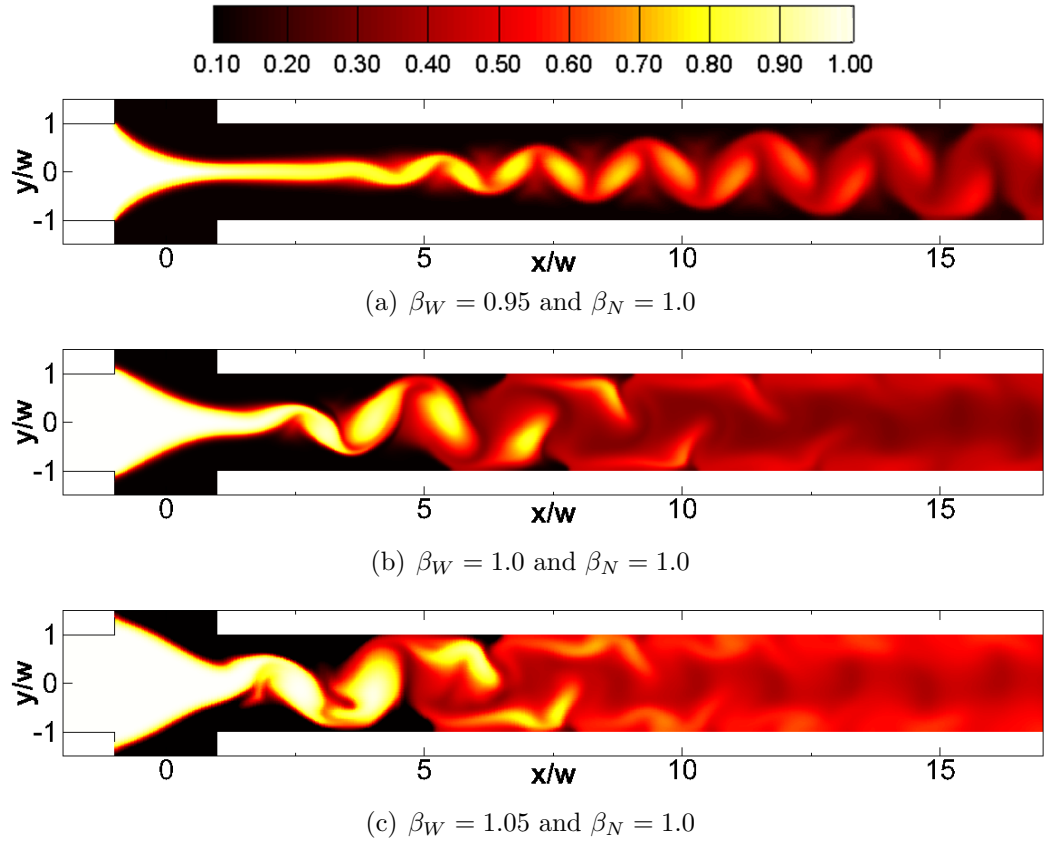

(a) $\beta_W = 0.95$ and $\beta_N = 1.0$

(b) $\beta_W = 1.0$ and $\beta_N = 1.0$

(c) $\beta_W = 1.05$ and $\beta_N = 1.0$

Fig. 5.26. Representative instantaneous snapshots of conductivity concentration field at an applied field of $E_a = 500V/cm$ for different electric field ratios with $\gamma = 10.0$.

Figure 5.26 shows the disturbed conductivity concentration fields for β_W varying from 0.95 to 1.05 under the nominal electric field of $E_a = 500$ V/cm which is higher than the threshold values for all the considered cases. When $\beta_W = 0.95$, the throat of the high-conductivity center stream in the east channel is squeezed to a thin band by the two symmetrical sheath streams with faster flow rates. As a result, small perturbations originate far from the microchannel intersection region at $x/w \approx 4.0$ and as they convect downstream the disturbance amplitude gradually grows and occupies the east channel in spanwise direction. As β_W is raised to 1.05, a larger amount of high-conductivity stream is injected into the east channel due to higher

flow rate from the west channel, see Figure 5.26 (c). A much wider throat with higher concentration intensity is observed being oscillating right from the entrance of the east channel at $x/w \approx 1.0$. As the throat swings in a relatively lower rate compared to what has been observed in the $\beta_W = 0.95$ case, the disturbance amplitude quickly develops to the full channel width. From the simulation results shown in Figures 5.25 and 5.26, for the symmetrical electric field case ($\beta_N = 1.0$) the electric field ratio β_W can be used to control the center-to-sheath flow-rate ratio and the width of high-conductivity center stream in the east channel.

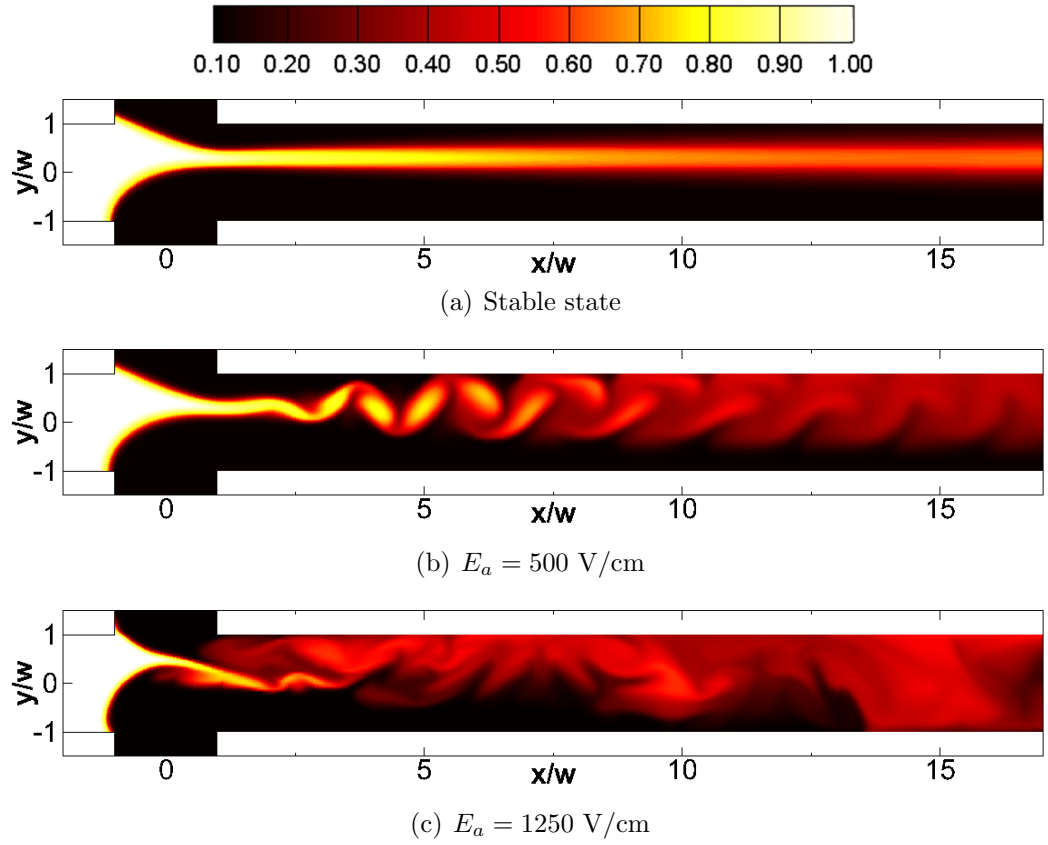

(a) Stable state

(b) $E_a = 500$ V/cm

(c) $E_a = 1250$ V/cm

Fig. 5.27. Representative instantaneous snapshots of conductivity concentration fields at different strengths of electric fields for $\beta_W = 0.98$ and $\beta_N = 1.08$ with $\gamma = 10.0$.

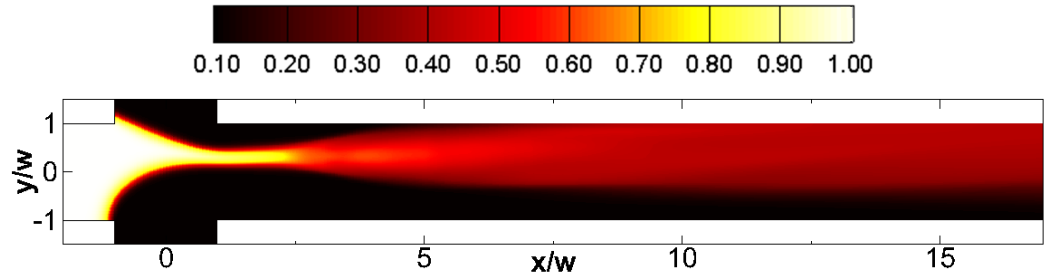

(a) $E_a = 500$ V/cm

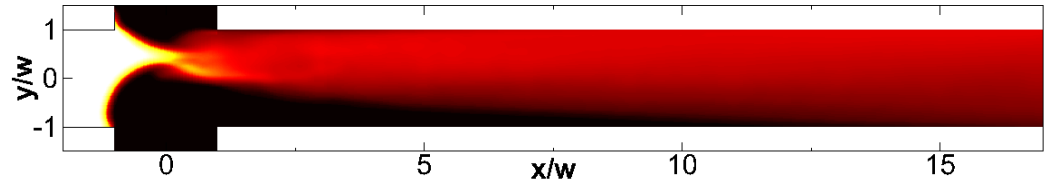

(b) $E_a = 1250$ V/cm

Fig. 5.28. Average conductivity concentration fields at the applied fields of $E_a = 500$ and 1250 V/cm for $\beta_W = 0.98$ and $\beta_N = 1.08$ with $\gamma = 10.0$.

Next we simulate the non-symmetric electric field case. When different electrical potentials are asymmetrically imposed at the three inlets, the center stream in the east channel could be shifted not to align with the central line of the channel at the stable state and the perturbation patterns at the disturbed state would be also changed. Figure 5.27 shows the representative instantaneous snapshots of conductivity concentration fields at the stable state and two applied fields of $E_a = 500$ and 1250 V/cm for $\beta_W = 0.98$ and $\beta_N = 1.08$. The average concentration fields at the two disturbed states are given in Figure 5.28. From the figures it can be observed that at the stable state as shown in Figure 5.27 (a), the high-conductivity stream from the west channel is straightly injected into the east channel along $y/w \approx 0.3$ in the upper region of the channel instead of along $y/w = 0$ due to $\beta_N = 1.08$ meaning a higher electric field is imposed in the north channel than that applied in the south channel. At an intermediate electric field of $E_a = 500$ V/cm which is high enough to invoke EKI, the disturbed high-conductivity stream convects to the outlet in a peri-

odic alignment and only occupies the upper region of the channel from $y/w \approx -0.4$ to $y/w = 1.0$ without touching the bottom wall, see Figures 5.27 (b) and 5.28 (a). As the electric field strength is increased to $E_a = 1250$ V/cm, a thinner throat is formed. The injection head is compressed back within the microchannel intersection region. It periodically swings and strongly injects the high-conductivity stream into the east channel. As a result, though in the upstream section of the east channel still disturbances only occupies the upper region of the channel, as they convect downstream rapidly in a chaotic way the disturbances expands to the full channel width from the downstream section of $x/w \approx 13.0$, see Figure 5.27 (c) and 5.28 (b).

6. SUMMARY AND FUTURE WORK

6.1 Conclusions

Isotachphoresis (ITP) and electrokinetic instability (EKI) are complex, multi-physical flow phenomena on the micro-scales and they are extensively applied in microfluidic systems. Due to non-linear electromigration physics, sharp gradients in species concentration and/or applied electric fields occur in ITP and EKI which in many cases causes difficult design and simulation challenges. In order to accurately simulate and thus help understand essential physics of ITP and EKI, a useful numerical tool is desired. In the present research work, a high-order accurate finite difference solver using WENO schemes was developed to simulate ITP and EKI phenomena in microfluidic devices. The solver is using a multiblock approach to allow simulations with complex geometries that fit Cartesian grids. Validation of the solver was performed for one- and two-dimensional ITP and EKI problems. In one-dimensional ITP problems in which steep gradients present in both electric field and species concentration, it was demonstrated that on a given uniform grid the present WENO solver not only gave a smooth non-oscillatory solution, but it also offered a more accurate result with reduced numerical diffusion compared to several existing numerical schemes including the first-order upwind, the second-order central difference, the SLIP, and the sixth-order compact schemes. The present solver was also validated to be capable of accurately resolving the sharp interfaces of species concentration and electric field by comparing the numerical result with the available analytical solution. For two-dimensional ITP and EKI problems, the present solver was used to study and understand the basic physics and mechanism of the two kinds of electrokinetic phenomena. The obtained simulation results showed good agreements with the numerical and the experimental results presented in the literature which indicates that

the solver is a good numerical tool to analyze and study ITP and EKI phenomena in microfluidic systems.

By using the validated solver, a series of three-dimensional simulations were carried out to study EKI phenomena in a cross-shaped microchannel, a more realistic flow geometry relevant to a wide range of applications. Simulation results obtained by the present solver for two specific and other more general cases showed that the solver had the capability to capture the threshold value of electric field for the onset of EKI and it offered a better numerical description of the critical features of EKI phenomena in the considered cross-shaped microchannel compared to the numerical and experimental results provided in the literature. From the general parametric study, several useful guidelines showing the effect of different parameters on EKI in a cross-shaped microchannel for the injection mode of $\gamma > 1.0$ were explored by the present solver and are summarized as follows.

- The higher the conductivity ratio is, the lower the threshold value of the applied electric field is required to invoke the instability in the EK flow.

- As the strength of the applied electric field is raised, the EK flow transits from a steady state to a time-dependent periodic state, and then to an aperiodic, chaotic state. In such process the mixing intensity in the downstream channel tends to reach higher values. Thus, from a point of mixing, the degree of mixing can be enhanced with the increase of the applied field.

- For a fixed conductivity ratio, a thicker microchannel requires a lower threshold value of the applied field for the onset of EKI. Under the same electric field, intensive instabilities are more likely to develop in the EK flow. Thus a well-mixed fluid is easier to be achieved as the channel depth increases.

- In general, the ratio between the west and the north/south nominal fields can be used to control the center-to-sheath flow-rate ratio and the width of high-conductivity center stream in the downstream channel. In a non-symmetric

electric field case, the position of the injected center stream in the downstream channel can be shifted along the spanwise direction by changing the ratio between the north and south nominal fields. In such case, the disturbed high-conductivity stream may only occupy a part of the downstream channel along spanwise direction under a relatively low applied field. However, at higher electric fields the highly perturbed high-conductivity stream may expand to the full channel width as it convects downstream.

6.2 Future Work

Research work that could be undertaken in future is proposed in this section. First, as the present solver can only handle complex geometries that fit Cartesian grid, in the future an Immersed Boundary Method (IBM) needs to be added to enable the solver to handle arbitrarily complex geometries. IBM methods have been widely used in CFD as an attractive methodology because of its capability to efficiently handle complex moving and rotating geometries on structured grids [104]. In most cases, the implementation of IBM methods is based on explicit time advancement schemes [105]. Thus, the main challenge for the current case is how to appropriately couple an IBM with the semi-implicit scheme for time integration in the present solver so as to successfully implement the IBM. In addition, efforts need to be made to ensure that the solver can also efficiently handle complex geometries for all the involved scalars, including species concentration and electrical potential etc. The methods presented in [106, 107] may be useful to deal with the problem.

Another improvement that could be done for the present solver is to implement Adaptive Mesh Refinement (AMR) rather than only using a uniform grid throughout the computational domain. The use of AMR will allow the solver to dynamically concentrate more grid points at regions of high gradients in ITP, for example, without a need to refine the mesh everywhere. In this way, the solver will accurately resolve

the sharp interfaces which is of key importance in ITP with a significantly reduced computational cost.

Finally the newly developed solver can be applied to simulate full three-dimensional ITP phenomena with multiple species in complex geometries by accurately and efficiently solving a set of governing equations including the incompressible Navier-Stokes equations with electrical body forces, the charge conservation equation, and a large number of species transport equations.

LIST OF REFERENCES

LIST OF REFERENCES

[1] C.-X. Zhang and W. Thormann, "Head-column field-amplified sample stacking in binary system capillary electrophoresis. 2. optimization with a preinjection plug and application to micellar electrokinetic chromatography," *Analytical chemistry*, vol. 70, no. 3, pp. 540–548, 1998.

[2] S. L. Freire and A. R. Wheeler, "Proteome-on-a-chip: Mirage, or on the horizon?," *Lab on a Chip*, vol. 6, no. 11, pp. 1415–1423, 2006.

[3] G. M. Whitesides, "The origins and the future of microfluidics," *Nature*, vol. 442, no. 7101, pp. 368–373, 2006.

[4] D. R. Reyes, D. Iossifidis, P.-A. Auroux, and A. Manz, "Micro total analysis systems. 1. introduction, theory, and technology," *Analytical chemistry*, vol. 74, no. 12, pp. 2623–2636, 2002.

[5] T. M. Squires and S. R. Quake, "Microfluidics: Fluid physics at the nanoliter scale," *Reviews of modern physics*, vol. 77, no. 3, p. 977, 2005.

[6] P. S. Dittrich, K. Tachikawa, and A. Manz, "Micro total analysis systems. latest advancements and trends," *Analytical chemistry*, vol. 78, no. 12, pp. 3887–3908, 2006.

[7] T. Vilkner, D. Janasek, and A. Manz, "Micro total analysis systems. recent developments," *Analytical chemistry*, vol. 76, no. 12, pp. 3373–3386, 2004.

[8] D. Janasek, J. Franzke, and A. Manz, "Scaling and the design of miniaturized chemical-analysis systems," *Nature*, vol. 442, no. 7101, pp. 374–380, 2006.

[9] J. P. Brody, P. Yager, R. E. Goldstein, and R. H. Austin, "Biotechnology at low reynolds numbers," *Biophysical Journal*, vol. 71, no. 6, pp. 3430–3441, 1996.

[10] E. A. Mansur, M. YE, Y. WANG, and Y. DAI, "A state-of-the-art review of mixing in microfluidic mixers," *Chinese Journal of Chemical Engineering*, vol. 16, no. 4, pp. 503–516, 2008.

[11] C.-C. Chang and R.-J. Yang, "Electrokinetic mixing in microfluidic systems," *Microfluidics and Nanofluidics*, vol. 3, no. 5, pp. 501–525, 2007.

[12] S. Shin, I. Kang, and Y. Cho, "Mixing enhancement by using electrokinetic instability under time-periodic electric field," *Journal of Micromechanics and Microengineering*, vol. 15, no. 3, p. 455, 2005.

[13] A. E. Herr, J. I. Molho, K. A. Drouvalakis, J. C. Mikkelsen, P. J. Utz, J. G. Santiago, and T. W. Kenny, "On-chip coupling of isoelectric focusing and free solution electrophoresis for multidimensional separations," *Analytical chemistry*, vol. 75, no. 5, pp. 1180–1187, 2003.

[14] W. Thormann, R. A. Mosher, and M. Bier, "Experimental and theroretical dynamics of isoelectric focusing: Elucidation of a general separation mechanism," *Journal of Chromatography A*, vol. 351, pp. 17–29, 1986.

[15] R. Bharadwaj and J. G. Santiago, "Dynamics of field-amplified sample stacking," *Journal of Fluid Mechanics*, vol. 543, pp. 57–92, 2005.

[16] D. Saville, "Electrohydrodynamics: the taylor-melcher leaky dielectric model," *Annual review of fluid mechanics*, vol. 29, no. 1, pp. 27–64, 1997.

[17] M. Oddy, J. Santiago, and J. Mikkelsen, "Electrokinetic instability micromixing," *Analytical Chemistry*, vol. 73, no. 24, pp. 5822–5832, 2001.

[18] C.-H. Chen and J. G. Santiago, "Electrokinetic flow instability in high concentration gradient microflows," ASME, 2002.

[19] C.-H. Chen, H. Lin, S. K. Lele, and J. G. Santiago, "Convective and absolute electrokinetic instability with conductivity gradients," *Journal of Fluid Mechanics*, vol. 524, pp. 263–303, 2005.

[20] J. D. Posner and J. G. Santiago, "Convective instability of electrokinetic flows in a cross-shaped microchannel," *Journal of Fluid Mechanics*, vol. 555, no. 1, pp. 1–42, 2006.

[21] D. A. Boy and B. D. Storey, "Electrohydrodynamic instabilities in microchannels with time periodic forcing," *Physical Review E*, vol. 76, no. 2, p. 026304, 2007.

[22] M. H. Oddy and J. G. Santiago, "Multiple-species model for electrokinetic instability," *Physics of Fluids*, vol. 17, p. 064108, 2005.

[23] I. Workings, N. Lectures, P. Classics, and P. Plus, "Electric fields yield chaos in microflows," *Masthead (PDF)*, vol. 109, no. 36, 2012.

[24] J. D. Posner, C. L. Pérez, and J. G. Santiago, "Electric fields yield chaos in microflows," *Proceedings of the National Academy of Sciences*, vol. 109, no. 36, pp. 14353–14356, 2012.

[25] J. Park, S. Shin, K. Y. Huh, and I. Kang, "Application of electrokinetic instability for enhanced mixing in various micro–t-channel geometries," *Physics of Fluids*, vol. 17, p. 118101, 2005.

[26] M.-Z. Huang, R.-J. Yang, C.-H. Tai, C.-H. Tsai, and L.-M. Fu, "Application of electrokinetic instability flow for enhanced micromixing in cross-shaped microchannel," *Biomedical microdevices*, vol. 8, no. 4, pp. 309–315, 2006.

[27] C.-H. Tai, R.-J. Yang, M.-Z. Huang, C.-W. Liu, C.-H. Tsai, and L.-M. Fu, "Micromixer utilizing electrokinetic instability-induced shedding effect," *Electrophoresis*, vol. 27, no. 24, pp. 4982–4990, 2006.

[28] Y.-J. Pan, C.-M. Ren, and R.-J. Yang, "Electrokinetic flow focusing and valveless switching integrated with electrokinetic instability for mixing enhancement," *Journal of Micromechanics and Microengineering*, vol. 17, no. 4, p. 820, 2007.

[29] H. Lin, B. D. Storey, M. H. Oddy, C.-H. Chen, and J. G. Santiago, "Instability of electrokinetic microchannel flows with conductivity gradients," *Physics of Fluids*, vol. 16, p. 1922, 2004.

[30] B. D. Storey, "Direct numerical simulation of electrohydrodynamic flow instabilities in microchannels," *Physica D: Nonlinear Phenomena*, vol. 211, no. 1, pp. 151–167, 2005.

[31] K. H. Kang, J. Park, I. S. Kang, and K. Y. Huh, "Initial growth of electrohydrodynamic instability of two-layered miscible fluids in t-shaped microchannels," *International journal of heat and mass transfer*, vol. 49, no. 23, pp. 4577–4583, 2006.

[32] W.-J. Luo, "Effect of ionic concentration on electrokinetic instability in a cross-shaped microchannel," *Microfluidics and nanofluidics*, vol. 6, no. 2, pp. 189–202, 2009.

[33] C. Druzgalski, M. Andersen, and A. Mani, "Direct numerical simulation of electroconvective instability and hydrodynamic chaos near an ion-selective surface,"

[34] E. Demekhin, N. Nikitin, and V. Shelistov, "Direct numerical simulation of electrokinetic instability and transition to chaotic motion," *arXiv preprint arXiv:1306.4259*, 2013.

[35] F. M. Everaerts, J. L. Beckers, and T. P. Verheggen, *Isotachophoresis: theory, instrumentation and applications*. Elsevier, 2011.

[36] P.-A. Auroux, D. Iossifidis, D. R. Reyes, and A. Manz, "Micro total analysis systems. 2. analytical standard operations and applications," *Analytical chemistry*, vol. 74, no. 12, pp. 2637–2652, 2002.

[37] L. Chen, J. E. Prest, P. R. Fielden, N. J. Goddard, A. Manz, and P. J. Day, "Miniaturised isotachophoresis analysis," *Lab on a Chip*, vol. 6, no. 4, pp. 474–487, 2006.

[38] G. Goet, T. Baier, and S. Hardt, "Transport and separation of micron sized particles at isotachophoretic transition zones," *Biomicrofluidics*, vol. 5, no. 1, p. 014109, 2011.

[39] D. Saville and O. Palusinski, "Theory of electrophoretic separations. part i: Formulation of a mathematical model," *AIChE Journal*, vol. 32, no. 2, pp. 207–214, 1986.

[40] J. Kim, K. Choi, S. Cho, A. Riaz, and D. S. Chung, "Isotachophoretically assisted on-line complexation of trace metal ions in a highly saline matrix for capillary electrophoresis," *Bulletin of the Korean Chemical Society*, vol. 33, no. 3, pp. 790–794, 2012.

[41] S.-W. Huang and H.-F. Tzeng, "Simultaneous determination of deoxycytidine diphosphate and deoxycytidine triphosphate by capillary electrophoresis with transient isotachophoretic stacking: A sensitive monitoring method for ribonucleotide reductase activity," *Electrophoresis*, vol. 33, no. 3, pp. 536–542, 2012.

[42] S. Medina-Casanellas, F. Benavente, J. Barbosa, and V. Sanz-Nebot, "Transient isotachophoresis in on-line solid phase extraction capillary electrophoresis time-of-flight-mass spectrometry for peptide analysis in human plasma," *Electrophoresis*, vol. 32, no. 13, pp. 1750–1759, 2011.

[43] J.-M. Busnel, B. Schoenmaker, R. Ramautar, A. Carrasco-Pancorbo, C. Ratnayake, J. S. Feitelson, J. D. Chapman, A. M. Deelder, and O. A. Mayboroda, "High capacity capillary electrophoresis-electrospray ionization mass spectrometry: Coupling a porous sheathless interface with transient-isotachophoresis," *Analytical chemistry*, vol. 82, no. 22, pp. 9476–9483, 2010.

[44] M. Bercovici, S. K. Lele, and J. G. Santiago, "Open source simulation tool for electrophoretic stacking, focusing, and separation," *Journal of Chromatography A*, vol. 1216, no. 6, pp. 1008–1018, 2009.

[45] http://www.esi-group.com/products/Fluid Dynamics/cfd-ace.

[46] http://www.comsol.com.

[47] M. Bier, O. Palusinski, R. Mosher, and D. Saville, "Electrophoresis: mathematical modeling and computer simulation," *Science*, vol. 219, no. 4590, pp. 1281–1287, 1983.

[48] O. Palusinski, A. Graham, R. Mosher, M. Bier, and D. Saville, "Theory of electrophoretic separations. part ii: construction of a numerical simulation scheme and its applications," *AIChE journal*, vol. 32, no. 2, pp. 215–223, 1986.

[49] E. V. Dose and G. A. Guiochon, "High-resolution modeling of capillary zone electrophoresis and isotachophoresis," *Analytical chemistry*, vol. 63, no. 11, pp. 1063–1072, 1991.

[50] M. C. Breadmore, R. A. Mosher, and W. Thormann, "High-resolution computer simulations of stacking of weak bases using a transient ph boundary in capillary electrophoresis. 1. concept and impact of sample ionic strength," *Analytical chemistry*, vol. 78, no. 2, pp. 538–546, 2006.

[51] V. Hruška, M. Jaroš, and B. Gaš, "Simul 5–free dynamic simulator of electrophoresis," *Electrophoresis*, vol. 27, no. 5-6, pp. 984–991, 2006.

[52] M. Bercovici, S. K. Lele, and J. G. Santiago, "Compact adaptive-grid scheme for high numerical resolution simulations of isotachophoresis," *Journal of Chromatography A*, vol. 1217, no. 4, pp. 588–599, 2010.

[53] http://stanfordspresso.blogspot.com.

[54] S. V. Ermakov, M. S. Bello, and P. Giorgio Righetti, "Numerical algorithms for capillary electrophoresis," *Journal of Chromatography A*, vol. 661, no. 1, pp. 265–278, 1994.

[55] J. H. Martens, J. C. Reijenga, J. H. ten Thije Boonkkamp, R. M. Mattheij, and F. M. Everaerts, "Transient modelling of capillary electrophoresis:: Isotachophoresis," *Journal of Chromatography A*, vol. 772, no. 1-2, pp. 49–62, 1997.

[56] T. Sounart and J. Baygents, "Simulation of electrophoretic separations by the flux-corrected transport method," *Journal of Chromatography A*, vol. 890, no. 2, pp. 321–336, 2000.

[57] J.-W. Yu, Y. Chou, and R.-J. Yang, "High-resolution modeling of isotachophoresis and zone electrophoresis," *Electrophoresis*, vol. 29, no. 5, pp. 1048–1057, 2008.

[58] J. Shim, P. Dutta, and C. F. Ivory, "Finite-volume methods for isotachophoretic separation in microchannels," *Numerical Heat Transfer, Part A: Applications*, vol. 52, no. 5, pp. 441–461, 2007.

[59] S. Bhattacharyya and P. P. Gopmandal, "Interaction of electroosmotic flow on isotachophoretic transport of ions," in *Proceedings of World Academy of Science, Engineering and Technology*, no. 69, Citeseer, 2012.

[60] S. Bhattacharyya, P. P. Gopmandal, T. Baier, and S. Hardt, "Sample dispersion in isotachophoresis with poiseuille counterflow," *Physics of Fluids (1994-present)*, vol. 25, no. 2, p. 022001, 2013.

[61] F. Dang, L. Zhang, M. Jabasini, N. Kaji, and Y. Baba, "Characterization of electrophoretic behavior of sugar isomers by microchip electrophoresis coupled with videomicroscopy," *Analytical chemistry*, vol. 75, no. 10, pp. 2433–2439, 2003.

[62] A. O. El Moctar, N. Aubry, and J. Batton, "Electro-hydrodynamic micro-fluidic mixer," *Lab on a Chip*, vol. 3, no. 4, pp. 273–280, 2003.

[63] R. A. Frazier, J. M. Ames, and H. E. Nursten, "The development and application of capillary electrophoresis methods for food analysis," *Electrophoresis*, vol. 20, no. 15-16, pp. 3156–3180, 1999.

[64] K. Kleparnik and P. Bocek, "Dna diagnostics by capillary electrophoresis," *Chemical reviews*, vol. 107, no. 11, pp. 5279–5317, 2007.

[65] E. Dabek-Zlotorzynska, "Capillary electrophoresis in the determination of pollutants," *Electrophoresis*, vol. 18, no. 12-13, pp. 2453–2464, 1997.

[66] M. J. Desai and D. W. Armstrong, "Separation, identification, and characterization of microorganisms by capillary electrophoresis," *Microbiology and molecular biology reviews*, vol. 67, no. 1, pp. 38–51, 2003.

[67] D. A. Shetty, T. C. Fisher, A. R. Chunekar, and S. H. Frankel, "High-order incompressible large-eddy simulation of fully inhomogeneous turbulent flows," *Journal of Computational Physics*, vol. 229, no. 23, pp. 8802–8822, 2010.

[68] Y. Delorme, K. Anupindi, A. Kerlo, D. Shetty, M. Rodefeld, J. Chen, and S. Frankel, "Large eddy simulation of powered fontan hemodynamics," *Journal of biomechanics*, 2012.

[69] J. Melcher and G. Taylor, "Electrohydrodynamics: a review of the role of interfacial shear stresses," *Annual Review of Fluid Mechanics*, vol. 1, no. 1, pp. 111–146, 1969.

[70] R. F. Probstein, *Physicochemical hydrodynamics: an introduction*. Wiley. com, 2005.

[71] V. G. Levich and S. A. Rice, "Physicochemical hydrodynamics," *Physics Today*, vol. 16, p. 75, 1963.

[72] C.-H. Chen, "Electrohydrodynamic stability," in *Electrokinetics and Electrohydrodynamics in Microsystems*, pp. 177–220, Springer, 2011.

[73] R. J. Hunter, *Zeta potential in colloid science: principles and applications*, vol. 125. Academic press London, 1981.

[74] H.-C. Chang and L. Y. Yeo, *Electrokinetically driven microfluidics and nanofluidics*. Cambridge University Press Cambridge, UK:, 2010.

[75] R.-L. Chien and D. S. Burgi, "Field amplified sample injection in high-performance capillary electrophoresis," *Journal of Chromatography A*, vol. 559, no. 1, pp. 141–152, 1991.

[76] S. Yao, D. E. Hertzog, S. Zeng, J. C. Mikkelsen Jr, and J. G. Santiago, "Porous glass electroosmotic pumps: design and experiments," *Journal of Colloid and Interface Science*, vol. 268, no. 1, pp. 143–153, 2003.

[77] R. Sadr, M. Yoda, Z. Zheng, and A. Conlisk, "An experimental study of electro-osmotic flow in rectangular microchannels," *Journal of Fluid Mechanics*, vol. 506, pp. 357–367, 2004.

[78] G. Garcia-Schwarz, M. Bercovici, L. Marshall, and J. Santiago, "Sample dispersion in isotachophoresis," *Journal of Fluid Mechanics*, vol. 679, pp. 455–475, 2011.

[79] T. Baier, F. Schoenfeld, and S. Hardt, "Analytical approximations to the flow field induced by electroosmosis during isotachophoretic transport through a channel," *Journal of Fluid Mechanics*, vol. 682, pp. 101–119, 2011.

[80] D. A. Shetty, J. Shen, A. J. Chandy, and S. H. Frankel, "A pressure-correction scheme for rotational navier-stokes equations and its application to rotating turbulent flows," *Communications in Computational Physics*, vol. 9, no. 3, pp. 740–755, 2011.

[81] G.-S. Jiang and C.-W. Shu, "Efficient implementation of weighted eno schemes.," tech. rep., DTIC Document, 1995.

[82] Y. Morinishi, T. Lund, O. Vasilyev, and P. Moin, "Fully conservative higher order finite difference schemes for incompressible flow," *Journal of Computational Physics*, vol. 143, no. 1, pp. 90–124, 1998.

[83] R. D. Falgout and U. M. Yang, "hypre: A library of high performance preconditioners," in *Computational ScienceICCS 2002*, pp. 632–641, Springer, 2002.

[84] G. E. Karniadakis, M. Israeli, and S. A. Orszag, "High-order splitting methods for the incompressible navier-stokes equations," *Journal of computational physics*, vol. 97, no. 2, pp. 414–443, 1991.

[85] C. M. Oishi, M. F. Tomé, J. A. Cuminato, and S. McKee, "An implicit technique for solving 3d low reynolds number moving free surface flows," *Journal of Computational Physics*, vol. 227, no. 16, pp. 7446–7468, 2008.

[86] X. Chen, K. Toh, J. Chai, and C. Yang, "Developing pressure-driven liquid flow in microchannels under the electrokinetic effect," *International Journal of Engineering Science*, vol. 42, no. 5, pp. 609–622, 2004.

[87] J. Zhang and T. L. Jackson, "A high-order incompressible flow solver with weno," *Journal of Computational Physics*, vol. 228, no. 7, pp. 2426–2442, 2009.

[88] T. K. Khurana and J. G. Santiago, "Preconcentration, separation, and indirect detection of nonfluorescent analytes using fluorescent mobility markers," *Analytical chemistry*, vol. 80, no. 1, pp. 279–286, 2008.

[89] B. Jung, R. Bharadwaj, and J. G. Santiago, "On-chip millionfold sample stacking using transient isotachophoresis," *Analytical chemistry*, vol. 78, no. 7, pp. 2319–2327, 2006.

[90] A. J. Martin and F. Everaerts, "Displacement electrophoresis," *Analytica chimica acta*, vol. 38, pp. 233–237, 1967.

[91] T. K. Khurana and J. G. Santiago, "Sample zone dynamics in peak mode isotachophoresis," *Analytical chemistry*, vol. 80, no. 16, pp. 6300–6307, 2008.

[92] A. Jameson, "Analysis and design of numerical schemes for gas dynamics, 1: artificial diffusion, upwind biasing, limiters and their effect on accuracy and multigrid convergence," *International Journal of Computational Fluid Dynamics*, vol. 4, no. 3-4, pp. 171–218, 1995.

[93] S. S. Bahga, M. Bercovici, and J. G. Santiago, "Robust and high-resolution simulations of nonlinear electrokinetic processes in variable cross-section channels," *Electrophoresis*, vol. 33, no. 19-20, pp. 3036–3051, 2012.

[94] V. Hruška and B. Gaš, "Kohlrausch regulating function and other conservation laws in electrophoresis," *Electrophoresis*, vol. 28, no. 1-2, pp. 3–14, 2007.

[95] M. Abramowitz and I. A. Stegun, *Handbook of mathematical functions: with formulas, graphs, and mathematical tables*. No. 55, Courier Dover Publications, 1972.

[96] M. C. Breadmore and J. P. Quirino, "100 000-fold concentration of anions in capillary zone electrophoresis using electroosmotic flow controlled counterflow isotachophoretic stacking under field amplified conditions," *Analytical chemistry*, vol. 80, no. 16, pp. 6373–6381, 2008.

[97] J. G. Shackman, M. S. Munson, and D. Ross, "Gradient elution moving boundary electrophoresis for high-throughput multiplexed microfluidic devices," *Analytical chemistry*, vol. 79, no. 2, pp. 565–571, 2007.

[98] H. Lin, "Electrokinetic instability in microchannel flows: A review," *Mechanics Research Communications*, vol. 36, no. 1, pp. 33–38, 2009.

[99] Y. Xu, Y. Gao, H. Wei, Y. Du, and E. Wang, "Field-amplified sample stacking capillary electrophoresis with electrochemiluminescence applied to the determination of illicit drugs on banknotes," *Journal of Chromatography A*, vol. 1115, no. 1, pp. 260–266, 2006.

[100] C. L. Ren and D. Li, "Effects of spatial gradients of electrical conductivity on chip-based sample injection processes," *Analytica chimica acta*, vol. 518, no. 1, pp. 59–68, 2004.

[101] J. Baygents and F. Baldessari, "Electrohydrodynamic instability in a thin fluid layer with an electrical conductivity gradient," *Physics of Fluids*, vol. 10, no. 1, pp. 301–311, 1998.

[102] J. F. Hoburg and J. R. Melcher, "Internal electrohydrodynamic instability and mixing of fluids with orthogonal field and conductivity gradients," *Journal of Fluid Mechanics*, vol. 73, no. 02, pp. 333–351, 1976.

[103] L.-M. Fu, R.-J. Yang, C.-H. Lin, and Y.-S. Chien, "A novel microfluidic mixer utilizing electrokinetic driving forces under low switching frequency," *Electrophoresis*, vol. 26, no. 9, pp. 1814–1824, 2005.

[104] K. Anupindi, Y. Delorme, D. A. Shetty, and S. H. Frankel, "A novel multiblock immersed boundary method for large eddy simulation of complex arterial hemodynamics," *Journal of Computational Physics*, vol. 254, pp. 200–218, 2013.

[105] R. Mittal and G. Iaccarino, "Immersed boundary methods," *Annu. Rev. Fluid Mech.*, vol. 37, pp. 239–261, 2005.

[106] S. Kang, G. Iaccarino, and F. Ham, "Dns of buoyancy-dominated turbulent flows on a bluff body using the immersed boundary method," *Journal of Computational Physics*, vol. 228, no. 9, pp. 3189–3208, 2009.

[107] D. Pan, "A simple and accurate ghost cell method for the computation of incompressible flows over immersed bodies with heat transfer," *Numerical Heat Transfer, Part B: Fundamentals*, vol. 58, no. 1, pp. 17–39, 2010.

VITA

VITA

Qian Li was born and grew up in Beijing, China. He received a Bachelor of Science with a major in Mechanical Engineering and Automation from Beijing University of Technology in July 2007. Due to excellent achievements during the undergraduate years, he was subsequently accepted to become a graduate student by the department of mechanical engineering in Beijing University of Technology without the entrance examinations. He graduated with a Master of Science in Mechanical Engineering in July 2010. In August 2010, he started his doctoral studies in the School of Mechanical Engineering, Purdue University, West Lafayette, IN, USA.

The published papers of Qian Li are listed as follows:

[1] Qian Li, Yann Delorme, Steven Frankel, Moran Bercovici, "High-fidelity Simulations of Electrokinetic Phenomena in Microfluidic Devices", *Microuidics and nanouidics*, in preparation.

[2] Qian Li, Kameswararao Anupindi, Yann Delorme, Steven Frankel, "High-Order Numerical Simulations of Electrokinetic Instability in a Cross-shaped Microchannel", *2013 Israel Society for Theoretical and Applied Mechanics Symposium, Haifa, Israel*, December 1 2013.

[3] Qian Li, Yann Delorme, Steven Frankel, "High Order WENO Simulation of Electrokinetic Instability in a Cross-Shaped Micro-channel", *66th Annual Meeting of the APS Division of Fluid Dynamics, Pittsburg, USA*, November 24-26 2013.

[4] Qian Li, Jing Zhao, "A Universal Approach for Configuration Synthesis of Reconfigurable Robots Based on Fault Tolerant Indices", *Industrial Robot: An International Journal*, Vol. 39(1): pp. 69-78, 2012.

[5] Jing Zhao, Qian Li, "On the Joint Velocity Jump For Redundant Robots in the Presence of Locked-Joint Failures", *ASME Journal of Mechanical Design*, Vol. 130, pp. 102305.1-102305.7, October 2008.

[6] Jing Zhao, Qian Li, "An Analytical Algorithm with Minimum Joint Veloc-ity Jump for Redundant Robots in the Presence of Locked-Joint Failures", *2008 IEEE International Conference on Robotics and Automation*, pp. 1987-1992, May 2008.

[7] Qian Li, Jing Zhao, "Research of the Identity of Fault Tolerance Performance for Kinematically Redundant Robots", *Chinese High Technology Letters*, Vol. 18(6): pp. 615-623, 2008.

[8] Yu Liu, Jing Zhao, Qian Li, "Design of a Multifunctional Nursing Bed", *Machine Design and Research*, Vol. 24: pp. 125-128, May 2008.

[9] Song Yang, Qian Li, Yiliang Zhang, Xiaoyang Li, "Measurement of Three-Dimensional Forces and Displacements for A Deformable Steel Reticulation Device", *Journal of Experimental Mechanics*, Vol. 21(6): pp. 703-709, December 2006.